

INFORMATION TO USERS

This manuscript has been reproduced from the microfilm master. UMI films the text directly from the original or copy submitted. Thus, some thesis and dissertation copies are in typewriter face, while others may be from any type of computer printer.

The quality of this reproduction is dependent upon the quality of the copy submitted. Broken or indistinct print, colored or poor quality illustrations and photographs, print bleedthrough, substandard margins, and improper alignment can adversely affect reproduction.

In the unlikely event that the author did not send UMI a complete manuscript and there are missing pages, these will be noted. Also, if unauthorized copyright material had to be removed, a note will indicate the deletion.

Oversize materials (e.g., maps, drawings, charts) are reproduced by sectioning the original, beginning at the upper left-hand corner and continuing from left to right in equal sections with small overlaps.

Photographs included in the original manuscript have been reproduced xerographically in this copy. Higher quality 6" x 9" black and white photographic prints are available for any photographs or illustrations appearing in this copy for an additional charge. Contact UMI directly to order.

**Bell & Howell Information and Learning
300 North Zeeb Road, Ann Arbor, MI 48106-1346 USA**

UMI[®]
800-521-0600

University of Alberta

**THE INITIATION OF DELAYED HYDRIDE CRACKING
IN ZIRCONIUM-2.5 NIOBIUM**

by

DERONG YAN ©

A thesis submitted to the Faculty of Graduate Studies and Research

in partial fulfillment of the requirements

for the degree of DOCTOR OF PHILOSOPHY

in

MATERIALS ENGINEERING

Department of Chemical and Materials Engineering

Edmonton, Alberta

Fall 1999



National Library
of Canada

Acquisitions and
Bibliographic Services

395 Wellington Street
Ottawa ON K1A 0N4
Canada

Bibliothèque nationale
du Canada

Acquisitions et
services bibliographiques

395, rue Wellington
Ottawa ON K1A 0N4
Canada

Your file *Votre référence*

Our file *Notre référence*

The author has granted a non-exclusive licence allowing the National Library of Canada to reproduce, loan, distribute or sell copies of this thesis in microform, paper or electronic formats.

The author retains ownership of the copyright in this thesis. Neither the thesis nor substantial extracts from it may be printed or otherwise reproduced without the author's permission.

L'auteur a accordé une licence non exclusive permettant à la Bibliothèque nationale du Canada de reproduire, prêter, distribuer ou vendre des copies de cette thèse sous la forme de microfiche/film, de reproduction sur papier ou sur format électronique.

L'auteur conserve la propriété du droit d'auteur qui protège cette thèse. Ni la thèse ni des extraits substantiels de celle-ci ne doivent être imprimés ou autrement reproduits sans son autorisation.

0-612-46950-6

Canada

University of Alberta

Library Release Form

Name of Author: DERONG YAN

Title of Thesis: THE INITIATION OF DELAYED HYDRIDE
CRACKING IN ZIRCONIUM-2.5 NIOBIUM

Degree: DOCTOR OF PHILOSOPHY

Year this Degree Granted: 1999

Permission is hereby granted to the University of Alberta Library to reproduce single copies of this thesis and to lend or sell such copies for private, scholarly, or scientific research purposes only.

The author reserves all other publication and other rights in association with the copyright in the thesis, and except as hereinbefore provided, neither the thesis nor any substantial portion thereof may be printed or otherwise reproduced in any material form whatever without the author's prior written permission.



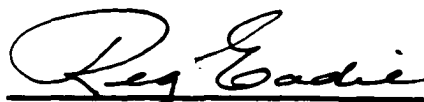
Derong YAN
Room 205, No. 43, Lane 250
Ling-Ling Road, Shanghai 200032
The People's Republic of China

Date: June 2, 1999

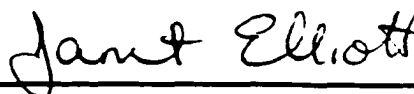
University of Alberta

Faculty of Graduate Studies and Research

The undersigned certify that they have read, and recommend to the Faculty of Graduate Studies and Research for acceptance, a thesis entitled **THE INITIATION OF DELAYED HYDRIDE CRACKING IN ZIRCONIUM-2.5 NIOBIUM** submitted by **DERONG YAN** in partial fulfillment of the requirements for the degree of **DOCTOR OF PHILOSOPHY** in **MATERIALS ENGINEERING**.



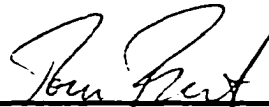
Dr. R. L. EADIE (Supervisor)



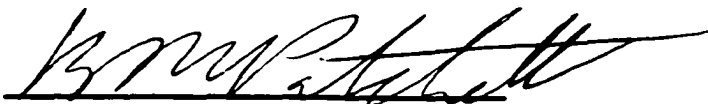
Dr. J. A. W. ELLIOTT



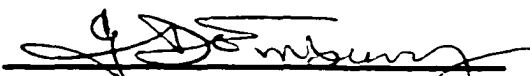
Dr. T. H. ETSSELL



Dr. T. W. FOREST



Dr. B. M. PATCHETT



Dr. J. D. EMBURY (External examiner)

Date: 99-5-27

TO MY PARENTS AND SISTER

ABSTRACT

This thesis contains two parts of work that study the initiation of the delayed hydride cracking (DHC) in zirconium alloys in different aspects.

The first part is a theoretical work in which the effect of stress on the hydride precipitation solvus in zirconium is studied from the view point of thermodynamics. The material equilibrium of a closed thermodynamic system which corresponds to a simplified model of hydride precipitation in zirconium is discussed using the internal energy minimization method. It is found that for the simplified model of hydride precipitation, the equation $dG = \delta W$ is an alternative expression for material equilibrium condition and can be used to study the effect of stress. Here dG is the change of the total Gibbs free energy of the system and δW the total mechanical work done on the system by the external stress. Applying this equation to the simplified hydride precipitation model, when stressed and non-stressed, respectively, the relation for the effect of the stress can be established. Solutions under different boundary conditions are derived and discussed. Based on these discussions, a general expression for the effect of external stress is obtained.

The second part is mainly an experimental work on the mechanism of the threshold stress intensity factor, K_{IH} , for the DHC in Zr-2.5wt% Nb alloys. A modified experimental method was developed and used in this work. In this modified method, the specimens are

fatigued between consecutive experiments, and the load is kept as a constant during the experiment. A new R-curve phenomenon related to the DHC initiation in Zr-2.5wt% Nb alloys has been observed and proposed for the first time. Based on this concept, the K_{IH} is more carefully defined from the view point of experiment. The hydride cluster lengths at different K_I are measured. Based on this work, the threshold phenomenon of DHC is explained, and some other phenomena are discussed. A qualitative micromechanical model which incorporates the effect of both stress and energy is proposed to explain the details of the K_{IH} mechanism and some other experimental phenomena.

ACKNOWLEDGEMENT

I would like to acknowledge and thank the following people that made the completion of this thesis possible and enjoyable:

First, to my supervisor Dr. Reg. L. Eadie for giving me the opportunity to work in this interesting research area, and for his support, encouragement, and guidance throughout the completion of this work and my study.

To Profs. J.D. Embury and G.R. Purdy for their comment and encouragement, and to Drs. M.P. Puls, D.R. Metzger, J.A.W. Elliott and C.Q. Ru for helpful discussion and comment, during the completion of the work given in chapter 3.

To Prof. J.D. Embury again for helpful discussion on the work given in chapter 4, and to the Chalk River Laboratory (CRL) of the Atomic Energy Canada Ltd. (AECL) for providing the alloy used in this work, and to Drs. C.E. Coleman and O.T. Woo, and other technical staff at CRL-AECL for the TEM analysis of the alloy. Also to G.K. Shek at the Ontario Hydro, to Debbie Reynolds and Peter Poruks for their assistance in preparing the specimens.

To Christina Barker, Bob Konzuk, Bob Smith, Jack Gibeau, Douglas Booth, Walter Boddez, Rob Stefaniuk, Clark Bicknell and Shiraz Merali for their interest in my work and very helpful technical assistance.

To the people in our group during my stay here: Milan Jovanović, Gang Lin, Yuehua Ma, Xiaolin Chen, Shumin Sun and Susan McFarland for discussion, support and especially the time we had in coffee break and picnic.

And, to the University of Alberta for scholarships and fellowships throughout my study, as well as to the Natural Sciences and Engineering Research Council of Canada (NSERC) for funding this research work.

TABLE OF CONTENTS

TABLE OF CONTENTS

CHAPTER 1. INTRODUCTION	1
1.1. INTRODUCTION TO Zr-2.5wt% Nb PRESSURE TUBE MATERIAL	2
1.1.1. Physical Properties of Zirconium	3
1.1.2. Zr-2.5wt% Nb Alloy and Its Microstructures	5
1.1.2.1. Phase Transformation	6
1.1.2.2. Microstructures	7
1.1.3. Mechanical Properties	8
1.1.3.1. Effect of Microstructures	8
1.1.3.2. Effect of Texture and Hydride Orientation	9
1.1.3.3. Effect of Temperature	11
1.1.3.4. Recovery and Recrystallization	12
1.1.3.5. Effect of Irradiation	13
1.2. THEORIES OF DELAYED HYDRIDE CRACKING	14
1.2.1. The Behaviour of Hydrogen in Zirconium	14
1.2.1.1. Zirconium-Hydrogen System	14
1.2.1.2. Hysteresis of Hydrogen Solvus in Zirconium Alloys	16
1.2.1.3. Mechanical Properties and Effect of Hydride	17
1.2.1.4. Diffusion of Hydrogen in Zirconium	18
1.2.1.5. Chemical Potential of Hydrogen Dissolved in Stressed Solid	19
1.2.2. Fracture Mechanics of Delayed Hydride Cracking	20
1.2.2.1. General Description of Stress Distribution at the Crack Tip	20
1.2.2.2. Effect of Plane Strain and Plane Stress Status on DHC	22
1.2.2.3. Stress Redistribution due to Hydrogen Diffusion and Hydride Precipitation	23

TABLE OF CONTENTS

1.2.3. Current Theoretical Model for Delayed Hydride Cracking	27
1.2.3.1. Hydrogen Diffusion	28
1.2.3.2. Hydride Formation	29
1.2.3.3. Hydride Cracking	30
1.3. INFLUENCING FACTORS ON THE DHC BEHAVIOUR OF Zr-2.5wt% Nb	
ALLOY	35
1.3.1. Effect of Microstructures	35
1.3.2. Effect of Texture	36
1.3.3. Effect of Temperature	37
1.3.3.1. Direction of Approach to Temperature (T_{DAT})	37
1.3.3.2. Crack Arrest Temperature (T_{CAT})	39
1.3.4. Effect of Thermal History	40
1.3.4.1. Thermal Ratchetting	40
1.3.4.2. Memory Effect	42
1.3.5. Effect of Stress Intensity Factor	43
1.3.6. Effect of Hydride Morphology	43
CHAPTER 2. OBJECTIVES	65
CHAPTER 3. THE EFFECT OF STRESS ON THE HYDRIDE	
PRECIPITATION SOLVUS IN ZIRCONIUM	67
3.1. INTRODUCTION	68
3.2. MATERIAL EQUILIBRIUM FOR STRESSED SOLIDS	71
3.2.1. Material Equilibrium in A Closed Thermodynamic System	71
3.2.2. An Alternative Expression of Material Equilibrium Condition	81
3.3. THE EFFECT OF STRESS ON HYDRIDE PRECIPITATION SOLVUS	
IN STRESSED ZIRCONIUM	86
3.4. CONSIDERATION OF A DIFFERENT BOUNDARY CONDITION	92

TABLE OF CONTENTS

3.5. DISCUSSION	96
3.6. CONCLUSIONS	99
 CHAPTER 4. THE MECHANISM OF K_{IH} IN DELAYED HYDRIDE CRACKING OF Zr-2.5wt% Nb AT 150°C	
4.1. INTRODUCTION	102
4.1.1. The K_{IH} Issues	102
4.1.2. The Objectives Of This Work	105
4.2. EXPERIMENTAL	107
4.2.1. Materials	107
4.2.2. Specimen Preparation	107
4.2.3. Experimental Equipment	108
4.2.4. K_{IH} Experiments	110
4.2.5. Post-Testing Examinations	111
4.3. RESULTS	113
4.3.1. R-Curve Phenomena	113
4.3.2. Length Of Hydride Clusters	115
4.3.3. Critical Length Of Hydride Cluster At Different Applied K_I	117
4.3.4. Effect Of Stress Level And Triaxiality	117
4.3.5. Fractography	119
4.4. DISCUSSION	121
4.4.1. R-Curve Phenomena	121
4.4.2. Length Of Hydride Clusters	124
4.4.3. Critical Length Of Hydride Cluster At Different Applied K_I	126
4.4.4. The Energy Required To Create The Fracture Surface Of The Hydride Cluster	127
4.4.5. Stage I/Stage II DHC Velocity	130
4.4.6. Absence Of Hydride Cluster At Low K_I	131

TABLE OF CONTENTS

4.4.7. Acoustic Emission Without Striation Formation And Partially Fractured Hydride Cluster	131
4.4.8. Measurement Of Hydride Cluster Length	135
4.5. CONCLUSIONS	137
CHAPTER 5. CONCLUSIONS	154
CHAPTER 6. FUTURE WORK	155
BIBLIOGRAPHY	157

LIST OF TABLES

LIST OF TABLES

	Page
Table 1.1. Typical physical properties of zirconium.	3
Table 1.2. Typical composition of Zr-2.5wt% Nb alloy.	5
Table 1.3. Crystal structure and lattice parameter of phases in zirconium alloys.	6
Table 1.4. Mechanical properties of annealed Zr-2.5wt% Nb sheet at room temperature.	10
Table 4.1. Composition of the Zr-2.5wt% Nb alloys used in this work.	107
Table 4.2. Summary of K_{IH} experiments in this work.	111
Table 4.3. Summary of the total number and average length of hydride clusters for the three experiments of the first category in section 4.3.1.	116
Table 4.4. Summary of experimental observations.	118
Table 4.5. Hardness of Zr-2.5wt% Nb alloys used in this work.	125
Table 4.6. The specific energy required to create the fracture surface (calculated from the experimental results in this work).	129

LIST OF FIGURES

LIST OF FIGURES

	Page
Figure 1.1. Influence of hydrogen on the relative change of lattice parameter a of α -zirconium.	46
Figure 1.2. Influence of niobium on lattice parameters of Zr-Nb alloys.	46
Figure 1.3. The zirconium-oxygen phase diagram.	47
Figure 1.4. The zirconium-niobium phase diagram: (a) the complete system; (b) the zirconium-rich portion.	48-49
Figure 1.5. The effect of niobium on the hardness increase during quenching and aging.	50
Figure 1.6. The effect of aging on the hardness of Zr-2.6wt% Nb.	50
Figure 1.7. The effect of cold work on the tensile properties of induction-melted sponge zirconium.	51
Figure 1.8. The texture in Zr-2.5wt% Nb alloys developed during rolling.	52
Figure 1.9. The effect of hydride and crystallographic orientation on the impact behaviour of Zircaloy-2.	53
Figure 1.10. The effect of temperature on the tensile properties of induction-melted sponge zirconium.	54
Figure 1.11. The stress-strain curve for short-time and 1000hr loading period at 260, 316, and 399°C.	55
Figure 1.12. The effect of temperature on the impact energy of zirconium (Charpy V-notch specimen).	55
Figure 1.13. The composite of general behaviour during recovery and recrystallization of 25% cold-worked zirconium annealed for 100 minutes at different temperatures.	56

LIST OF FIGURES

Figure 1.14.	The width of the (0004) X-ray diffraction peak of 20% cold-worked Zr-2.5wt% Nb after heating at different temperatures.	57
Figure 1.15.	(a) The zirconium-hydrogen phase diagram; (b) the high hydrogen content portion of the Zr-H phase diagram.	58
Figure 1.16.	Pressure-composition isotherms in the Zr-H system in the temperature range (a) 500-700°C; and (b) 800-850°C.	59
Figure 1.17.	The stress zones at the crack tip in plane strain.	60
Figure 1.18.	The rigid-plastic strip model for finite crack.	60
Figure 1.19.	(a) Stresses for the applied load L; (b) stresses for the reversed load DL; (c) stresses from superposition.	61
Figure 1.20.	A bright-field transmission electron micrograph showing typical grain structure in Zr-2.5% Nb pressure-tube material.	62
Figure 1.21.	The effect of cooling rate and maximum temperature on the total hydrogen level, $C_{H(tot)}$, at the peak stress location during temperature cycles of a Zr-2.5wt% Nb specimen containing 60 $\mu\text{g/g}$ hydrogen and a notch of depth 0.8 mm and tip radius 0.2 mm under net section stress of 300 MPa.	63
Figure 1.22.	Schematic diagram of the dependence of delayed hydride cracking velocity on stress intensity factor.	64
Figure 3.1.	Diagram illustrating the hydride (denoted as δ phase) precipitation from the zirconium matrix (denoted as α phase) under (a) no stress; (b) stress.	100
Figure 4.1.	The dimensions of a double cantilever beam (constant- K_I) specimen.	139
Figure 4.2.	Experimental results in first category when $K_I \geq 7.0 \text{ MPa}\sqrt{\text{m}}$.	140-141
Figure 4.3.	Experimental results in second category when $6.0 \text{ MPa}\sqrt{\text{m}} < K_I$	142-144

LIST OF FIGURES

	$< 7.0 \text{ MPa}\sqrt{\text{m}}$.	
Figure 4.4.	Experimental results in third category when $K_I \leq 6.0 \text{ MPa}\sqrt{\text{m}}$.	145-146
Figure 4.5.	Distance of crack front advance at different K_I .	147
Figure 4.6.	Length of hydride clusters along crack path.	148
Figure 4.7.	Critical hydride cluster length at different K_I .	149
Figure 4.8.	A partly fractured hydride cluster at crack tip, when $K_I = 7.0 \text{ MPa}\sqrt{\text{m}}$ (SEM).	150
Figure 4.9.	Fracture surface showing variation of crack length along specimen thickness direction.	151
Figure 4.10.	Comparison of critical hydride cluster length vs. applied K_I curves theoretically calculated and experimentally measured.	152
Figure 4.11.	A schematic showing critical hydride cluster lengths and the lengths of hydride clusters that grow at different diffusion times, at different K_I 's.	153

LIST OF SYMBOLS AND TERMINOLOGY

SYMBOLS AND TERMINOLOGY USED IN CHAPTER 3

- U, u - the internal energy, and the volume density of internal energy, respectively
- P - the atmospheric pressure
- V - the volume
- v - the ratio of the volume of a volume element after the infinitesimal deformation divided by its volume in the reference state before the infinitesimal deformation
- T - the temperature
- S, s - the entropy, and the volume density of entropy, respectively
- ρ - the volume density of mole number
- G - the Gibbs free energy
- R - the gas constant
- ϵ - the strain
- σ - the stress
- p - the air pressure; or the hydrostatic stress: $p = (\sigma_{ii} + \sigma_{jj} + \sigma_{kk})/3$
- \bar{u} , \bar{v} , \bar{w} - the three components of displacement with regard to a Cartesian coordinates
- α , β , γ - the three direction cosines of the normal of a surface element
- n - the mole number
- W - the mechanical work or strain energy

SYMBOLS AND TERMINOLOGY

- x_1, x_2 - the precipitation solvi (in molal fraction) of hydrogen in non-stressed and stressed zirconium, respectively
- x - the stoichiometric number of hydrogen in hydride ZrH_x (usually $x = 1.67$)
- μ - the chemical potential
- α - the zirconium matrix
- δ - the hydride
- \bar{G}_α^{n-s} - the molal Gibbs free energy of the non-stressed zirconium matrix
- \bar{G}_δ^{n-s} - the molal Gibbs free energy of the non-stressed hydride
- \bar{G}_α^a - the molal Gibbs free energy of the stressed zirconium matrix
- \bar{G}_δ^a - the molal Gibbs free energy of the stressed hydride
- $\mu_{H,\alpha}^{n-s}$ - the chemical potential of hydrogen in the non-stressed zirconium matrix.
- $\mu_{H,\alpha}^a$ - the chemical potential of hydrogen in the stressed zirconium matrix
- $\bar{V}_{H,\alpha}$ - the partial molal volume of hydrogen in zirconium
- $\bar{V}_{\alpha-\delta}$ - the volume increase when one mole of zirconium matrix absorbs x moles of hydrogen and forms one mole of hydride ZrH_x
- \bar{W}_α^a - the strain energy per mole of the stressed zirconium matrix
- \bar{W}_δ^a - the strain energy per mole of the stressed hydride
- $\bar{W}_{\alpha-\delta}^{a-inc}$ - the total change in strain energy of the system under external stress during the hydride formation, which is measured considering one mole of hydride is formed in this way
- \bar{G}_δ^{a-inc} - the molal Gibbs free energy of hydride under the external stress which is

SYMBOLS AND TERMINOLOGY

modified by the formation of hydride precipitates. Here the molal Gibbs free energy is a mole average value, since the stress and strain throughout this hydride phase may not be uniform

$\overline{G}_{\alpha'}^{a+inc}$ - the molal Gibbs free energy of the zirconium matrix after hydride transformation, α' denoting the zirconium with a lower hydrogen concentration than original due to hydride formation, and 'a+inc' denoting the external stress which is modified by the formation of the hydride precipitates. Here the molal Gibbs free energy is a mole average value, since the stress, strain, and hydrogen concentration etc. throughout this zirconium phase may not be uniform

closed thermodynamic system

- a thermodynamic system that has no mass transfer with its surroundings
 - in this chapter, it refers to: the α -Zr with interstitial hydrogen, and the hydride.
- This closed system may have heat transfer, P-V work, and mechanical work (through external stress) with its environment, but it does not have mass transfer with its environment

system I- in section 3.2 of this work, the above closed system is denoted as 'system I'

isolated thermodynamic system

- a thermodynamic system that does not interact in any way with its surroundings

SYMBOLS AND TERMINOLOGY

- in this work, it includes the closed system mentioned above, the loading system (the source of applied stress), and the air (which gives the P-V work) in between the boundary of the closed system and the wall of the isolated system

system II- in section 3.2.1 of this work, the above isolated system is denoted as 'system II'

environment

- in this work, it refers to: the existence outside the closed system and inside the isolated system. This includes both the loading system and the air. In section 3.2.1 of this work, it is denoted by a subscript 'env'

- here the term 'environment' instead of 'surroundings' is used, in order to specify that this refers to the 'surroundings' of the closed system (or system I) and not that of the isolated system (or system II)

SYMBOLS USED IN CHAPTER 4

K_I - the stress intensity factor, in $\text{MPa}\sqrt{\text{m}}$

K_{IH} - the threshold stress intensity factor, below which the delayed hydride cracking cannot happen, in $\text{MPa}\sqrt{\text{m}}$

r_p - the plastic zone size at crack tip, in μm

σ_{ys} - the yield stress, in MPa

G_c - the *specific* energy required to create the fracture surface, in J/m^2 . See section

SYMBOLS AND TERMINOLOGY

4.4.4 for details

L_c - the critical hydride cluster length, in μm . See sections 4.3.3 and 4.4.3 for details

ν - Poisson's ratio

E - Young's modulus, in MPa

l_{gl}, t_{gl} - the maximum length for hydride cluster growth when fracture is not considered, and the required time, respectively. See section 4.4.5 for details

CHAPTER 1. INTRODUCTION

In the 1950s, three nuclear reactors were built in Ontario, Canada [1]. These nuclear reactors used heavy water as the moderator, and zirconium alloy pressure tubes in their major cooling system. The operating conditions for these pressure tubes were very severe. During the operation, the pressure tubes endured a pressure of about 100 atm inside the tube. The zirconium alloy used was Zircaloy-2 at first. Later, in order to reduce the pressure tube wall thickness, a stronger zirconium alloy, Zr-2.5wt% Nb, was introduced. Since the 1970s, following the observation of pressure tube crackings in Pickering Unit 3 (1974), extensive research has been conducted in the area of delayed hydride cracking (DHC) in Zr-2.5wt% Nb alloy.

1.1. INTRODUCTION TO Zr-2.5wt% Nb PRESSURE TUBE MATERIAL

In 1947, the U.S. Bureau of Mines developed the zirconium sponge process [2]. Zirconium sand (zirconium silicate, $ZrSiO_4$) was melted with graphite to form zirconium carbon nitride. This compound was chlorinated and then reduced by magnesium to form magnesium chloride and zirconium which were separated by a distillation process. The zirconium product was zirconium sponge, which was broken into small lumps. The sponge was compacted together with alloying elements, and melted in an arc furnace to form an ingot. Ingots were usually double arc melted to homogenise the alloy and then forged in preparation for further processing into bar, sheet or extrusion billets. For zirconium used as nuclear reactor pressure tube material, a special process to remove the hafnium, an element which occurs naturally with zirconium in its ore, must be undertaken, because of the high neutron absorption cross section of hafnium.

Because of its combination of mechanical properties and low neutron absorption cross section, zirconium was selected as the pressure tube material for the cooling system in nuclear reactors.

1.1.1. Physical Properties of Zirconium

Typical physical properties of zirconium are summarized in table 1.1 [2-4].

Table 1.1. Typical physical properties of zirconium

Parameters	Value or property
Atomic number	40
Atomic weight	91.2
Density (300K)	$6.5 \cdot 10^3 \text{ kg/m}^3$
Melting temperature	2125K (1850°C)
Transition temperature $\alpha \rightleftharpoons \beta$	1135K (862°C)
Specific heat (300K)	276 J/kg·K
Thermal conductivity (300K)	20 J/m·sec·K
Thermal neutron capture cross-section	0.8 m^{-1}
Electric resistivity	$0.44 \mu\Omega\text{-m}$
Young's modulus (300K)	[1120] direction, 99 GPa [0001] direction, 125 GPa
Poisson's ratio (300K)	0.35
Lattice parameters (300K)	
hexagonal closed-packed α	$a_0 = 0.323 \text{ nm}, c_0 = 0.515 \text{ nm}$
body-centered cubic β	$a_0 = 0.359 \text{ nm}$

Upon cooling, the body-centered cubic (bcc) β zirconium transforms into the hexagonal closed-packed (hcp) α zirconium. The crystallography of the $\beta \rightarrow \alpha$ transformation of crystal bar (high purity) zirconium was reported [5-7] to have the following relationship:

$$(0001)_\alpha // \{110\}_\beta \text{ and } \langle 11\bar{2}0 \rangle_\alpha // \langle 111 \rangle_\beta.$$

Lloyd [8] measured the lattice parameters of single crystal α zirconium with dilatation interferometry from room temperature to 860°C. The interference technique gave changes in dimensions but not absolute values, and hence Lloyd used the room temperature parameter values of Lichter [9] for reference constants. The combination of their studies gave an accurate description of the temperature dependence of the lattice parameters, as given by:

$$a_0 = 0.323118 + 1.6626 \times 10^{-6} (T - 25),$$

$$c_0 = 0.514634 + 4.7413 \times 10^{-6} (T - 25),$$

where a_0 and c_0 are in nm, and T is the temperature in °C. It is seen from the two equations that when the temperature is below 400°C, the change of lattice parameters due to temperature is less than 0.1% per 100°C and is anisotropic.

Lichter [9] studied the relationship between the lattice parameters of α zirconium and the atomic percentage of oxygen in the range 0 to 5 at%, and gave:

$$a_0 = 0.323168 + 0.01099m \pm 1.9 \times 10^{-5},$$

$$c_0 = 0.514764 + 0.02077m \pm 3.9 \times 10^{-5},$$

where a_0 and c_0 are in nm, and m is the percentage of oxygen in at%.

Espagno *et al.* [10] reported the effect of hydrogen on the relative change in a_0 . It appeared that the parameter increased linearly with hydrogen content up to the solubility limit

in the temperature range 340-560°C, as given in figure 1.1. Beck [11] reported values of $a_0 = 0.32335$ nm and $c_0 = 0.51520$ nm for hydrogen-saturated α zirconium at room temperature.

Richter *et al.* [12] studied the effect of niobium on the lattice parameters of α -zirconium and found that niobium decreases both the a_0 and c_0 of α -zirconium, as given in figure 1.2. There was virtually no change in the axial ratio, a value of 1.5931 being obtained for Zr-1wt% Nb compared to 1.5926 for pure zirconium.

1.1.2. Zr-2.5wt% Nb Alloy and Its Microstructures

The most common commercial zirconium alloys are Zircaloy-2, Zircaloy-4, Zr-1wt% Nb and Zr-2.5wt% Nb. The alloy of interest in this work is Zr-2.5wt% Nb, whose composition is given in table 1.2. The Zr-O and Zr-Nb partial phase diagrams are given in figure 1.3 [2] and figure 1.4 [12, 13]. The oxygen stabilizes the hexagonal α phase, and niobium stabilizes the cubic β phase.

Table 1.2. Composition of a typical Zr-2.5wt% Nb alloy

	Zr	Nb	Sn	Fe	Cr	Ni	Mo	O ($\mu\text{g/g}$)	H ($\mu\text{g/g}$)
Wt %	balance	2.6	0.0025	0.05	0.01	0.0035	0.0025	1200	5

1.1.2.1. Phase Transformation

Many zirconium alloys undergo athermal and/or isothermal β decomposition to transition phases before the equilibrium phases form. Two of the most common transition structures are the martensitic α' phase and the ω phase. The martensitic structure is a distorted α zirconium supersaturated with solute, and the ω structure is a primitive hexagonal cell with c_0/a_0 ratio of about 0.62 [4]. The crystallography and the lattice parameters of different phases in Zr-Nb alloys are given in table 1.3.

Table 1.3. The crystallographic structure and lattice parameters of phases in zirconium alloys

Phases	Lattice parameters (nm)
α hexagonal closed-packed	$a_0 = 0.323, c_0 = 0.515, c_0/a_0 = 1.59$
α' hexagonal closed-packed	$a_0 = 0.325, c_0 = 0.522, c_0/a_0 = 1.61$
ω hexagonal closed-packed	$a_0 = 0.504, c_0 = 0.313, c_0/a_0 = 0.621$
β -Zr body centered cubic	$a_0 = 0.359$
β -Nb body centered cubic	$a_0 = 0.330$

The ω phase in zirconium alloys forms either by aging of a quenched β phase or directly by quenching. The ω phase is metastable and will ultimately convert to the stable α phase plus the body centered cubic phase. The metastable ω has a hexagonal structure with an axial ratio of 0.622 ± 0.002 , regardless of composition [14]. The lattice parameters are about a_0

= 0.502 nm and $c_0 = 0.300$ nm. The actual lattice parameters will vary with both composition and aging temperature. The ω phase is oriented with the β phase according to

$$\langle 0001 \rangle_{\omega} // \langle 111 \rangle_{\beta} \text{ and } \langle 2\bar{1}\bar{1}0 \rangle_{\omega} // \langle \bar{1}01 \rangle_{\beta}.$$

The martensitic transformation is characterized by a M_s temperature at which the reaction starts upon cooling. This temperature is a function of composition and generally decreases with increasing solute in the β phase for substitutional solutes, and may decrease or increase with increasing content of interstitial solutes. There have been no cases reported for isothermal formation of martensite in zirconium alloys.

1.1.2.2. Microstructures

According to the above phase transformation theory, one may predict the complex microstructures of Zr-2.5wt% Nb alloy, by its thermal history:

- (1) In the annealed condition, it has a microstructure of equiaxed α grains with β phase at the grain boundaries.
- (2) When the alloy is slowly cooled from the β phase into the $(\alpha + \beta)$ phase region, α nucleates at the β grain boundaries and then grows to form a Widmanstätten structure.
- (3) When it is slowly cooled from the $(\alpha + \beta)$ phase region, β phase transforms into α phase by growing on the existing α phase. The remaining β becomes enriched in Nb and when it contains about 17-20 wt% Nb, it is metastable down to the room temperature. Hence the

microstructure consists of α grains and a network of β -zirconium which contains 17-20 wt% Nb at the α grain boundaries.

- (4) If it is heated into the β phase and water quenched, the β phase transforms into α' which has a martensitic structure. Heating α' below the monotectoid temperature 610°C will precipitate β -Nb phase within the α' needles and also at the twin boundaries, and the α' transforms into equilibrium α phase.
- (5) The metastable hexagonal ω phase forms either by quenching the β phase or by aging a Nb-enriched β phase. The β must contain about 7 wt% Nb before ω can form. This can be achieved by quenching from the ($\alpha+\beta$) phase region when β phase is enriched with Nb.

1.1.3. Mechanical Properties

1.1.3.1. Effect of Microstructures

The Zr-2.5wt% Nb alloy exhibits martensitic hardening. The formation of ω -phase during the cooling also results in very substantial strengthening. The metastable α' and ω decompose during thermal treatment at slightly elevated temperatures and usually give rise to additional hardening by aging. Winton *et al.* [15] studied the Zr-Nb system for its variations in mechanical properties during tempering. The effect of niobium content on the hardness in quenched and tempered samples is given in figure 1.5. Tempering (aging) causes a depletion in

the niobium content of the α' , which will decrease the strength. But, along with the loss of strength due to niobium depletion, there is a strengthening by the coherent precipitation of the Nb-enriched phase. The interaction of these two effects results in the hardness change as shown in figure 1.6 [15].

Cold work produces a dislocation substructure, which will affect the mechanical properties. The effect of cold work on the tensile properties of sponge zirconium is shown in figure 1.7 [16]. It is apparent that cold work has its major effect on properties in the first 20% reduction.

1.1.3.2. Effect of Texture and Hydride Orientation

Effect of Texture

The hexagonal crystal structure of α -zirconium results in anisotropic mechanical properties. When a Zr-2.5wt% Nb alloy is rolled into sheets, a texture is developed by the hexagonal α grains, as shown in figure 1.8 [17]. The tensile properties of an annealed Zr-2.5wt% Nb sheet in the longitudinal, transverse and short transverse directions are given in table 1.4 [17]. The orientation of the hexagonal α grains relative to the axes of the tensile specimens is similar in the longitudinal and transverse specimens, and hence their mechanical properties are also similar. In the short transverse specimens, the c-axis of the hexagonal α -

zirconium is preferentially oriented along the tensile axis and the sheet is strongest in that direction.

Table 1.4. The room temperature mechanical properties of an annealed Zr-2.5wt% Nb sheet [17]

Specimen direction	0.2% Y.S. (MPa)	U.T.S (MPa)	% Elongation
Longitudinal	380	500	27
Transverse	470	500	22
Short transverse	520	540	17

Effect of Hydride Orientation

It was found that the orientation of hydride platelets was more important than the total hydrogen content in the samples.

Douglass [18] presented some graphs to show that, when the hydride platelets were parallel to the drawing (longitudinal) direction and the radial direction in cold-worked Zircaloy-2 tube material, the impact-energy absorption was much smaller at room temperature in the transverse direction than in the longitudinal direction as shown in figure 1.9. This is because in the transverse direction the hydride platelets were parallel to the fracture path and provided a notch effect.

Louthan *et al.* [19] reported that tensile ductility of Zircaloy-2 and Zircaloy-4 was drastically reduced when hydrides were oriented perpendicularly to the direction of the tensile stress.

The concept of effective hydrogen content was proposed [20], which was defined as the total hydrogen content multiplied by the fraction of hydride platelets lying between 50° and 90° to the stress direction. This effective hydrogen content has a similar meaning to another parameter, hydride continuity coefficient [21], which describes the degree the hydrides have oriented in the radial-axial plane of the tube wall material. The former refers directly to tensile stress direction, whereas the latter refers to a particular plane of the tube wall material. When, in the latter case, the tensile stress is perpendicular to the radial-axial plane of the tube wall, then the two parameters are interchangeable.

1.1.3.3. Effect of Temperature

On the Tensile Properties

The effect of temperature on the tensile properties of sponge zirconium is shown in figure 1.10 [2]. The effect of temperature on the stress-strain curve under different strain-rates is shown in figure 1.11 [22]. At lower temperatures, the plastic behaviour of annealed zirconium is relatively independent of time, but the time factor becomes an important variable at 399°C . From these graphs, it is seen that at temperatures near 400°C and higher, it is necessary to specify both the temperature and the strain-rate in reporting tensile properties.

On the Impact Properties

The V-notched Charpy impact energy of nominally pure zirconium, and zirconium with different hydrogen contents varies with temperature as shown in figure 1.12 [2]. It is obvious that temperature has a much stronger effect on the impact energy of zirconium containing hydrogen than those with nominally no hydrogen content.

1.1.3.4. Recovery and Recrystallization

The recovery, recrystallization and grain growth behaviour of 25% cold-worked zirconium is shown in figure 1.13 [4]. These behaviours can be studied by using microscopic examination, hardness measurement, electrical resistivity, and X-ray line-width measurement.

Recovery

Recovery is affected by the prior amount of cold work. Recovery is very slow below 300°C and very rapid above 600°C. Between 300-600°C, the rate of recovery is faster the greater the amount of previous cold work.

Measurement of the width of (0004) α -phase diffraction peaks of cold-worked Zr-2.5wt% Nb, as shown in figure 1.14 [23], indicates:

- (1) At 300°C recovery is slow.

-
- (2) At 500°C and 600°C, there is a rapid partial recovery followed by a much slower rate. The higher the temperature, the greater the initial recovery.
- (3) Temperature higher than 600°C is required for full recovery in less than thousands of hours.

Recrystallization

The temperature at which recrystallization begins is a function of cold work, purity and time. Johnson [2] studied the effect of short-time annealing on sponge zirconium which had been cold-rolled by 25 and 65%, respectively. It was found that an annealing time of 1/4 minute at 800°C was sufficient to cause considerable recrystallization in 25% cold-rolled metal, with the 0.2% yield stress decreasing from about 550 MPa to about 290 MPa. Complete recrystallization took place within 2 minutes for both degrees of cold work. Johnson's results indicate that short-time annealing at 750-800°C is sufficient in eliminating the effect of cold work.

1.1.3.5. Effect of Irradiation

Neutron irradiation increases the strength of zirconium alloys and reduces their ductility. The change in properties is related to the neutron exposure. Irradiation temperature, microstructures (heat-treatment, and cold-work, *etc.*) and compositions of the alloys all affect the change of properties with irradiation.

1.2. THEORIES OF DELAYED HYDRIDE CRACKING

1.2.1. The Behaviour of Hydrogen in Zirconium

1.2.1.1. Zirconium-Hydrogen System

Solvus Line of Hydrogen in Zirconium

Zirconium and zirconium alloys absorb a large quantity (up to 5 at% or 540 $\mu\text{g/g}$) of hydrogen in solid solution when the temperature is as high as 502°C, as shown in figure 1.15 [4]. The hydrogen solubility in zirconium exhibits an Arrhenius relationship with temperature [24], and decreases rapidly with decreasing temperature. The excess hydrogen precipitates as a hydride phase. There are three stoichiometric hydride phases:

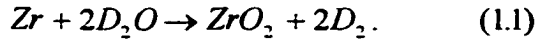
- (1) γ - face centered tetragonal (Zr-H_x , $x = 1.5$ to 1.67)
 - formed on fast cooling
- (2) δ - face centered cubic (Zr-H_x , $x = 1.5$ to 1.67)
 - formed on slow cooling
- (3) ϵ - face centered tetragonal (Zr-H_x , $x > 1.67$)

Vapour Pressure

The vapour pressure of hydrogen in equilibrium with zirconium hydrides has been studied by Libowitz [25]. The results are shown in figure 1.16 for the temperature range of 500-850°C. From these curves, one can see that decreasing the temperature drastically decreases the hydrogen pressure in equilibrium with zirconium hydrides. Therefore, although the data for temperatures below 500°C are not available, one can expect that the hydrogen pressure in equilibrium with zirconium hydrides in the temperature range of 200- 400°C will be very small. Usually, there is an oxide layer on the surface of zirconium alloys, which will prevent the hydrogen from entering and/or leaving the alloy. Hence, we may assume that the hydrogen dissipation from the specimens when holding at a certain test temperature (usually below 400°C) to be very small and there will be no significant drop in hydrogen concentration of the specimen.

Source of Hydrogen

The fabrication process for zirconium alloys is usually controlled so that the hydrogen concentration in finished products is lower than 10 µg/g. In nuclear reactors, however, the zirconium alloys are used in contact with heavy water. The corrosion reaction forms zirconium oxide, and releases deuterium by the reaction:



Some of the deuterium enters the zirconium alloys in atomic form as an interstitial solute. In the study of DHC, hydrogen is usually charged into the specimens and used as a surrogate for the deuterium.

1.2.1.2. Hysteresis of Hydrogen Solvus in Zirconium Alloys

Slattery [26] determined the solvi of hydrogen in Zircaloy-2, Zircaloy-4 and Zr-2.5wt% Nb alloys using the dilatometric method. According to Slattery's study, the solvi of hydrogen in Zr-2.5wt% Nb differ during heating and cooling. These solvi are usually referred to as the dissolution solubility C_H^d and the precipitation solubility C_H^p , and are given, respectively, by

$$C_H^d = 6.86 \times 10^4 \exp\left(-\frac{33763}{RT}\right), \quad (1.2)$$

$$C_H^p = 4.11 \times 10^4 \exp\left(-\frac{28002}{RT}\right), \quad (1.3)$$

where C_H^d and C_H^p are in $\mu\text{g/g}$, R is the gas constant 8.314 J/mol-K and T is the temperature in Kelvin. The temperature range in which these equations were obtained experimentally was 200-400°C.

The difference between the solvi during heating and cooling is mainly due to the plastic deformation and surface energy involved in the hydride precipitation process.

1.2.1.3. Mechanical Properties and Effect of Hydride

The stoichiometric hydrides are so brittle and weak ($100 \text{ MPa} < \text{U.T.S.} < 200 \text{ MPa}$) that a tensile test on them has little real meaning [27]. Therefore, hydride phases generally have a deleterious effect on the mechanical behavior of zirconium alloys. This deleterious effect is particularly evident at temperatures $< 150^\circ\text{C}$. In general, the deleterious effect increases as:

- (1) temperature falls below 150°C ;
- (2) hydrogen concentration increases;
- (3) hydrides become larger;
- (4) hydride platelets align more perpendicularly to the tensile stress axis.

In evaluating the effect of hydride platelet orientation, it is convenient to have a quantitative description of the extent of orientation. A parameter, f_x , is defined as the percentage of hydride platelets, whose plane normal makes an angle with a reference direction in the range between x° - 90° . A higher f_x value leads to a lower tensile ductility when the stress axis is parallel to the reference direction.

Three factors, alone or in combination, affect the hydride orientation:

- (1) crystallography - within a given grain, some habit planes are preferred, *e.g.* (0001);
- (2) cold work - hydride platelets tend to form parallel to the rolling plane;
- (3) stress - hydride platelets tend to orient with their normals perpendicular to an existing tensile stress.

1.2.1.4. Diffusion of Hydrogen in Zirconium

The diffusion of hydrogen is affected by hydrogen concentration, temperature gradient and stress gradient, as described in the general diffusion equation:

$$J = -\frac{DC}{RT} \left[RT \frac{d \ln C}{dx} + \frac{Q^*}{T} \frac{dT}{dx} - \bar{V}_H \frac{dp}{dx} \right], \quad (1.4)$$

where

J is the hydrogen flux;

D is the diffusivity of hydrogen in the metal;

R is the gas constant;

T is the temperature in Kelvin;

C is the hydrogen concentration at any point x;

Q* is the heat of hydrogen transport in the metal;

\bar{V}_H is the partial molal volume of hydrogen in the metal;

p is the hydrostatic stress $(\sigma_{xx} + \sigma_{yy} + \sigma_{zz})/3$, σ_{xx} , σ_{yy} and σ_{zz} being the principal stresses.

The diffusion coefficient for hydrogen in α -zirconium is given by [28]:

$$D = 2.17 \times 10^{-7} \exp\left(-\frac{35079}{RT}\right), \quad (1.5)$$

where D is in m^2/s , R = 8.314 J/mol·K, and T is temperature in Kelvin.

Diffusion in a Concentration Gradient

(1) In α phase

Sawatzky [28] gave the expression of diffusion coefficient over the temperature range 260-560°C as in equation (1.5).

(2) In β phase

Hydrogen diffusion in β -zirconium was studied by Gelezunas [29], who obtained the diffusion coefficient for the temperature range 760-1010°C as:

$$D = 5.32 \times 10^{-7} \exp\left(-\frac{34828}{RT}\right), \quad (1.6)$$

where D is in m^2/s , $R = 8.314 \text{ J/mol}\cdot\text{K}$, and T is in Kelvin.

Thermal Diffusion

Markowitz [30] considered the problem of thermal diffusion of hydrogen in the two-phase structure of α -zirconium and δ -hydride in Zircaloy-2. The hydrogen migrated to the cold side of the sample under a thermal gradient. Dissolution of hydride occurred at the hot side, and precipitation of the hydride occurred at the cold side. The value of heat of transport Q^* obtained was between 1.6 - 6.5 kcal/mol.

1.2.1.5. Chemical Potential of Hydrogen Dissolved in Stressed Solid

The chemical potential of hydrogen dissolved in stressed solids is given by [31]:

$$\mu_H^s = \mu_H^{n-s} - p \cdot \bar{V}_H, \quad (1.7)$$

where μ_H^s and μ_H^{n-s} are the chemical potential of hydrogen in stressed and non-stressed solids, respectively, \bar{V}_H is the partial molal volume of hydrogen in the solid, and p is the hydrostatic stress.

Equation (1.7) is derived under the assumption of small elastic deformation. It is also assumed that the dilation of the solid caused by per mole addition of hydrogen is the same for x , y , and z directions, and the effect of hydrogen addition on the compliances of the solid are ignored.

1.2.2. Fracture Mechanics of Delayed Hydride Cracking

1.2.2.1. General Description of Stress Distribution at the Crack Tip

The stress distribution near the crack tip in a Zr-2.5wt% Nb alloy has been summarized by Eadie *et al.* [32].

Under plane strain conditions, four zones have been defined near the crack tip, according to their stress-strain relationship [33], as illustrated in figure 1.17. They are: a process zone within 2δ of the tip, where $\delta = K_I^2/E\sigma_{ys}$ is the crack opening displacement (COD); a plastic annulus beyond 2δ for a short distance within which the Hutchinson-Rice-Rosengren (HRR) [34-35] solution is valid; the plastic zone outside the plastic annulus within which there

is significant plasticity; and the region outside the plastic zone where the linear elastic fracture mechanics solution is valid.

(1) Process zone

In the process zone, its proximity to the singularity point will increase the stresses, but on the other hand its closeness to the crack surface also relaxes the triaxiality of the plane strain conditions. The stress and strain in the process zone are not fully understood, because of the very large strains involved.

(2) Plastic annulus

In the plastic annulus region, the HRR singularity solution [36-38] can be used to describe the stresses for power hardening materials when the elastic strains are negligible compared to the plastic strains. Calculation of the HRR stresses for Zr-2.5wt% Nb at 250°C [39] gives the peak hydrostatic stress $p = (\sigma_{xx} + \sigma_{yy} + \sigma_{zz})/3$ at 2δ from the crack tip to be $2.6\sigma_{ys}$, where σ_{ys} is the yield stress. The zone where the HRR singularity applies decreases with increasing strain-hardening exponent n .

(3) Plastic Zone

The boundary of plastic zone under plane strain conditions is given approximately as [33]:

$$r(\theta) = \frac{K_I^2}{4\pi\sigma_{ys}^2} [(1 - 2\nu)^2 (1 + \cos\theta) + \frac{3}{2} \sin^2 \theta], \quad (1.8)$$

where K_I is the stress intensity factor and ν is the Poisson ratio.

(4) Linear Elastic Zone

Beyond the plastic zone, the linear elastic fracture mechanics solution applies, and the stresses are described by:

$$\begin{aligned}\sigma_{xx} &= \frac{K_I}{\sqrt{2\pi r}} \cos \frac{\theta}{2} \left(1 - \sin \frac{\theta}{2} \sin \frac{3\theta}{2}\right), \\ \sigma_{yy} &= \frac{K_I}{\sqrt{2\pi r}} \cos \frac{\theta}{2} \left(1 + \sin \frac{\theta}{2} \sin \frac{3\theta}{2}\right), \\ \sigma_{xy} &= \frac{K_I}{\sqrt{2\pi r}} \sin \frac{\theta}{2} \cos \frac{\theta}{2} \cos \frac{3\theta}{2}, \\ \sigma_{zz} &= \nu(\sigma_{xx} + \sigma_{yy}),\end{aligned}\quad (1.9)$$

where plane strain conditions are assumed.

1.2.2.2. Effect of Plane Strain and Plane Stress Status on DHC

Dutton *et al.* [40] recognized that in plane strain conditions, the stresses at the crack tip are elevated by the triaxiality caused by the through-thickness constraint. By following Rice *et al.* [41], they gave the peak stresses close to the crack tip to be:

$$\sigma_{xx} = 1.8\sigma_{ys}, \quad \sigma_{yy} = 3.0\sigma_{ys}, \quad \sigma_{zz} = 2.4\sigma_{ys}, \quad (1.10)$$

where σ_{ys} is the uniaxial yield stress, y is normal to the cracking plane and x is the cracking direction. Therefore, the peak hydrostatic stress p was $2.4\sigma_{ys}$.

In fracture tests, the required thickness of specimens to ensure plane strain conditions is given by [42]:

$$t \geq 2.5 \left(\frac{K_I}{\sigma_{ys}} \right)^2. \quad (1.11)$$

At 150°C, the yield stress of the Zr-2.5wt% Nb alloys used in this work was approximately 600 MPa. When $K_I = 15 \text{ MPa}\sqrt{\text{m}}$, one has $t_{\min} = 1.6 \text{ mm}$. This means that within the stress intensity factor K_I range ($< 15 \text{ MPa}\sqrt{\text{m}}$) we used in our K_{IH} tests, the specimens were under plane strain status. Therefore the peak stresses given in equation (1.10) applied to the situations in our K_{IH} tests.

Near the specimen side surfaces at the crack tip, plane stress conditions dominate due to the lack of constraint in the through-thickness direction. Therefore, the hydrostatic stress p near the specimen side surfaces is smaller than that inside the specimen. Since the hydrogen tends to diffuse to the specimen region with higher hydrostatic stress, hydrides will first form at the mid-thickness region at the crack tip where the hydrostatic stress p is the highest. With this situation further worsened by the higher triaxiality of stresses, cracking will initiate at this region. This may account for the "tongue" shape of the cracking front, the so called "tunnelling" effect, observed in thick specimens.

1.2.2.3. Stress Redistribution due to Hydrogen Diffusion and Hydride Precipitation

Stress Redistribution due to Hydride Precipitation

Due to the difference in molal volume of zirconium matrix containing hydrogen and zirconium hydride, there will be a dilation of volume when zirconium matrix containing

hydrogen transforms into zirconium hydride. In the early modeling of stress distribution at the crack tip, the effect of hydride precipitation on the stress redistribution was not taken into account. As Simpson *et al.* [43] put it, "more details on the alterations of the crack-tip stress field by the precipitation event are required".

This concern had lasted for at least ten years, until Eadie *et al.* [44] proposed an approach to establish a qualitative picture of the stress change due to the hydride precipitation. They introduced the rigid-plastic strip model, developed by Rice [45, 46] for the elastic perfectly-plastic case. The geometry of the model is shown in figure 1.18. Under the elastic perfectly-plastic assumption, the stresses beyond the plastic zone are pure elastic, and the magnitude of the stresses in the plastic zone, *i.e.* $a < |x| < a + \omega$, is equal to the yield stress. They suggested that there is a region of dilation in the plastic zone due to the hydride precipitation. The dilation can be simulated by adding a tensile stress ahead of the crack tip, as illustrated in figure 1.19. The Westergaard [47] stress function $F(z)$, plus the boundary condition: $\sigma_y = 0$, for $|x| < a$; $\sigma_y = \sigma_{ys}$, for $a < |x| < a + \omega$; and $V_y = 0$, for $|x| \geq a + \omega$, V_y being the displacement in the y direction, were used to obtain the analytical expression for stress distribution. And based on an equation of Rice [45], the plastic zone size ω was determined to be 108 μm . In their calculation, a crack length of 10 μm , $K_I = 10 \text{ MPa}\sqrt{\text{m}}$ and $\sigma_{ys} = 606 \text{ MPa}$ were used. The hydride length and thickness were assumed to be 100 μm and 2.5 μm respectively based on the experimental observation [48], and a strain of 0.17 perpendicular to the hydride platelet based on Weatherly's work [49] was adopted. The

importance of this work is that it pointed out the dilation effect due to the hydride precipitation just ahead of the crack tip.

By an elastoplastic finite element analysis, Ellyin *et al.* [50] numerically studied the change in stress and strain due to the hydride precipitation at the crack tip. They incorporated a rate-independent elastoplastic model into a finite element code, assuming a stationary crack subject to different loadings, and with a further refinement in which the material is assumed to be initially isotropic and the anisotropy develops due to plastic deformation. The advantage of this constitutive model is that it uses the uniaxial stress-strain curve to determine the tangent modulus E_t and hardening modulus g . Therefore, any effect of microstructure reflected in the uniaxial stress-strain curve is included in the constitutive model. In their model, two types of stress hypersurfaces, yield and memory surfaces, were used to describe the yield locus development. This gives a prediction of the direction of the motion of yield surface that is in better agreement with experimental results, compared with other existing models. They concluded, by FEM calculation, that hydride precipitation causes an elastic unloading in front of the crack. As the hydride platelet becomes longer, the peak normal stress at the front end (the end of hydride platelet closer to the crack tip) of the hydride will increase, while the peak normal stress at the back end of the hydride will decrease. As the hydride platelet becomes thicker, the situation is just the opposite: the peak normal stress at the front end will decrease and the peak normal stress at the back end will increase. The initial location of the hydride formation relative to the crack tip has little effect on the above conclusion, according to their calculation. The normal stress is the stress perpendicular to the cracking plane.

Later, Metzger *et al.* [51] developed a stepwise coupled diffusion/stress FEM model to study the effect of hydride precipitation on stress redistribution, hydrogen diffusion, and hence the morphology of hydride precipitate at the crack tip. In his calculation, firstly a crack tip is loaded to provide the initial stress distribution which will be used for diffusion analysis. Then when diffusion causes a certain amount of hydride precipitation, the volume dilation caused by this hydride is considered and a new stress distribution is obtained. With the new stress distribution, diffusion analysis is resumed until another small amount of hydride is formed. This process is repeated as the hydride grows. This model has the advantage that no previous assumption for the geometry of hydride is required, and the calculation will automatically give the most probable shape of the hydride formed. Metzger's calculation indicated that a tapering hydride was expected along the cracking plane, and as the hydride grew, the peak for both the hydrostatic stress and the normal stress became flattened and elongated. No compressive stress zone, which was an inevitable result in Ellyin *et al.*'s [50] calculation, is observed at the hydride region. Metzger's model is probably closer to the real situation and gives the best FEM simulation of hydride precipitation up to now. The hydride shapes predicted by Metzger's model have been observed experimentally [51].

Stress Redistribution due to Hydrogen Diffusion

Hydrogen diffusion also results in a redistribution of stress, due to the dilation caused by the positive partial molal volume of hydrogen in zirconium, which is given by MacEwen *et al.* [52] as $1.67 \times 10^{-6} \text{ m}^3/\text{mol}$ and Eadie *et al.* [53] as $1.7 \times 10^{-6} \text{ m}^3/\text{mol}$, respectively. When a

stress is applied, hydrogen begins to diffuse to the region with higher hydrostatic stress. During this process, a hydrogen concentration gradient is built up in the same direction as the hydrostatic stress gradient, and will impede further diffusion of hydrogen along the stress gradient. At the same time, when the hydrogen concentration increases, the tensile stress at that position will be relaxed due to the volume dilation caused by the positive partial molal volume of hydrogen in zirconium, although this effect is negligible. This is because the hydrogen concentration (only in $\mu\text{g/g}$) is very small, so that the fraction of volume change (usually about 10^{-6}) caused by the hydrogen concentration increase can be neglected compared with the strain (usually in the order of magnitude of about 10^{-3}). When these effects reach an equilibrium, a stable hydrogen concentration profile is built up. The diffusion of hydrogen itself will no longer cause any redistribution of stresses, because the hydrogen concentration now remains unchanged.

1.2.3. Current Theoretical Model for Delayed Hydride Cracking

The current model for DHC is: hydrogen diffuses to crack tip along the hydrostatic stress gradient, and causes an increase of hydrogen concentration near the crack tip. If the hydrogen concentration exceeds the precipitation solvus at that temperature, hydride will precipitate and grow. The region in which the hydride precipitates becomes a mixture of hydrides and matrix ligaments, and the fracture toughness of this region is lowered. When this region grows to a certain size, a critical condition is reached, and the crack will propagate.

Then the crack tip moves to a new location, where new hydride precipitates will form. Hence the cracking proceeds in a step-wise manner.

1.2.3.1. Hydrogen Diffusion

By the general expression of diffusion as given in equation (1.4), we have

$$J = -\frac{DC}{RT} \frac{d}{dx} [RT \ln C - p\bar{V}_H], \quad (1.12)$$

where

J is the hydrogen flux;

D is the diffusion coefficient of hydrogen in the metal;

R is the gas constant;

T is the temperature in Kelvin;

C is the hydrogen concentration at any point x ;

\bar{V}_H is the partial molal volume of hydrogen in the metal;

p is the hydrostatic stress (negative if compressive).

One can see that, if the derivative of chemical potential of hydrogen $d(RT \ln C - p\bar{V}_H)/dx$ is not zero, hydrogen diffusion will occur.

1.2.3.2. Hydride Formation

The driving force for hydride formation is the difference in Gibbs free energy of the zirconium matrix saturated with hydrogen and the zirconium hydride. When the precipitation solvus is reached, this difference in Gibbs free energy is large enough to overcome the elastic and plastic deformation energy associated with the hydride formation, so that precipitation will occur.

By the chemical potential expression of $(RT \ln C - p \bar{V}_H)$ and by $p = 2.4\sigma_{ys}$ based on Dutton *et al.*'s analysis [40], we have:

$$\frac{C}{C_o} = \exp\left(\frac{p \bar{V}_H}{RT}\right) = \exp\left(\frac{2.4\sigma_{ys} \bar{V}_H}{RT}\right), \quad (1.13)$$

which gives the maximum ratio of the hydrogen concentration near the crack tip over the average hydrogen concentration in the specimen as affected by the hydrostatic stress gradient. In equation (1.13), it is assumed that the hydrostatic stress at the hydrogen source is negligible compared to that at the crack tip. For Zr-2.5wt% Nb alloy, σ_{ys} is about 484 MPa at 300°C [54], which gives a ratio C/C_o of about 1.5. From the expressions of the precipitation solvus and dissolution solvus of hydrogen in zirconium, as given in equations (1.2) and (1.3), the ratio of C_H^p/C_H^d varies from 1.68 at 400°C to 2.59 at 200°C, which means that in the temperature range of 200-400°C, the hydrostatic stress will not be able to raise the hydrogen concentration from C_H^d to C_H^p . This is the reason why we need to first raise the temperature to a certain level (usually referred to as the peak temperature) higher than the test temperature, and then cool to

the test temperature so as to get a supersaturation of $C_H^{dt} > C_H^d$, the prime here denoting the dissolution solvus for the peak temperature. Hydride can form if $C_H^p/C_H^{dt} < 1.5$, which means the supersaturation of hydrogen concentration is high enough to be raised to the C_H^p by the hydrostatic stress. By this method, one can calculate the peak temperature one must reach for a certain test temperature, in order to get hydride precipitation.

1.2.3.3. Hydride Cracking

Several models have been proposed for the critical conditions of hydride cracking. They are namely the critical stress model [55], the energy balance model [56], and the combined critical stress and strain model [57].

Shi *et al.* [55] proposed the criterion for hydride fracture at a given K_I to be:

$$\sigma_{eff}^u + \sigma^h = \sigma_f^h, \quad (1.14)$$

where $\sigma_{eff}^u = \sigma_{\perp}$, which is the stress perpendicular to the crack plane, σ^h is the stress normal to the crack plane created only by the hydride formation due to the volume dilation (usually compressive), and σ_f^h is the critical stress required for hydride fracture, which is assumed to have a definitive value and is a material property of the hydride. They considered a sharp crack tip with a total crack length of $2a$ in an infinitely large and elastically isotropic plate. The K_I was calculated by [58]:

$$K_I = \frac{2a}{\sqrt{\pi a}} \int_0^a \frac{\sigma(x) dx}{\sqrt{a^2 - x^2}}, \quad (1.15)$$

where $\sigma(x)$ is the stress distribution along the half-crack length a . And by assuming a flat, ellipsoidally-shaped hydride precipitate and using Eshelby's method [37], they determined the stress σ^h created by hydride formation to be:

$$\sigma^h = -\alpha \frac{E \varepsilon_{\perp} t}{1 - \nu^2 L}, \quad (1.16)$$

where α is the proportionality coefficient, ε_{\perp} is the strain perpendicular to the cracking plane generated by the hydride inclusion, t and L are the thickness and diameter of the hydride disk, respectively. For $t < L$ (disc-shape inclusion), $\alpha = \pi/4$; and for $t = L$ (spherical inclusion), $\alpha = 8/15$. They concluded that, for a single-hydride platelet when $2\delta > 0.25t$, δ being the crack opening displacement (COD),

$$(K_{IH})^2 = \frac{E^2 \varepsilon_{\perp} t}{8\pi(1 - \nu^2)^2 \left(\frac{1}{1 - 2\nu} - \frac{\sigma_f^h}{\sigma_{ys}} \right)}, \quad (1.17)$$

where they assumed that the critical stress required to fracture the hydride is related to its Young's modulus: $\sigma_f^h = 7.357 \times 10^{-3} E_h$, E_h being the Young's modulus of hydride. Equation (1.17) is a function of temperature, since the yield stress σ_{ys} varies with temperature. It predicts a correct trend of K_{IH} vs. temperature, but a lower K_{IH} value when compared with the experimentally measured K_{IH} . It is believed that this discrepancy is due to the over-simplified one-hydride-platelet model used in their analysis.

Smith [57], however, argued that if equation (1.17) is correct, K_{IH} should be equal to zero if hydride precipitation were not associated with a strain ε_{\perp} , which is clearly not true because fracture must be associated with a non-zero K_I . Smith believed that it is over-simplistic to assume a tensile stress σ_h^f to be the criterion for hydride fracture, and some plastic strain must also be involved in the failure of the hydride region. Therefore, Smith proposed an expression for the K_{IH} to be:

$$K_{IH} = \sqrt{Ep^*V^*}, \quad (1.18)$$

where E is the Young's modulus of zirconium matrix, p^* is the tensile stress required either to fracture hydride platelets or to rupture the zirconium matrix ligaments between the fractured hydride platelets, whichever is larger, and V^* is the displacement between the two cracking surfaces required to rupture the ductile zirconium matrix ligaments between the hydride platelets. In the above expression, it is assumed that the stress within the fracture process zone is uniform, with a value of p^* , which can be further refined as $p^* = (1-f)q\sigma_{ys}$, σ_{ys} being the yield stress of the zirconium matrix, f being the fraction of area occupied by fractured hydride platelets and q being a plastic constraint factor, with a maximum value of about 3 [59]. In Smith's expression of K_{IH} , the displacement V^* and the fraction f are taken in an average sense, which contain scattering that may account for the variability in the experimentally measured K_{IH} . Smith also suggested that the hydride platelet should extend from the peak hydrostatic region which is a little away from the crack tip, rather than immediately extend from the crack tip as assumed in Shi *et al.*'s [55] model. But by Ellyin *et al.*'s numerical analysis [50], the

initial position of hydride precipitation has little effect on the development of stress distribution at the crack tip.

Zheng *et al.* [56] proposed a fracture criterion based on an energy balance. In this criterion, instead of a critical stress, the general elasto-plastic energy release rate over a finite crack extension is considered as the driving force for cracking. This energy release rate is defined as:

$$G_{finite} = \frac{\Delta W - \Delta U}{\Delta A} = \frac{\Delta W - \Delta U^e - \Delta U^p}{\Delta A}, \quad (1.19)$$

where ΔW is the mechanical work done by the external load during the finite crack extension, ΔU is the change in total energy which includes both elastic and plastic energy terms (ΔU^e and ΔU^p , respectively), and ΔA is the surface area formed during the crack extension. This criterion predicts a crack extension when

$$G_{finite} = G_c, \quad (1.20)$$

where G_c is the energy required to create the fracture surface, which reflects the combined effect of both hydrides and zirconium matrices. In [56], it is assumed that the length of crack extension equals the hydride length. Since G_{finite} is proportional to the crack extension length, Zheng *et al.*'s fracture criterion successfully explains the phenomenon that the hydride needs to grow to a certain length to fracture. In their study, G_{finite} is calculated numerically by using a finite element program assuming elasto-perfectly-plastic material behaviour, and the value of G_c is obtained experimentally by using the relation,

$$G_c = f_a G_h + (1 - f_a) G_m + R G_s, \quad (1.21)$$

where f_a is the area fraction of hydride on the fracture surface, G_h the energy required to create the fracture surface in the hydride, G_m and G_s the energy required to create the fracture surface in the matrix by tensile and shearing stress respectively, and R the surface roughness related to shearing. They obtained the values of f_a and R by examining the fracture surface, and based on the available G_h , G_m and G_s data [60], they found that G_{finite} and G_c agree with each other very well.

1.3. INFLUENCING FACTORS ON THE DHC BEHAVIOUR OF Zr-2.5wt% Nb ALLOY

1.3.1. Effect of Microstructures

Simpson and Cann [61] studied the effect of heat-treatment on the DHC velocity of Zr-2.5wt% Nb alloy, and found that microstructures had a strong effect, by a factor of five, on the DHC velocity. Zr-2.5wt% Nb pressure tube material in the as-manufactured condition consists of α -zirconium grains with a continuous β -zirconium at the grain boundaries, as shown in figure 1.20. According to Sawatzky *et al.* [62], the diffusion coefficient of hydrogen in β -zirconium is nearly two orders of magnitude higher than that in α -zirconium. Therefore, the short-circuiting diffusion through the β -phase in the as-manufactured Zr-2.5wt% Nb will enhance the hydrogen diffusion in the alloy. In as-manufactured Zr-2.5wt% Nb heat-treated for 10 days at 400°C, the β -phase decomposed and became discontinuous, so that the short-circuiting diffusion no longer existed. Since DHC is a diffusion-controlled process, the cracking velocity largely depends on the hydrogen diffusion rate. Therefore the DHC velocity in the as-manufactured alloy would be higher than that in the heat-treated one.

Coleman *et al.* [63] studied the effect of different heat-treatment times on the DHC velocity of 20% cold-worked Zr-2.5wt% Nb alloy, and obtained similar results. According to

their work, heat-treatment will decrease the DHC velocity. The longer the annealing time the smaller the DHC velocity became. The K_{DH} , however, seemed to be unaffected by the heat treatment, according to their studies.

The average activation energy of hydrogen diffusion in the zirconium alloy is reflected in the slope of the $\ln(\text{DHC velocity})$ vs. $1/T$ curve, T being the temperature in Kelvin. There has been quite a large discrepancy in the measured frequency factor and activation energy of hydrogen diffusion in zirconium alloy with different microstructures, as reported by Skinner *et al.* [64]. This may be due to the subtle differences between the nominally same microstructures of zirconium alloys reported in different papers.

1.3.2. Effect of Texture

Because of the anisotropy of hexagonal α -zirconium, a texture is formed upon plastic deformation during the fabrication process, which will affect hydride precipitation. Cheadle *et al.* [65] pointed out that hydride reorientation will become easier if α -grains are equiaxed and if their basal plane normals are parallel to the tensile stress. In this situation, the reoriented hydride platelets will be parallel to the basal plane of α -zirconium. Since the effective hydride platelets during the DHC process are those reoriented ones, the relative orientation between the basal plane of α -zirconium and the cracking plane will be an important factor in DHC initiation and propagation. Therefore, Coleman *et al.* [63] proposed that if the crystallographic

texture can be arranged so that the basal plane normals of α -grains are nearly perpendicular to the major tensile stress, DHC can be diminished.

The pressure tube Zr-2.5wt% Nb alloy has been plastically deformed in the radial direction, as a result about 60% of the basal plane normals are in the circumferential direction and most of the rest in the radial direction. Consequently, cracking is relatively easier in a plane perpendicular to the circumferential direction and is very difficult in a plane with the normal in the axial direction. Therefore, DHC always happens, or is made to happen, along the axial or radial direction, with the cracking plane lying in the axial-radial plane of the pressure tube alloy.

Previous heat-treatment, such as α -treatment and/or β -treatment, *i.e.* holding at a temperature in α -region or β -region, the nature of cold-work or hot-work, or hot-work temperature can greatly alter the texture in zirconium alloys. A good summary about the work done on this issue was given by Douglass [4].

1.3.3. Effect of Temperature

1.3.3.1. Direction of Approach to Temperature (T_{DAT})

Ambler [66] proposed the concept of T_{DAT} , the critical temperature above which the direction of approach to test temperature will make a significant difference in the DHC behaviour. Ambler *et al.* [67] showed that, for the DHC incubation time, *i.e.* the time required

to initiate cracking, there was a $T_{\text{DAT}} = 150^{\circ}\text{C}$. The trend of change of incubation time with respect to test temperature started to differ, when the test temperature was higher than T_{DAT} , for the situations as to whether the test temperature was approached by cooling or heating.

Ambler's experiments [66] showed that $T_{\text{DAT}} = 150^{\circ}\text{C}$ also applied to DHC velocity. According to Ambler's experiments, specimens cooled to the test temperature showed an Arrhenius relationship between the cracking velocity and the test temperature, while specimens heated to the test temperature first showed the same DHC velocity vs. temperature relationship as the cooled specimens, up to T_{DAT} , above which the cracking velocity decreased with a further increase of temperature.

Puls [68] and Simpson *et al.* [69] developed a DHC model in which the elastic constraint of hydrides played an important role in hydrogen diffusion to the crack tip. They postulated that the T_{DAT} phenomenon was related to the difference in the degree of elastic constraint in the hydrides formed upon cooling and upon heating. Based on the assumption that each step of crack growth required the nucleation of a new hydride at the crack tip, and this hydride was initially fully constrained, Ambler [66] developed an analytical model which, by adjusting the elastic constraint energy of hydride w_t^{inc} , gave a prediction of DHC velocity which was in fairly good agreement with the experimental results.

1.3.3.2. Crack Arrest Temperature (T_{CAT})

Smith and Eadie [70] proposed a new concept of temperature limit for DHC, referred to as T_{CAT} . T_{CAT} is defined as the temperature above which DHC can not be initiated, even if the mechanism of hydride precipitation still exists.

There is a T_{CAT} in fracture mechanics, in which no DHC mechanism is involved. For a certain stress intensity factor K_I which can initiate cracking at a certain temperature, if there exists a higher temperature above which cracking can no longer propagate, then this temperature is referred to as the T_{CAT} for this K_I . The explanation for this phenomenon is the increase in material toughness at higher temperature, which is usually demonstrated by Charpy impact tests. Conversely, this K_I is very close in meaning to K_{IC} , the critical K_I to initiate a cracking, at the temperature $T = T_{CAT}$.

In DHC, in a similar sense, K_{IH} should also have a one-to-one relationship with T_{CAT} . This is because K_{IH} is the minimum stress intensity factor for the DHC to happen under a certain set of conditions. For example, if one gets $K_{IH} = 6 \text{ MPa}\sqrt{\text{m}}$ at 200°C , then in other words, 200°C is the T_{CAT} for $K_I = 6 \text{ MPa}\sqrt{\text{m}}$. Therefore, one can see that T_{CAT} is a phenomenon which is closely related to the phenomenon of K_{IH} .

However, according to our present experimental procedures, T_{CAT} is defined as the temperature at which, due to some critical relationship between the stress distribution and hydrogen supersaturation at the crack tip, the hydride platelets cannot grow to a size large

enough for fracture. Therefore, in our present experiments, T_{CAT} is a function of peak-temperature, which determines the supersaturation of hydrogen in the specimen at the test temperature.

Further investigation in the first T_{CAT} , i.e. defined by Smith and Eadie [70], will provide us with an insight into the mechanical criterion for fracturing the hydride platelets and the matrix ligaments separated by hydride platelets. And the second T_{CAT} , as defined by our present experimental procedures, may provide us with an understanding of the critical stress distribution required for hydride precipitation and growth, as well as the interaction between hydride precipitation and the stress at the crack tip.

1.3.4. Effect of Thermal History

1.3.4.1. Thermal Ratchetting

Eadie *et al.* [71] first noticed and quantitatively described the effect of thermal cycles on increasing the local hydrogen concentration, which was referred to as ratchetting. By using a FEM code [72], which took into account the hydrogen diffusion and hydride precipitation, they quantitatively studied this effect with different parameters of thermal cycles, such as peak temperature and cooling rate *etc.*. Their results are shown in figure 1.21, where $C_H(tot)$ is

defined as the average hydrogen concentration within each FEM cell, including the hydrogen in the zirconium matrix and the hydrogen in the hydride precipitates.

The essence of thermal ratchetting is the existence of two solvi of hydrogen in zirconium during cooling and heating. During the cooling process, the hydride precipitation brings about a large local segregation of hydrogen (as hydride), which may not completely dissolve during the subsequent heating process if the peak-temperature is not high enough. On the other hand, when the temperature rises, more hydrogen will diffuse into the crack tip region, which will precipitate as hydride during the next cooling process. In this way, every thermal cycle will add some hydride at the crack tip region. This effect will disappear, if the peak-temperature during the heating process is high enough, so that the dissolution solvus of hydrogen at this temperature exceeds the average hydrogen concentration in the specimen, and all hydrides in the specimen then dissolve, when heated to the peak-temperature.

Eadie *et al.* [71] further refined the concept of ratchetting into three categories, in decreasing order of importance: (1) hydride formation ratchetting; (2) cool-down ratchetting; and (3) pure ratchetting. In a recent technical report by Metzger [73], these three kinds of ratchetting were further elucidated, and the parameters required to completely describe a thermal cycle, plus their effect on hydride accumulation were discussed. Metzger [73] further brought up the importance of heat-up process to the hydride accumulation, which had not been fully recognized before.

1.3.4.2. Memory Effect

Cameron *et al.* [74] proposed that there is a memory effect in hydride precipitation in cold-worked Zr-2.5wt% Nb alloy. The memory effect is defined as the strong tendency for the size, distribution, and morphology of hydrides before a thermal cycle to a higher temperature at which the hydrides dissolve, to influence the same factors of the hydrides re-precipitated during cooling.

According to their experiments, in as-received 25% cold-worked Zr-2.5wt% Nb tube material containing about 8 $\mu\text{g/g}$ hydrogen, hydrides usually lie on the axial-circumferential planes. After heating to 225°C and holding for 180 minutes, the hydrides dissolved and re-precipitated in the original orientation. This proved the effect of original hydride orientation on the subsequent re-precipitation. Applying a tensile stress in an appropriate direction to the specimen during the thermal holding and cooling process re-oriented the hydrides on the axial-radial planes. They then showed that refining the hydrides by a heat-treatment at 300°C plus subsequent quenching before the above experiment could diminish the stress-induced re-orientation effect. This proved that the refined hydride morphology, as the original hydride morphology, counterbalanced the effect of tensile stress on hydride re-orientation. They further studied the effect of cooling-rate on the memory effect, and found that fast cooling, *e.g.* quenching, would diminish the memory effect, while under a slow cooling rate, *e.g.* 1°C/min, the memory effect could still be observed.

1.3.5. Effect of Stress Intensity Factor

The effect of stress intensity factor K_I on DHC velocity is illustrated in figure 1.22. The curve is usually divided into three stages. In stage I, where K_I is very close to K_{IH} , the DHC velocity increases rapidly with increasing K_I . The mechanism for this rapid growth of DHC velocity, which is related to K_{IH} phenomena, has not been satisfactorily explained in the literature and will be studied in this work. In stage III, the cracking velocity increases sharply with any small increase of K_I , and the material fails with a mechanism other than DHC. In stage II (the plateau), the DHC velocity almost remains as a constant or increases slightly with K_I . In chapter 4 of this work, the stages I and II behaviour of the DHC velocity vs. K_I curve will be explained from the point of view of a critical hydride cluster length for fracture.

1.3.6. Effect of Hydride Morphology

The detrimental effect of hydrides, especially the re-oriented ones, on the mechanical properties of Zr-2.5wt% Nb alloy has been summarized in section 1.2.1.3.

Wallace *et al.* [75] studied the effect of hydride morphology on the fracture toughness of cold-worked Zr-2.5wt% Nb pressure tube material. They introduced a parameter, referred to as hydride continuity coefficient (HCC), to quantitatively describe the degree the hydrides have oriented in the axial-radial plane of the pressure tube alloy. Their results showed that

increasing the hydrogen concentration and the HCC would reduce the fracture toughness. For material with a hydrogen concentration in the range of 60-80 $\mu\text{g/g}$ and a HCC value of about 0.5, the fracture toughness at low temperature ($< 240^\circ\text{C}$) was very low, and there was a sharp increase of fracture toughness at 240°C . Metallographic studies by SEM showed that, when at low temperature, the re-oriented hydride platelets fractured by cleavage, while the zirconium matrix between the hydride platelets ruptured by microvoid coalescence, and the over-all cracking occurred primarily along the hydride platelets. When the temperature was above 240°C , where the material fractured in a ductile mode with a stable cracking rate, the crack-path was not influenced by the re-oriented hydride platelets, and the fracture surface exhibited a ductile fracture. They explained that the rapid increase of fracture toughness at 240°C was partly because of a loss of triaxial constraint at the crack tip due to the transition to plane-stress conditions at high temperature. But some of their results showed that, when the hydrogen concentration was less than $60 \mu\text{g/g}$ and HCC was less than 0.1, there was no such abrupt change of fracture toughness due to the increase of temperature. Therefore, it was obvious that this phenomenon must have something to do with the amount and the orientation of hydride platelets in the specimen. It was probably because there was a brittle-ductile transition of hydrides at a temperature around 240°C .

Recently, Shek *et al.* [76] proposed that, during the DHC of Zr-2.5wt% Nb alloy, the fracture of hydride platelets was completed in a sudden manner, without any pre-microcracking of hydride platelets before the critical fracture event. This observation was different from that

observed in this work as will be discussed in chapter 4. They also found that the length of hydride platelets was associated with striations, and both hydride length and striation length increased as temperature increased. This observation confirms the postulation that DHC proceeds with the precipitation, growth and fracture of critical size hydride platelets.

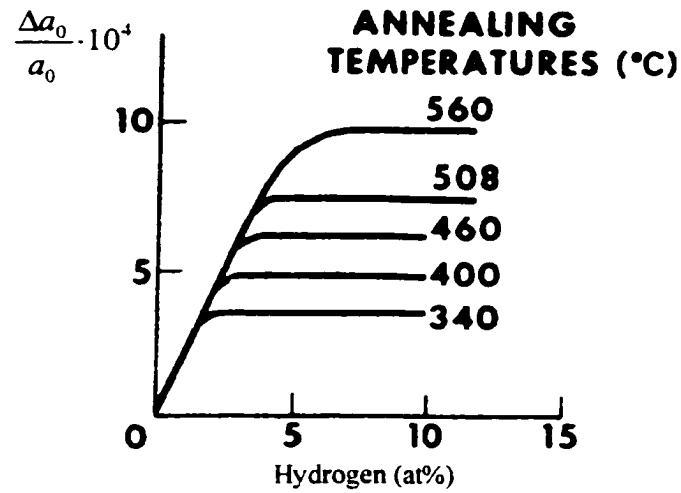


Figure 1.1. Influence of hydrogen on the relative change of lattice parameter a_0 of α -zirconium (Espagno *et al.* [10]).

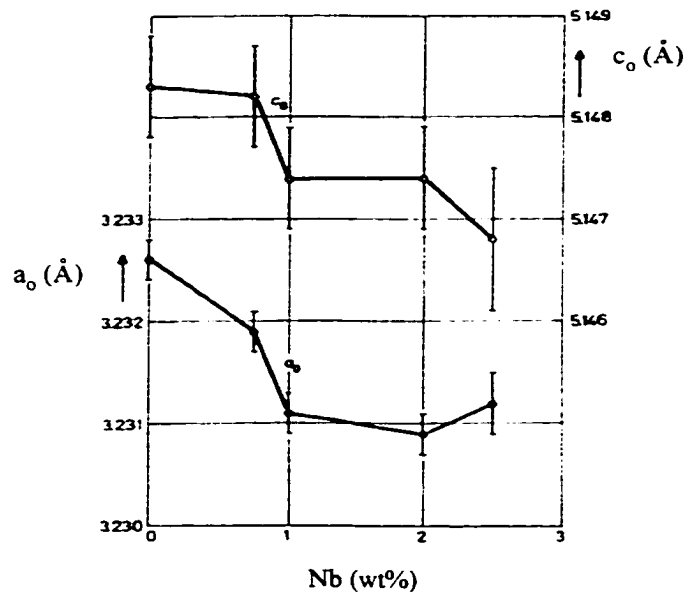


Figure 1.2. Influence of niobium on lattice parameters of α -zirconium (Richter *et al.* [12]).

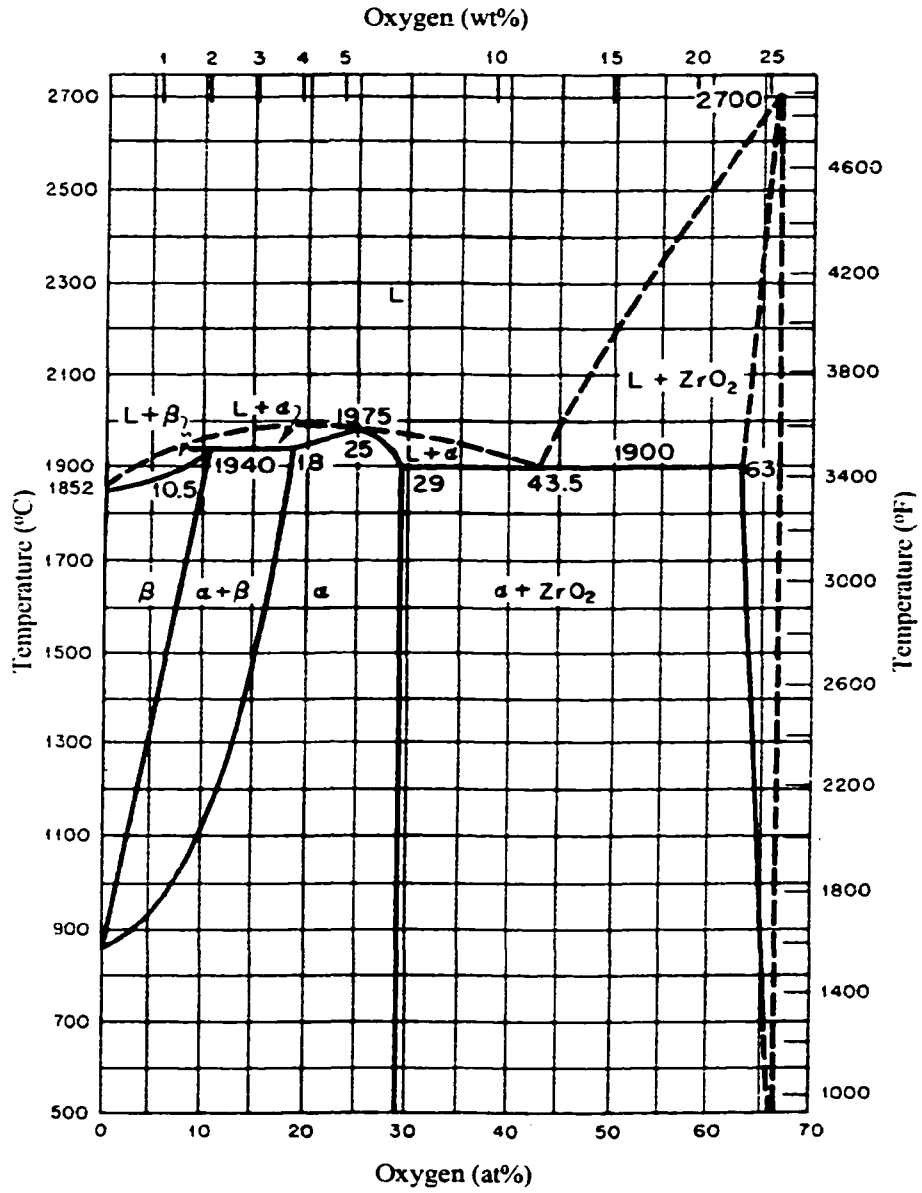


Figure 1.3. The zirconium-oxygen phase diagram (Lustman and Kerze [2]).

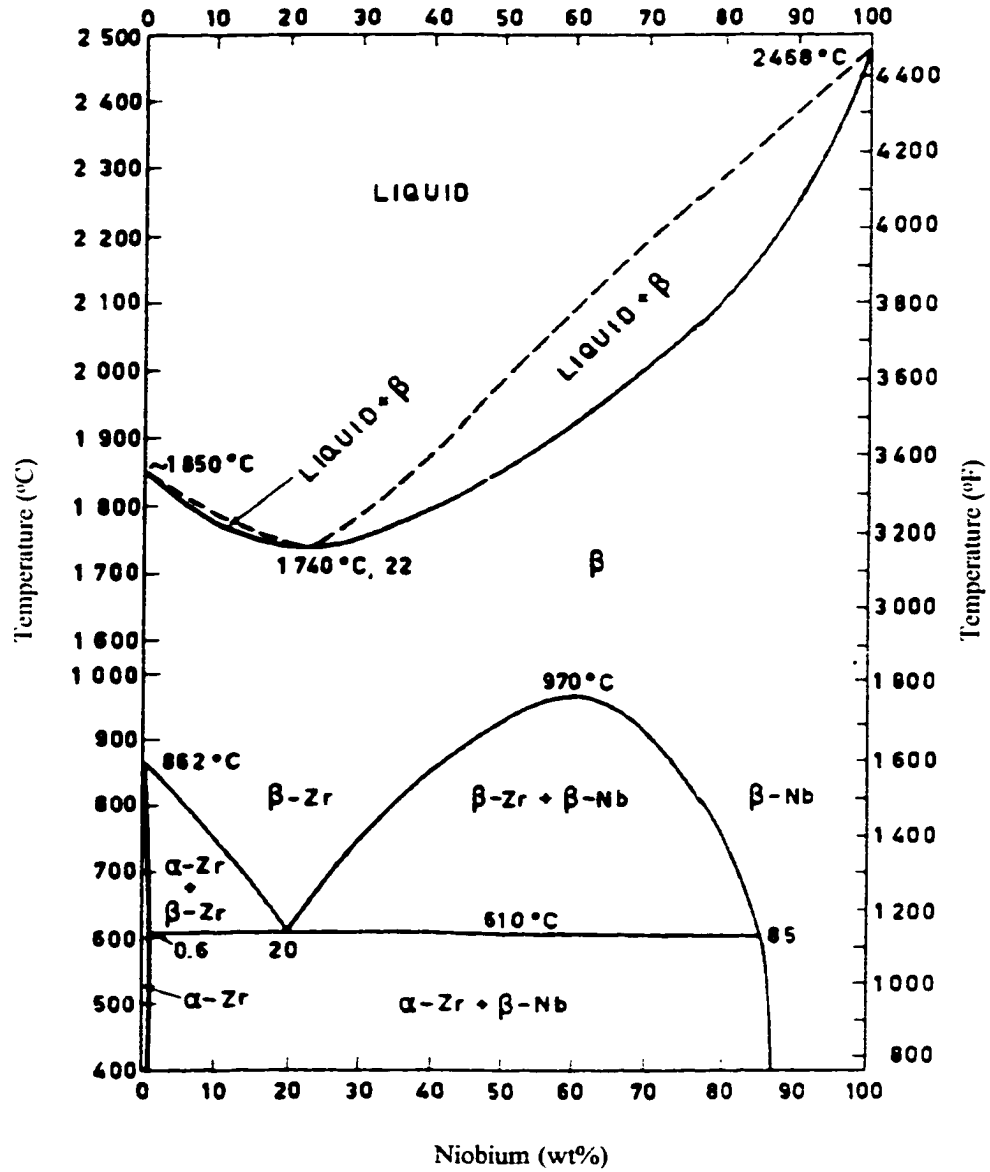


Figure 1.4 (a). The Zr-Nb phase diagram: the complete system (Richter *et al.* [12]).

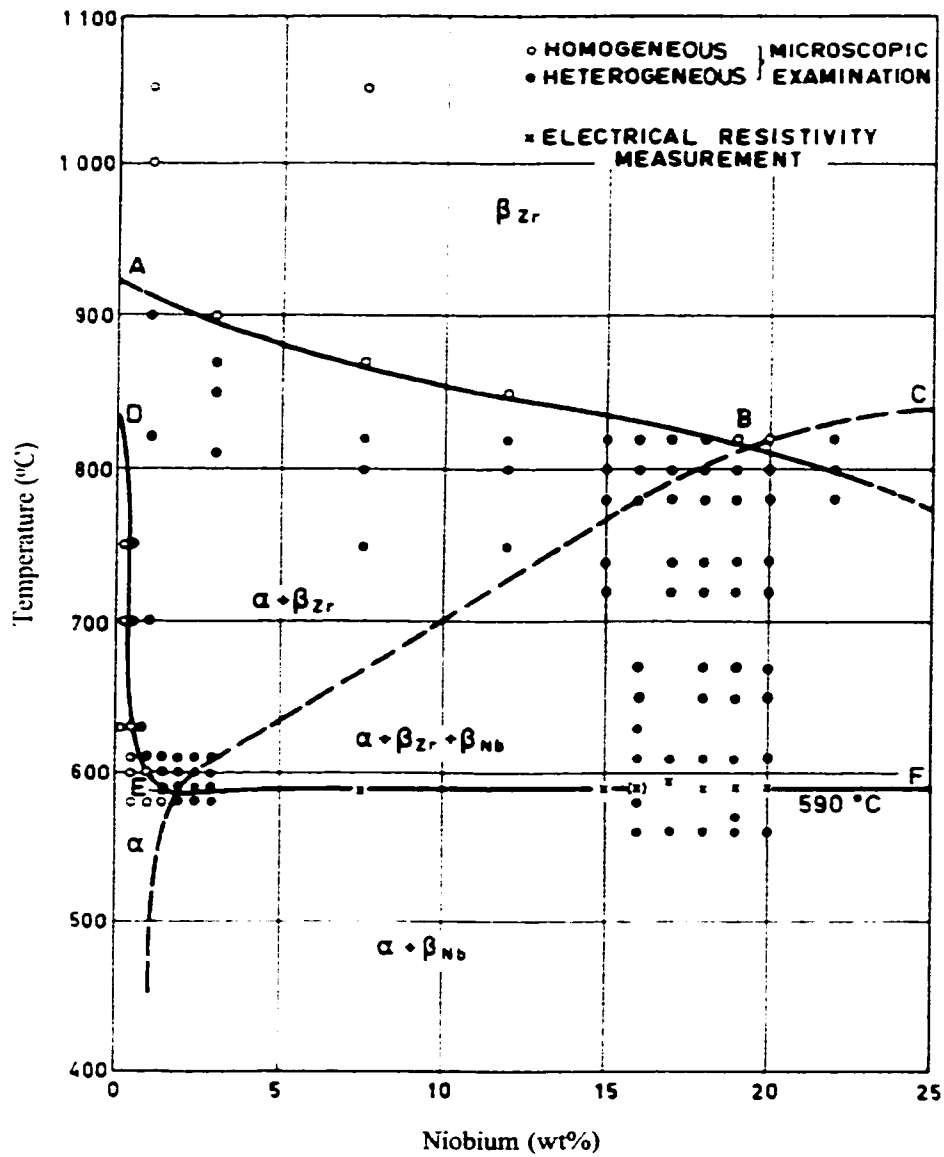


Figure 1.4 (b). The Zr-Nb phase diagram: the Zr-rich portion (Lundin and Cox [13]).

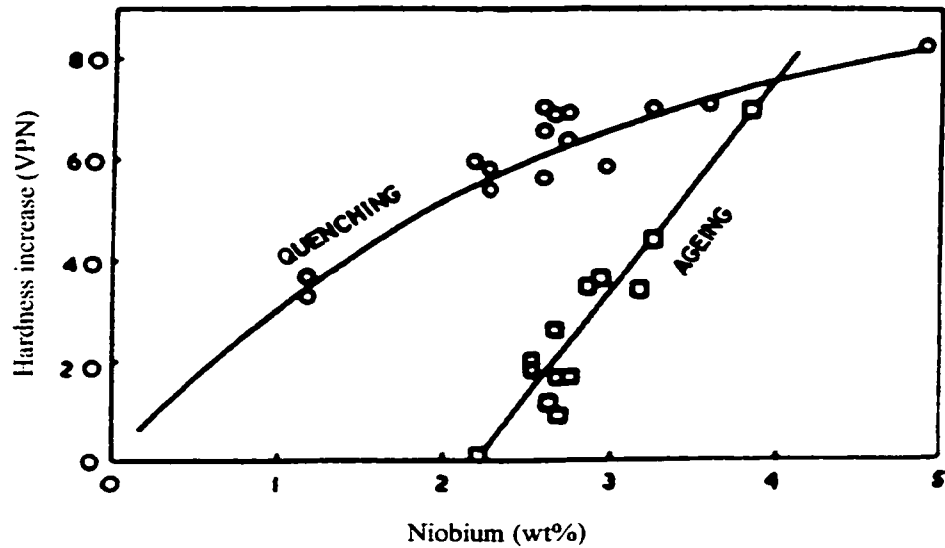


Figure 1.5. The effect of niobium on the hardness increase during quenching and aging (Winton and Murgatroyd [15]).

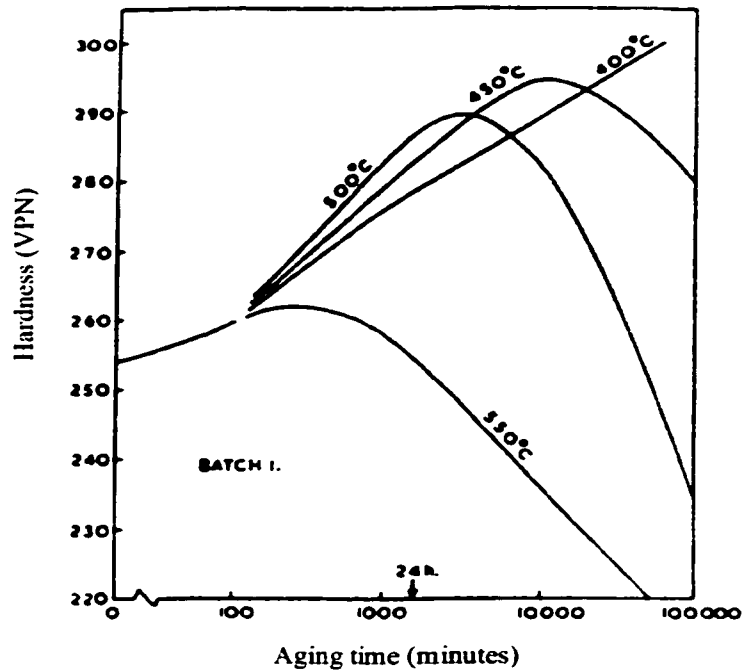


Figure 1.6. The effect of aging on the hardness of Zr-2.6wt% Nb (Winton and Murgatroyd [15]).

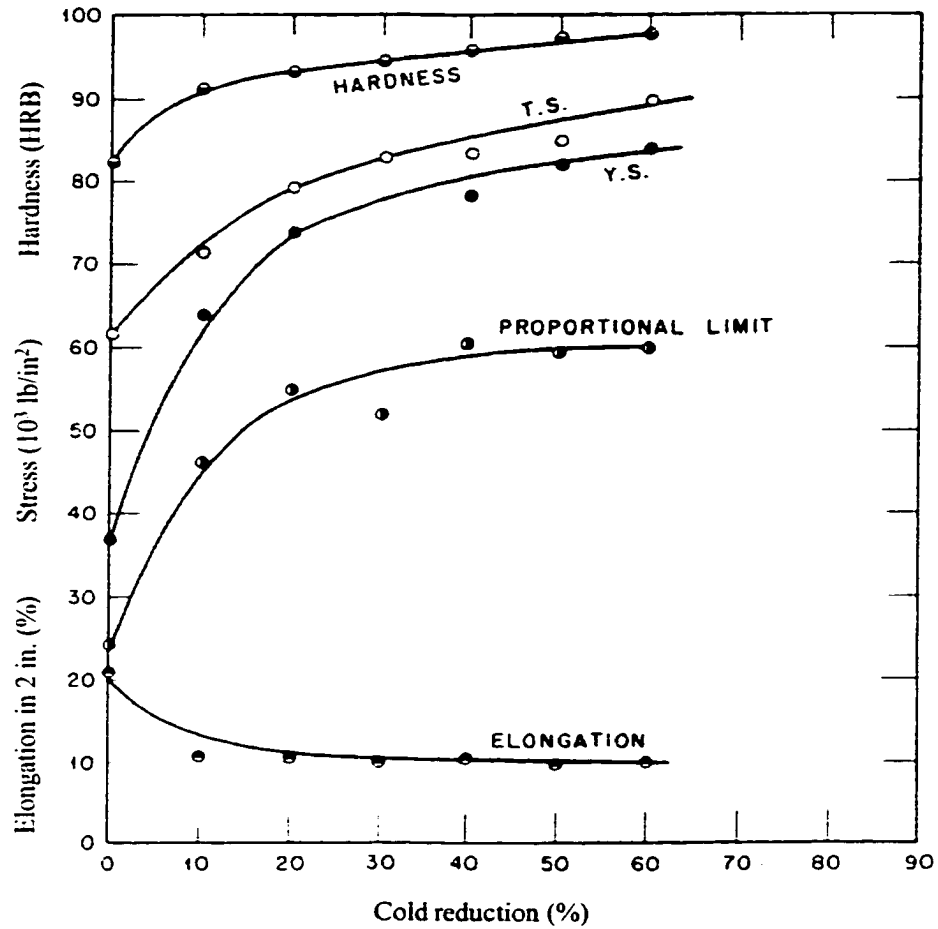


Figure 1.7. The effect of cold work on the tensile properties of induction-melted sponge zirconium (Hayes *et al.* [16]).

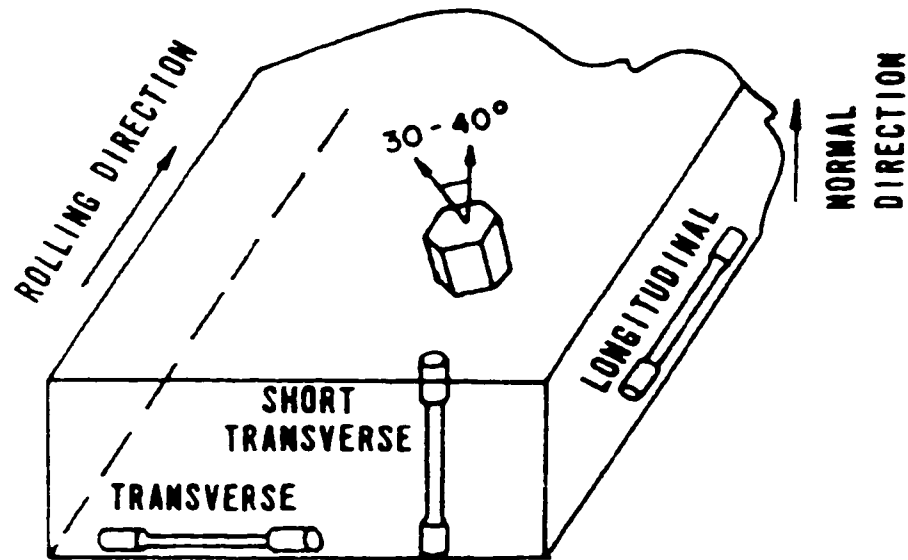


Figure 1.8. The texture in Zr-2.5wt% Nb alloys developed during rolling (Cheadle [17]).

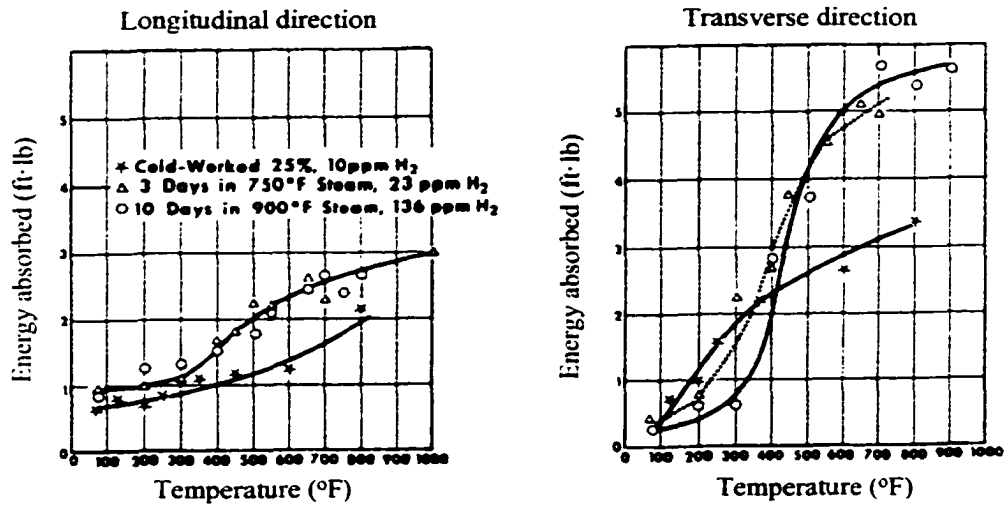
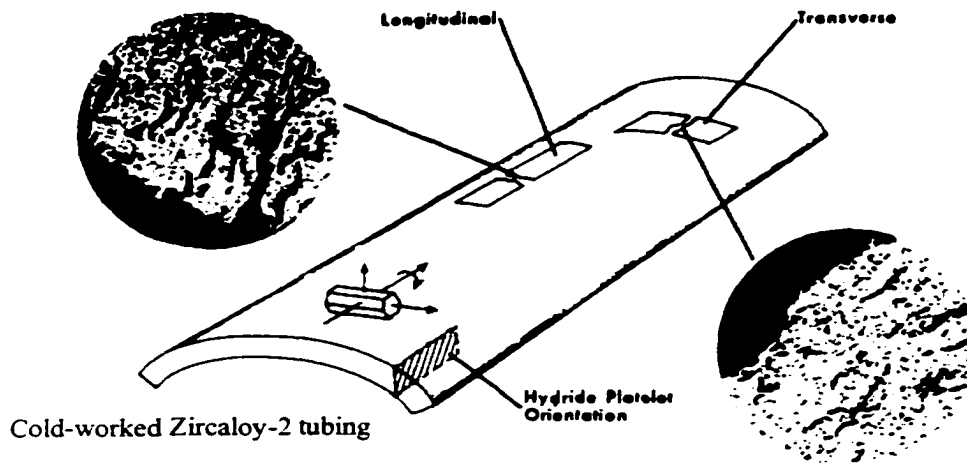


Figure 1.9. The effect of hydride and crystallographic orientation on the impact behaviour of Zircaloy-2 (Douglass [18]).

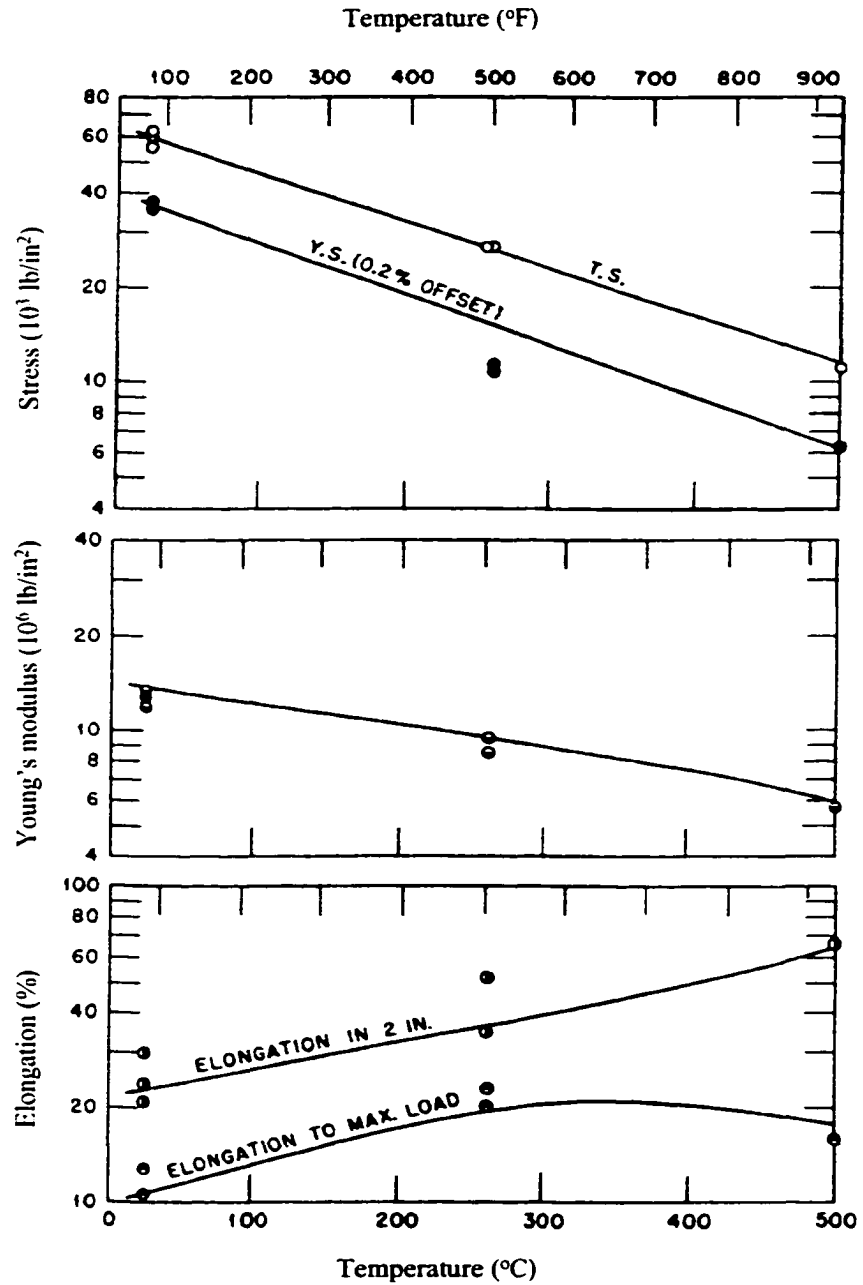


Figure 1.10. The effect of temperature on the tensile properties of induction-melted sponge zirconium (Lustman and Kerze [2]).

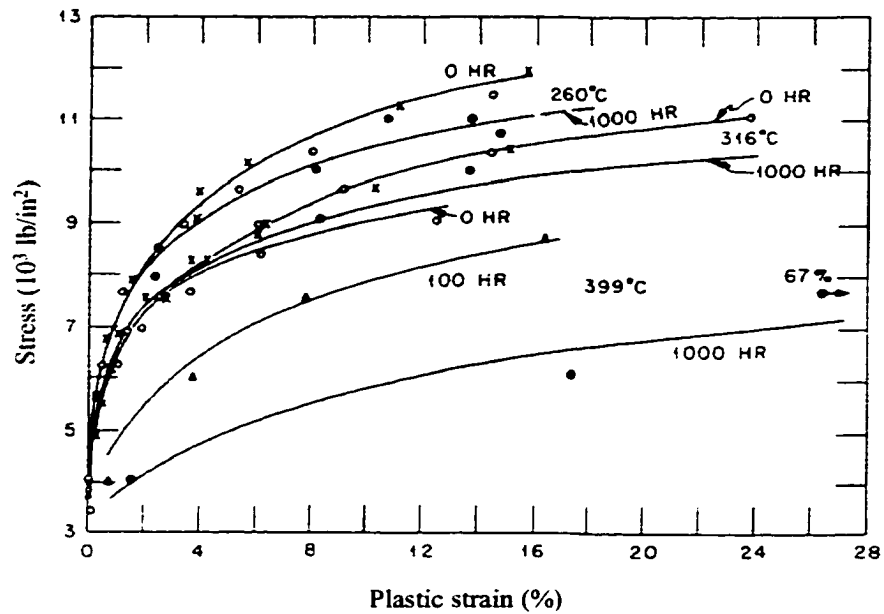


Figure 1.11. The stress-strain curve for short-time and 1000hr loading period at 260, 316, and 399°C (Manjoine and Mudge [22]).

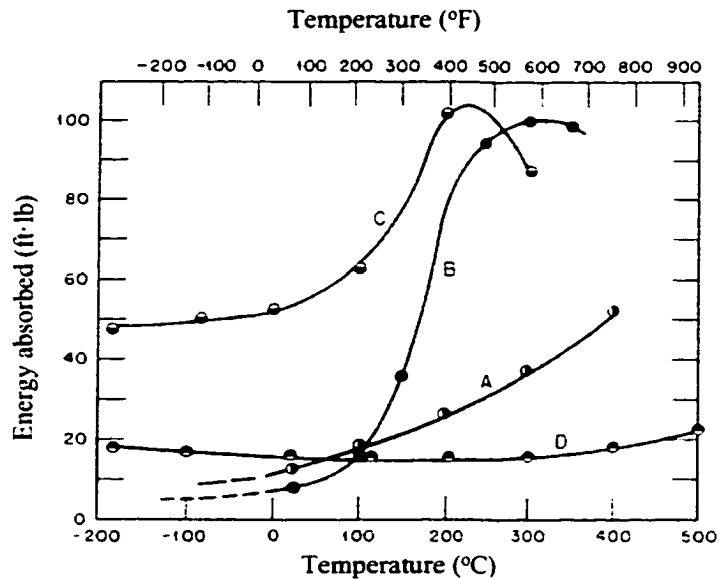


Figure 1.12. The effect of temperature on the impact energy of zirconium (Charpy V-notch specimen). A: induction-melted sponge zirconium; B: arc-melted crystal bar zirconium, $31\mu\text{g/g H}_2$, cooled from 705°C; C: arc-melted crystal bar zirconium, $9\mu\text{g/g H}_2$, cooled from 705°C; D: induction-melted sponge zirconium (Lustman and Kerze [2]).

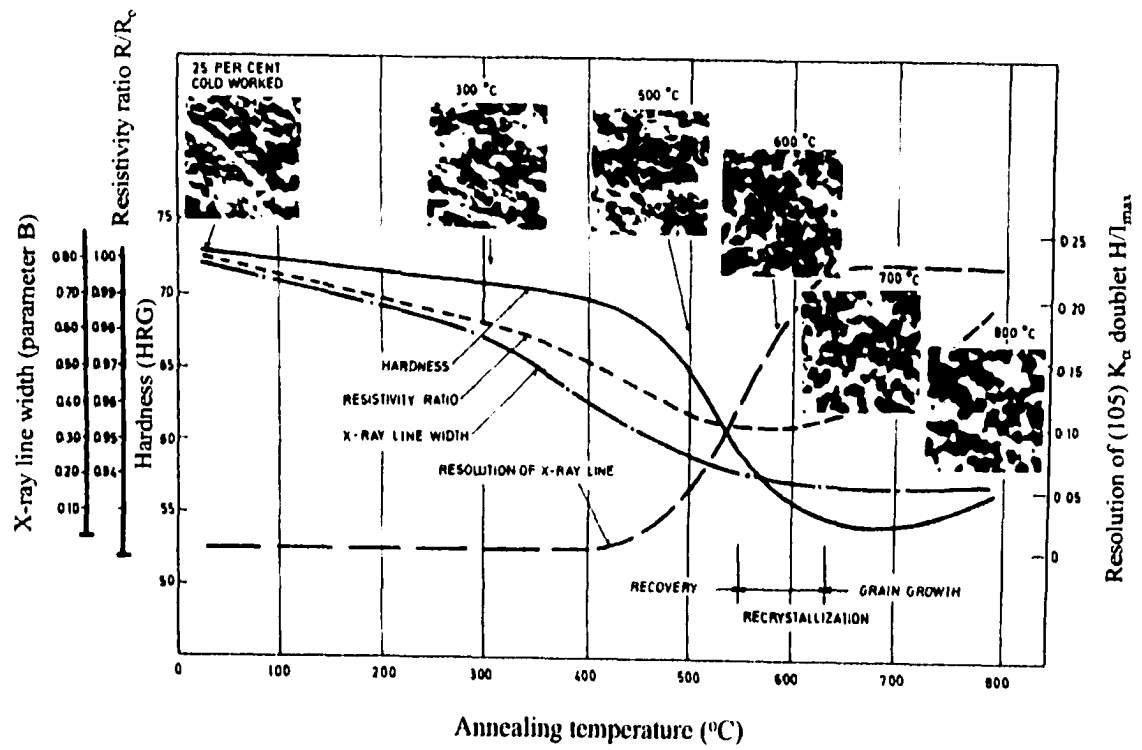


Figure 1.13. The composite of general behaviour during recovery and recrystallization of 25% cold-worked zirconium annealed for 100 minutes at different temperatures (Douglass [4]).

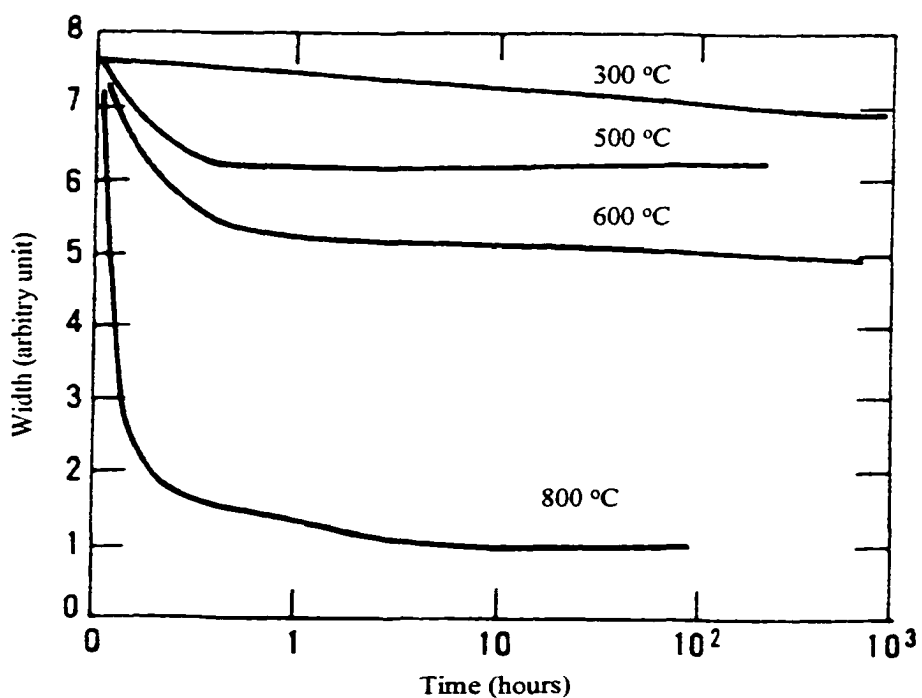


Figure 1.14. The width of the (0004) X-ray diffraction peak of 20% cold-worked Zr-2.5wt% Nb after annealing at different temperatures (Cheadle [23]).

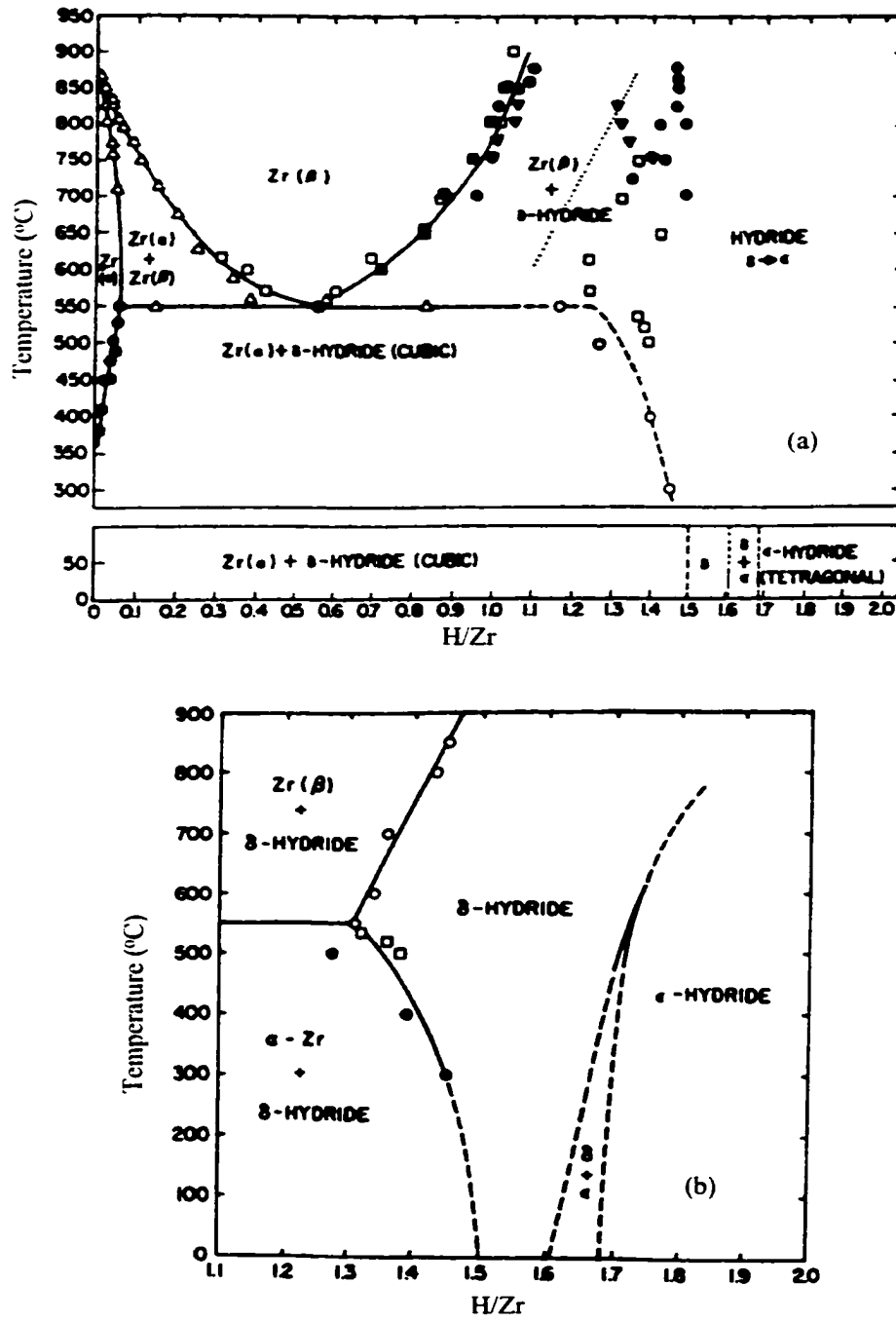


Figure 1.15. (a) The zirconium-hydrogen phase diagram; (b) The high hydrogen content portion of the Zr-H phase diagram (Douglass [4]).

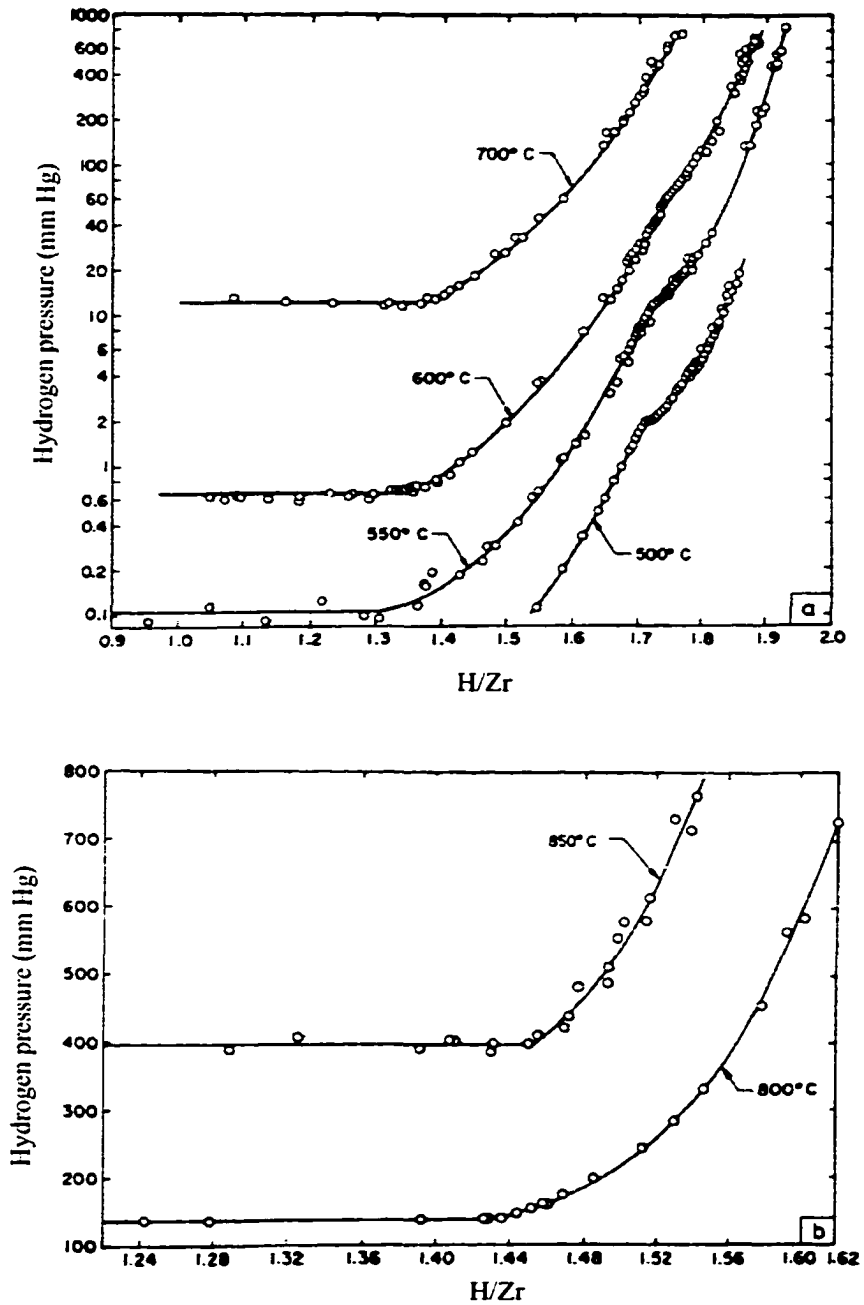


Figure 1.16. Pressure-composition isotherms in the Zr-H system in the temperature range (a) 500-700°C; and (b) 800-850°C (Libowitz [25]).

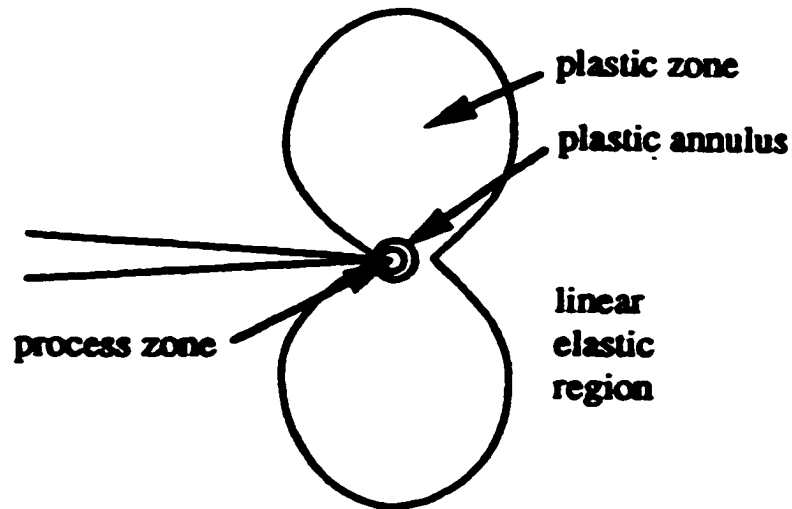


Figure 1.17. The stress zones at the crack tip in plane strain (Eadie *et al.* [32]).

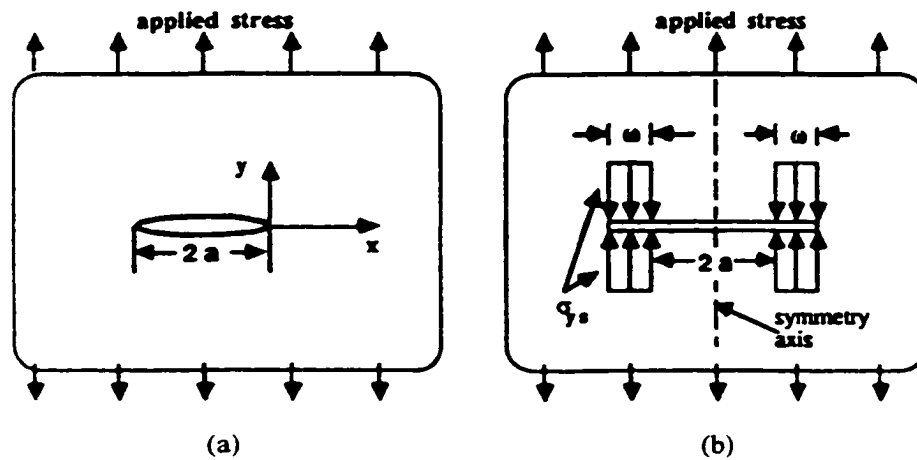


Figure 1.18. The rigid-plastic strip model for finite crack. (a) The crack and the coordinate system; (b) The model with the crack now increased in length by the plastic zones and a compressive stress equal to the yield stress added along the plastic zones of length ω (Eadie and Ellyin [44]).

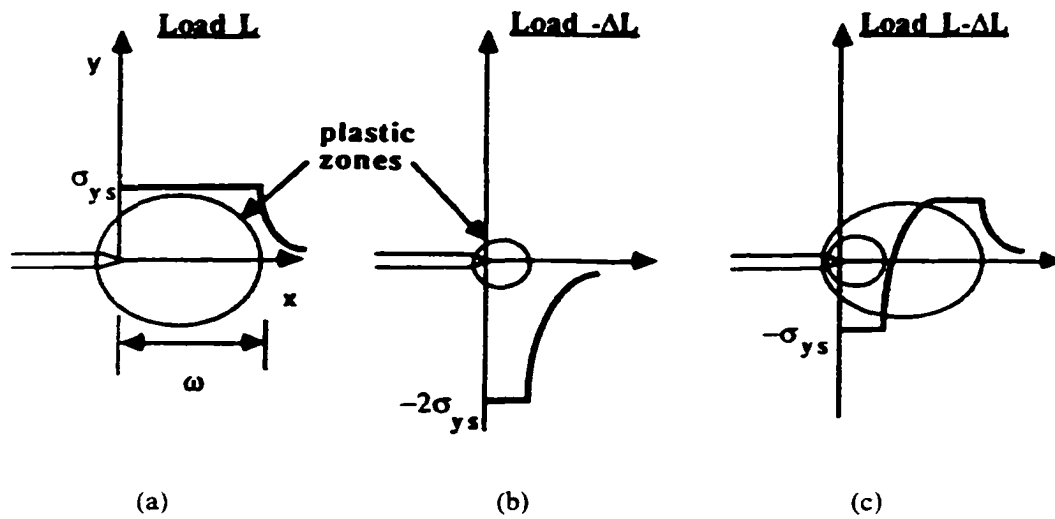


Figure 1.19. (a) Stresses for the applied load L ; (b) Stresses for the reversed load ΔL ; (c) Stresses from superposition (Eadie and Ellyin [44]).



Figure 1.20. A bright-field transmission electron micrograph showing typical grain structure in Zr-2.5wt% Nb pressure tube material. Beta phase separating the alpha grains is denoted by arrows (Simpson and Cann [61]).

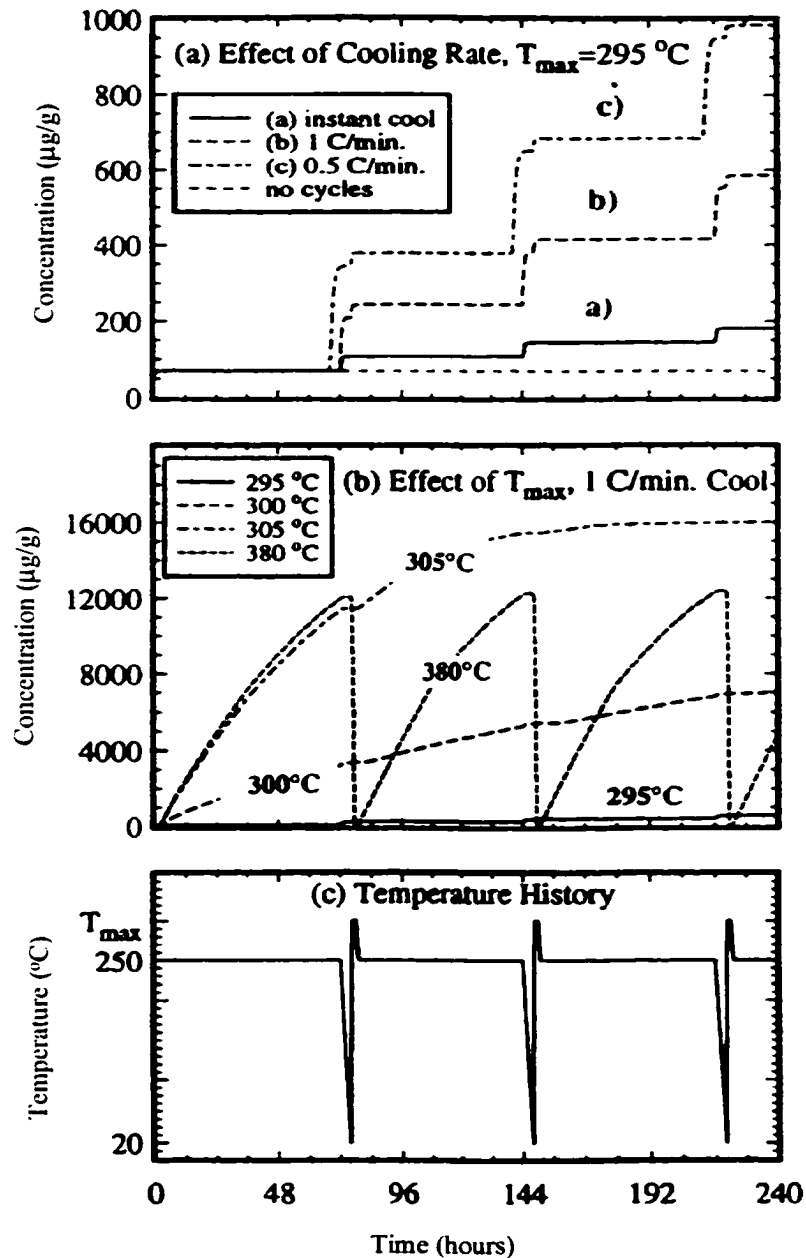


Figure 1.21. The effect of cooling rate and maximum temperature on the total hydrogen level, $C_H(\text{tot})$, at the peak stress location during temperature cycles of a Zr-2.5wt% Nb specimen containing 60 $\mu\text{g/g}$ hydrogen and a notch of depth 0.8 mm and tip radius 0.2 mm under net section stress of 300 Mpa (Eadie *et al.* [71]).

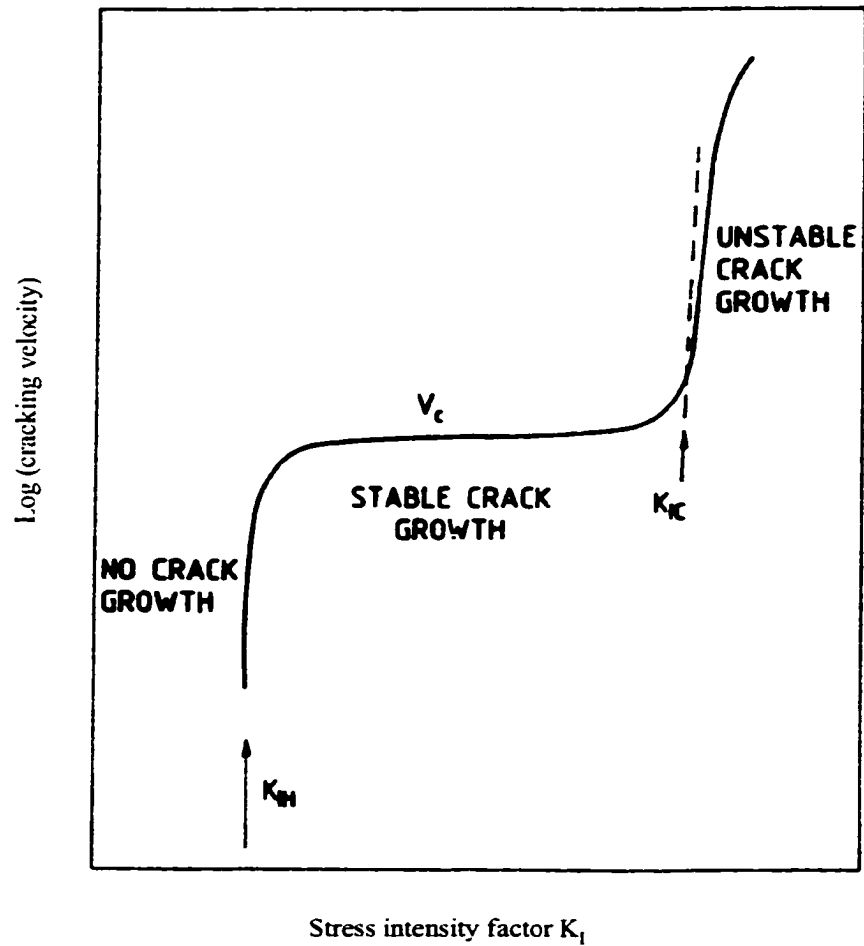


Figure 1.22. Schematic diagram of the dependence of delayed hydride cracking velocity on stress intensity factor (Cheadle [23]).

CHAPTER 2. OBJECTIVES

Because it is not practical to eliminate completely the hydrogen content in the alloy, nor is it possible to eliminate completely flaws in the material, we are unable to eliminate the possibility of DHC. What we can do is to find out the factors that affect the initiation or propagation of DHC, and then try to control and reduce them.

This work concentrates on the critical conditions for DHC initiation, mainly on the effect of stress on hydride precipitation and the mechanism of the threshold stress intensity

factor K_{IH} for DHC. The critical conditions for DHC initiation have been of deep concern to CANDU operators and licensors, who want to know how to diminish this failure mechanism and how long the pressure tubes can last before replacement becomes necessary. A knowledge of the DHC initiation will help us better understand and predict the onset of DHC, and eventually to develop new alloys that are more resistant to this fracture mechanism.

This work focuses on these two aspects of the DHC initiation:

(1) The effect of stress on the precipitation solvus of hydrogen in zirconium.

This part of the work attempts to understand hydride precipitation from the point of view of thermodynamics, and to find a proper material equilibrium criterion for studying the effect of stress on the hydrogen precipitation solvus in zirconium. There has been previous work on this issue [77, 78]. In this work, by following the internal energy minimization method used in Gibbs' original work and other studies [79-82], a more rigorously developed expression will be proposed.

(2) The mechanism of the threshold stress intensity factor K_{IH} for DHC.

K_{IH} is an important parameter in DHC because it defines the stress levels for an assumed or measured pressure tube flaw size at which the pressure tubes may be operated without concern for leakage for their life time [43]. However, as will be elaborated in chapter 4, the definition and determination of the K_{IH} parameter are still not uniquely defined, and the micromechanism of K_{IH} is not well understood [55-56, 83]. This part of the work aims at a better understanding of K_{IH} in these two aspects.

CHAPTER 3. THE EFFECT OF STRESS ON THE HYDRIDE PRECIPITATION SOLVUS IN ZIRCONIUM**ABSTRACT**

This work attempts to find a proper material equilibrium criterion for studying the effect of stress on the precipitation solvus of hydrogen in zirconium. The internal energy minimization method used in Gibbs' original work and other studies on isolated thermodynamic systems is followed, and is extended to studying the material equilibrium of a closed thermodynamic system, which is the present case. For the closed system specified, the material equilibrium condition is found to have an alternative expression, which is more suitable for studying the effect of stress on the hydride precipitation solvus in zirconium. Applying this condition as the material equilibrium criterion, a general expression for the effect of stress on the hydride precipitation solvus is obtained for a simplified model with coherent elastic precipitates.

3.1. INTRODUCTION

Delayed hydride cracking (DHC) in zirconium nuclear reactor pressure tube alloys has been of research interest for the last few decades. It is generally accepted as a process that involves stress induced hydrogen diffusion, hydride precipitation and hydride fracturing [40, 84]. This work attempts to understand the hydride precipitation process under stress from the view point of thermodynamics, and to find out how stress might affect the hydrogen solubilities.

It has long been known that elastic stress may influence phase equilibria [85], and the relationship between the hydrogen solubilities in zirconium alloys and those influencing factors, such as stress and strain energy terms, have been the issue of some recent work [77, 78]. In his pioneering work, Puls established an expression for the hydride precipitation solvus in a fully constrained solid [77]. But, it seems that the effect of external stress, especially for the case when there exists mechanical work done by the external stress, was not fully discussed in Puls' papers. Therefore, it might be worthwhile for us to extend some discussion on this issue, since an accurate knowledge of how the stress and strain energy affect the hydride precipitation solvus is essential both theoretically and practically, and will aid in the establishment of a theoretical model of DHC initiation.

In correlating these factors, it is first necessary to establish criteria for material equilibria under stress. The thermodynamic equilibrium conditions under stress were

discussed in the original work of Gibbs [79], and have since been discussed and established for various kinds of solids in a series of papers by Larché and Cahn [80-82]. In these works, the relationship between the chemical potential of independently variable components in different phases under stress and at equilibrium is established.

Our case, however, might be a little different. Firstly, the thermodynamic system we use to study the hydride precipitation process in stressed zirconium is considered as a closed one, rather than an isolated system as those considered in [79-81]. This is appropriate since during the hydride precipitation, the system (which consists of matrix and precipitate) does not have mass exchange but may have energy exchange (heat or mechanical work) with its surroundings. In this work, a closed thermodynamic system is defined as: a thermodynamic system that has no mass transfer with its surroundings; and an isolated thermodynamic system is defined as: a thermodynamic system that does not interact in any way with its surroundings. These definitions are consistent with those of most authors [86]. Although we may later find the material equilibrium condition for the closed system is identical to that of an isolated one, for the sake of being rigorous, we followed the method used in [79-81], which minimizes the internal energy of an isolated system while keeping the total entropy constant, and studied the material equilibrium condition of a closed thermodynamic system consisting of coherent solid phases with interstitial solutes.

Secondly, the material equilibrium condition expressed as chemical potential uniformity (for interstitial solutes), when applied to our case of hydride precipitation, does not directly reflect how the stress affects the hydrogen solubility. To overcome this difficulty,

some previous work on this issue [77, 78] invoked the Moutier theorem [87]. By going through a Moutier cycle and incorporating the material equilibrium condition as well, an expression for the effect of external stress on the hydride precipitation solvus was obtained [77]. In this work, based on the material equilibrium study of a closed thermodynamic system, we find that, for the closed system corresponding to a simplified hydride precipitation model, the material equilibrium condition has an alternative expression, $dG = \delta W$, which is more suitable for studying our issue of hydrogen solubility. Here dG is the total change in Gibbs free energy of the system, δW being the total mechanical work done on the system by external stress. This expression is generally a necessary condition of material equilibria for closed thermodynamic systems, but for the equilibrium of one interstitial solute in two coherent phases (that is what we assumed in our simplified model of hydride precipitation in zirconium), as one will later see in section 3.2 of this work, it has a unique property of being both necessary and sufficient. Besides, this expression directly relates the Gibbs free energy of the system to the mechanical work done on the system by the external stress, and therefore is ideal for studying the effect of the external stress. Applying this condition as a material equilibrium criterion to the case of hydride precipitation, we can obtain the effect of stress on hydrogen solubility without going through a Moutier cycle (the purpose of going through this cycle was to relate the chemical potential of hydrogen to the external stress), and a general expression is obtained for the simplified precipitation model.

In summary, the discussion on material equilibrium is extended in two aspects in this work: (1) The internal energy minimization method used in [79-81] for studying the

thermodynamic equilibria of isolated thermodynamic systems, is applied to studying the material equilibrium of a closed thermodynamic system. It is found that the material equilibrium condition of the closed thermodynamic system is identical to that of an isolated one. (2) Based on the study in (1), it is found that, for the closed thermodynamic system corresponding to a simplified hydride precipitation model, the material equilibrium condition has an alternative expression, which is more suitable for studying our case of hydride precipitation.

By applying the alternative material equilibrium expression obtained above, two different boundary conditions are discussed, and a general expression for the effect of stress on the hydride precipitation solvus is obtained for a simplified model.

3.2. MATERIAL EQUILIBRIUM FOR STRESSED SOLIDS

3.2.1. Material Equilibrium in a Closed Thermodynamic System

First, let us look at the basic principle of thermodynamic equilibria, on which the internal energy minimization method is based: for the equilibrium of any isolated system, it is necessary and sufficient that in all possible variations in the state of the system which do not alter its entropy, the variation of its energy shall either vanish or be positive [79]. It can

be put as

$$(\delta U)_S \geq 0, \quad (3.1)$$

where U is the internal energy of the isolated system, and the subscript 'S' means that entropy is conserved. This is the second equivalent expression of equilibrium criterion of an isolated thermodynamic system, and is given as equation (2) in Gibbs' work [79]. Therefore, when deriving the equilibrium criteria, it is usual to let the variation of the system's internal energy be zero while recognizing the conservation of the entropy of the system.

In this work, the thermodynamic system we use to study the hydride precipitation is considered as a closed system, rather than an isolated one. The definitions of a closed system and an isolated system used in this work have been given in the introduction (section 3.1) of this chapter and again under nomenclature, and are consistent with those of most authors. This is appropriate, since the system we consider consists of the zirconium matrix and hydride precipitate, and during the hydride transformation, the system does not have mass exchange with its environment, but may have energy exchange, such as heat transfer or mechanical work through the external stress, with its surroundings. In order to apply the internal energy minimization method mentioned above, we first need to construct an isolated thermodynamic system which includes our thermodynamic system. Therefore, we let the closed system we consider (denoted as system I in the balance of section 3.2) plus the environment with which it interacts (denoted by a subscript 'env' in the balance of section 3.2) constitute an isolated thermodynamic system (denoted as system II in the balance of

section 3.2). Entropy is conserved in system II, and the variation of internal energy is also taken for system II.

We suppose that system I consists of two or more solid phases containing only interstitial solutes, and that its environment consists of the air and the loading system (which can be considered as solids). Both system I and its environment are enclosed in a fixed rigid envelope which is impermeable to either heat or mass, and are thus isolated from the outside of the envelope. We suppose that the loading system is firmly fixed on the envelope wherever they meet, and that the contact between the loading system and system I is a solid-solid interface, and the displacement on this interface has the nature of that of a coherent interface [81]. An example for this kind of contact is that the loading system is perfectly welded to system I wherever they meet. We suppose that the space between the envelope and system I and the loading system is completely filled with the air, which has a constant pressure. The reason we introduce the air as a part of the environment is that it gives the atmospheric pressure in the definition of Gibbs free energy in our later discussion. We further suppose that the surface of system I is continuous, which means we can move between any two points on this surface without leaving the surface. This eliminates any possible voids inside system I. Thus the surface of system I consists of two parts that are in contact with either the loading system or the air. It is assumed that there is no mass transfer between system I and its environment, and that the environment has reached material equilibrium, so that no mass exchange needs to be considered in it. Without affecting the final results achieved, gravity is ignored in the following discussion for brevity. The energy

of interfaces and its possible effect are also ignored.

In this work, for brevity, a Cartesian coordinate system X, Y and Z is assumed in describing any displacement and force. Before the infinitesimal deformation (in the reference state), any point of system I or the loading system (which is considered to be composed of solids) is associated with a set of coordinates x , y and z . After the infinitesimal deformation, the displacement of each point can be described by a set of three components of displacement \bar{u} , \bar{v} and \bar{w} , which are functions of x , y and z . When integrating with respect to volume or surface, the integral domain is taken on the volume or surface in the reference state before the infinitesimal deformation.

Using U_I to denote the internal energy of system I, and based on the assumption that it is a function of the entropy S , the strain ϵ_{ij} ($i, j = 1, 2, 3$) and the mole number $n_{k,l}$ of the interstitial solute k in phase l , the first variation of U_I is

$$\delta U_I = \int_{V'_I} \left(\frac{\partial u_I}{\partial s_I} \cdot \delta s_I + \frac{\partial u_I}{\partial \epsilon_{ij}} \cdot \delta \epsilon_{ij} + \sum_l \sum_k \frac{\partial u_I}{\partial \rho_{k,l}} \cdot \delta \rho_{k,l} \right) \cdot dV'_I, \quad (3.2)$$

where the integral is taken for the entire volume V'_I of system I in the reference state, dV'_I denoting a volume element in the integral; u_I , s_I and $\rho_{k,l}$ are the volume density of the internal energy, entropy and mole number of the interstitial solute k in phase l , respectively; summation over indices i and j is assumed in equation (3.2) and in the following. In this work, when we consider the equilibrium between the hydride precipitate and the zirconium matrix saturated with hydrogen, we assume it only involves interstitial hydrogen atom

movement in the zirconium atom lattice between the zirconium matrix which is to transform into the hydride and the surrounding zirconium matrix which does not transform. It is assumed that the interface which separates the two does not move, except for the displacement due to the strain. Therefore, the surface integral which takes this effect into account as in [79-81] is not considered here. A hydride precipitation model which takes into account the interface movement will be the objective of a separate work.

When considering the internal energy U_{env} of the environment with which system I interacts, the assumption is made that this environment is always at material equilibrium (hence one need not consider the variation of its composition), and that its internal energy U_{env} is a function of its entropy S and its volume V (for solids, this is equivalent to considering the strain ϵ_{ij}). The first variation of U_{env} is:

$$\begin{aligned} \delta U_{env} &= \int_{V'_{env}} \left(\frac{\partial u_{env}}{\partial s_{env}} \cdot \delta s_{env} + \frac{\partial u_{env}}{\partial v_{env}} \cdot \delta v_{env} \right) \cdot dV'_{env} \\ &= \int_{V'_{env}} \left(\frac{\partial u_{env}}{\partial s_{env}} \cdot \delta s_{env} \right) \cdot dV'_{env} + \int_{V'_{env}} \left(\frac{\partial u_{env}}{\partial v_{env}} \cdot \delta v_{env} \right) \cdot dV'_{env}, \end{aligned} \quad (3.3)$$

where the integral is taken for the entire volume V_{env}' of the environment in the reference state, dV_{env}' denoting a volume element in the integral, v_{env} being the ratio of the volume of a volume element at the point of interest after the infinitesimal deformation divided by its volume in the reference state, and the u_{env} and s_{env} here being the volume density of the internal energy and entropy, respectively. The first integral in equation (3.3) is due to the heat exchange, therefore the second integral must equal the mechanical work done on the

environment during the infinitesimal change. Equation (3.3) can thus be rewritten as

$$\begin{aligned} \delta U_{env} = & \int_{V'_{env}} \left(\frac{\partial u_{env}}{\partial s_{env}} \cdot \delta s_{env} \right) \cdot dV'_{env} + \int_{A^P} (p \cdot \delta N) \cdot dA^P \\ & + \int_{A^S} (X_{env} \cdot \delta \bar{u}_{env} + Y_{env} \cdot \delta \bar{v}_{env} + Z_{env} \cdot \delta \bar{w}_{env}) \cdot dA^S, \end{aligned} \quad (3.4)$$

where p is the air pressure, δN is the distance the surface of system I moves in the direction of the outward pointing normal for system I, dA^P is a surface element, and the integral is taken on A^P , which is the part of the surface of system I in contact with the air. Similarly, A^S is the part of the surface of system I in contact with the loading system, and dA^S is a surface element. X_{env} , Y_{env} , and Z_{env} are the three components of the force exerted on the loading system by system I at the surface element dA^S . $\delta \bar{u}_{env}$, $\delta \bar{v}_{env}$, and $\delta \bar{w}_{env}$ are the three components of the displacement at the surface element dA^S , which are positive if in the direction from the loading system to system I. Since the envelope which encloses system I and the environment is rigid, no variation of displacement is allowed along the envelope. Thus it does not do any mechanical work on the environment inside of it.

In equation (3.4), we have

$$\delta N = \delta \bar{u} \cdot \alpha + \delta \bar{v} \cdot \beta + \delta \bar{w} \cdot \gamma, \quad (3.5)$$

where α , β , and γ are the direction cosines of the normal to the surface of system I; $\delta \bar{u}$, $\delta \bar{v}$, and $\delta \bar{w}$ are the components of the displacement of the surface element dA^P , positive when in the direction from system I to the air. By the assumption that displacement is continuous

across A^s , we know

$$\delta \bar{u}_{env} = -\delta \bar{u}, \quad \delta \bar{v}_{env} = -\delta \bar{v}, \quad \delta \bar{w}_{env} = -\delta \bar{w}, \quad (3.6)$$

where $\delta \bar{u}$, $\delta \bar{v}$, and $\delta \bar{w}$ are the components of the displacement of the surface element dA^s , positive when in the direction from system I to the loading system. Thus equation (3.4) can be rewritten as

$$\begin{aligned} \delta U_{env} = & \int_{V'_{env}} \left(\frac{\partial u_{env}}{\partial s_{env}} \cdot \delta s_{env} \right) \cdot dV'_{env} \\ & + \int_{A^p} (p\alpha \cdot \delta \bar{u} + p\beta \cdot \delta \bar{v} + p\gamma \cdot \delta \bar{w}) \cdot dA^p \\ & - \int_{A^s} (X_{env} \cdot \delta \bar{u} + Y_{env} \cdot \delta \bar{v} + Z_{env} \cdot \delta \bar{w}) \cdot dA^s. \end{aligned} \quad (3.7)$$

Equation (3.2) can be written as

$$\begin{aligned} \delta U_I = & \int_{V'_I} \left(\frac{\partial u_I}{\partial s_I} \cdot \delta s_I + \sum_l \sum_k \frac{\partial u_I}{\partial \rho_{k,l}} \cdot \delta \rho_{k,l} \right) \cdot dV'_I \\ & + \int_{V'_I} (\sigma_{xx} \cdot \delta \epsilon_{xx} + \sigma_{yy} \cdot \delta \epsilon_{yy} + \sigma_{zz} \cdot \delta \epsilon_{zz} \\ & + \sigma_{yz} \cdot \delta \gamma_{yz} + \sigma_{zx} \cdot \delta \gamma_{zx} + \sigma_{xy} \cdot \delta \gamma_{xy}) \cdot dV'_I. \end{aligned} \quad (3.8)$$

Applying the Gauss divergence theorem, and through integration by parts such as

$$\int_V \left(\frac{\partial \sigma_{xx}}{\partial x} \cdot \delta \bar{u} \right) \cdot dV = \int_S (\sigma_{xx} \alpha \cdot \delta \bar{u}) \cdot dS - \int_V (\sigma_{xx} \cdot \frac{\partial \delta \bar{u}}{\partial x}) \cdot dV, \quad (3.9)$$

we may transform equation (3.8) into

$$\begin{aligned}
\delta U_I = & \int_{V'_I} \left(\frac{\partial u_I}{\partial s_I} \cdot \delta s_I + \sum_l \sum_k \frac{\partial u_I}{\partial \rho_{k,l}} \cdot \delta \rho_{k,l} \right) \cdot dV'_I \\
& - \int_{V'_I} \left[\left(\frac{\partial \sigma_{xx}}{\partial x} + \frac{\partial \sigma_{xy}}{\partial y} + \frac{\partial \sigma_{xz}}{\partial z} \right) \cdot \delta \bar{u} + \left(\frac{\partial \sigma_{yx}}{\partial x} + \frac{\partial \sigma_{yy}}{\partial y} + \frac{\partial \sigma_{yz}}{\partial z} \right) \cdot \delta \bar{v} \right. \\
& \quad \left. + \left(\frac{\partial \sigma_{zx}}{\partial x} + \frac{\partial \sigma_{zy}}{\partial y} + \frac{\partial \sigma_{zz}}{\partial z} \right) \cdot \delta \bar{w} \right] \cdot dV'_I \\
& + \int_A \left[(\sigma_{xx} \alpha + \sigma_{xy} \beta + \sigma_{xz} \gamma) \cdot \delta \bar{u} + (\sigma_{yx} \alpha + \sigma_{yy} \beta + \sigma_{yz} \gamma) \cdot \delta \bar{v} \right. \\
& \quad \left. + (\sigma_{zx} \alpha + \sigma_{zy} \beta + \sigma_{zz} \gamma) \cdot \delta \bar{w} \right] \cdot dA.
\end{aligned} \tag{3.10}$$

Note that here the surface A of system I consists of A^p and A^s .

The first variation of the total internal energy of the isolated system II is

$$\delta U_{II} = \delta U_I + \delta U_{env}. \tag{3.11}$$

Combining equations (3.7), (3.10) and (3.11), we get

$$\begin{aligned}
\delta U_{II} = & \int_{V'_I} \left(\frac{\partial u_I}{\partial s_I} \cdot \delta s_I + \sum_l \sum_k \frac{\partial u_I}{\partial \rho_{k,l}} \cdot \delta \rho_{k,l} \right) \cdot dV'_I \\
& + \int_{V'_{env}} \left(\frac{\partial u_{env}}{\partial s_{env}} \cdot \delta s_{env} \right) \cdot dV'_{env} \\
& - \int_{V'_I} \left[\left(\frac{\partial \sigma_{xx}}{\partial x} + \frac{\partial \sigma_{xy}}{\partial y} + \frac{\partial \sigma_{xz}}{\partial z} \right) \cdot \delta \bar{u} + \left(\frac{\partial \sigma_{yx}}{\partial x} + \frac{\partial \sigma_{yy}}{\partial y} + \frac{\partial \sigma_{yz}}{\partial z} \right) \cdot \delta \bar{v} \right. \\
& \quad \left. + \left(\frac{\partial \sigma_{zx}}{\partial x} + \frac{\partial \sigma_{zy}}{\partial y} + \frac{\partial \sigma_{zz}}{\partial z} \right) \cdot \delta \bar{w} \right] \cdot dV'_I \\
& + \int_{A^p} \left[(\sigma_{xx} \alpha + \sigma_{xy} \beta + \sigma_{xz} \gamma + p \alpha) \cdot \delta \bar{u} + (\sigma_{yx} \alpha + \sigma_{yy} \beta + \sigma_{yz} \gamma + p \beta) \cdot \delta \bar{v} \right. \\
& \quad \left. + (\sigma_{zx} \alpha + \sigma_{zy} \beta + \sigma_{zz} \gamma + p \gamma) \cdot \delta \bar{w} \right] \cdot dA^p \\
& + \int_{A^s} \left[(\sigma_{xx} \alpha + \sigma_{xy} \beta + \sigma_{xz} \gamma - X_{env}) \cdot \delta \bar{u} + (\sigma_{yx} \alpha + \sigma_{yy} \beta + \sigma_{yz} \gamma - Y_{env}) \cdot \delta \bar{v} \right. \\
& \quad \left. + (\sigma_{zx} \alpha + \sigma_{zy} \beta + \sigma_{zz} \gamma - Z_{env}) \cdot \delta \bar{w} \right] \cdot dA^s.
\end{aligned} \tag{3.12}$$

The variations in equation (3.12) are subject to two constraints:

(1) the total entropy of the isolated system II is conserved:

$$\int_{V'_l} \delta s_l \cdot dV'_l + \int_{V'_{env}} \delta s_{env} \cdot dV'_{env} = 0; \quad (3.13)$$

(2) the mass of each interstitial solute k is conserved:

$$\int_{V'_l} (\sum_l \delta \rho_{k,l}) \cdot dV'_l = 0, \quad \text{for } k = 1, 2, 3, \dots \quad (3.14)$$

In order to apply these two constraints to equation (3.12), we introduce a Lagrange multiplier t for equation (3.13), and Lagrange multipliers λ_k ($k = 1, 2, 3, \dots$) for each equation (3.14-k). We then add equation (3.13) multiplied by t and each equation (3.14-k) multiplied by λ_k ($k = 1, 2, 3, \dots$) to equation (3.12), and get an unconstrained variation of independent variables.

Equating this variation to zero, we can get the conditions for equilibrium:

(1) the thermal equilibrium condition:

$$t = \left(\frac{\partial u}{\partial S} \right)_{v, \rho_{k,l}}, \text{ constant throughout } V'_l, V'_{env}, \quad (3.15)$$

which requires that the temperature is constant throughout the entire system II;

(2) the material equilibrium conditions for each interstitial solute k:

$$\lambda_k = \left(\frac{\partial u_l}{\partial \rho_{k,l}} \right)_{s_l, v_l}, \text{ for } l = 1, 2, 3, \dots \quad (3.16)$$

which requires that the chemical potential of each interstitial solute k is constant throughout

V_1' ;

(3) the mechanical equilibrium conditions, which require that:

$$\begin{aligned}\frac{\partial \sigma_{xx}}{\partial x} + \frac{\partial \sigma_{xy}}{\partial y} + \frac{\partial \sigma_{xz}}{\partial z} &= 0, \\ \frac{\partial \sigma_{yx}}{\partial x} + \frac{\partial \sigma_{yy}}{\partial y} + \frac{\partial \sigma_{yz}}{\partial z} &= 0, \\ \frac{\partial \sigma_{zx}}{\partial x} + \frac{\partial \sigma_{zy}}{\partial y} + \frac{\partial \sigma_{zz}}{\partial z} &= 0,\end{aligned}\tag{3.17}$$

in volume V_1' , and

$$\begin{aligned}\sigma_{xx}\alpha + \sigma_{xy}\beta + \sigma_{xz}\gamma &= -p\alpha, \\ \sigma_{yx}\alpha + \sigma_{yy}\beta + \sigma_{yz}\gamma &= -p\beta, \\ \sigma_{zx}\alpha + \sigma_{zy}\beta + \sigma_{zz}\gamma &= -p\gamma,\end{aligned}\tag{3.18}$$

on the surface A^P of system I, and

$$\begin{aligned}\sigma_{xx}\alpha + \sigma_{xy}\beta + \sigma_{xz}\gamma &= X_{env}, \\ \sigma_{yx}\alpha + \sigma_{yy}\beta + \sigma_{yz}\gamma &= Y_{env}, \\ \sigma_{zx}\alpha + \sigma_{zy}\beta + \sigma_{zz}\gamma &= Z_{env},\end{aligned}\tag{3.19}$$

on the surface A^s of system I. Equation (3.17) gives the mechanical equilibrium conditions for each volume element in V_1' in the three directions X, Y, and Z. Equations (3.18) and (3.19) give the mechanical equilibrium conditions on surfaces A^P and \bar{A} of system I respectively. On A^P , the force exerted by the interior of system I on a surface element dA^P must be normal to the surface and equal in magnitude (but opposite in direction) to the air pressure p . On A^s , the force exerted by the interior of system I on a surface element dA^s is

equal to the force exerted by that surface element on the loading system. An equivalent statement is: on A^s , the force exerted by the interior of system I on a surface element dA^s is equal in magnitude (but opposite in direction) to the force exerted by the loading system on that surface element.

As mentioned in section 3.1 of this chapter, the material equilibrium conditions expressed in chemical potential uniformity as given by equation (3.16), when applied to our case of hydride precipitation, do not directly reflect the effect of the external stress. In the following discussion, one will see that, for a simple closed thermodynamic system which consists of two solid phases with one interstitial solute, the material equilibrium conditions have an alternative expression which can be conveniently used to study the case of hydride precipitation.

3.2.2. An Alternative Expression of the Material Equilibrium Condition

Now we will show that, the material equilibrium conditions given in equation (3.16) can be alternatively expressed as $dG_I = \delta W$, for the closed thermodynamic system (system I) if the system consists of only two solid phases with one interstitial solute. Here dG_I is the total change in Gibbs free energy of system I, δW being the total mechanical work done on system I by an external stress. This expression is the material equilibrium criterion we will later use to derive the expression for the effect of stress on the hydride precipitation in zirconium.

We have proven in section 3.2.1 that when the isolated thermodynamic system II is in equilibrium, the temperature is constant throughout system I and its environment, and the chemical potential of each interstitial solute k is constant throughout system I. The air pressure p is constant by assumption. Therefore, in the following discussion, the constant temperature and atmospheric pressure conditions are assumed. This assumption not only gives brevity to the derivation but is also sufficient and appropriate for our issue of hydride precipitation in zirconium. To be consistent with conventions, we use T and P to represent the temperature and the atmospheric pressure. When we consider the mass exchange in system I, for brevity, we assume the chemical potential of each interstitial solute k is constant in each phase l . When material equilibrium is reached, this chemical potential is then equal in all the phases. Hence we can use μ_{kl} to represent the chemical potential of interstitial solute k in phase l . In our derivation, we first do not limit the number of phases and solutes, but will do that when we draw conclusions.

The system I we considered above is a closed system consisting of two or more solid phases containing only interstitial solutes, which, besides heat exchange, has only two other means of energy exchange with its environment: (i) the P - V work, which is the mechanical work done on system I by the air through the atmospheric pressure P . As mentioned in section 3.2.1 when we construct the isolated thermodynamic system II, the reason we consider the effect of the air is that it gives the atmospheric pressure P in the definition of Gibbs free energy in our later discussion; and (ii) the work done by the external stress, which is the mechanical work done on system I by the loading system. In the following discussion,

we no longer use the term “the loading system”, but use “the external stress” to represent this effect.

When system I is at thermal and mechanical equilibrium, for an infinitesimal change, we have, from the Gibbs equation of internal energy under stress as given in equation (3.2):

$$dU_I = TdS_I + dw + \sum_l \sum_k \frac{\partial U_I}{\partial n_{k,l}} \cdot \delta n_{k,l}, \quad (3.20)$$

where dU_I is the change of the internal energy of system I, T is the temperature, S_I is the total entropy of system I, dw is the work done on system I by its environment, and $n_{k,l}$ is the mole number of interstitial solute k in phase l .

In equation (3.20), dw consists of the contributions from both the P-V work and the work done by the external stress. Substituting dw by $-PdV_I + \delta W$, where δW is the work done on system I by the external stress, one obtains:

$$dU_I = TdS_I - PdV_I + \delta W + \sum_l \sum_k \frac{\partial U_I}{\partial n_{k,l}} \cdot \delta n_{k,l}. \quad (3.21)$$

In order to apply the thermal and mechanical equilibrium conditions, one may add and subtract $S_I dT$ and $V_I dP$ from equation (3.21):

$$dU_I = TdS_I + S_I dT - S_I dT - PdV_I + V_I dP - V_I dP + \delta W + \sum_l \sum_k \frac{\partial U_I}{\partial n_{k,l}} \cdot \delta n_{k,l}, \quad (3.22)$$

i.e.

$$d(U_I + PV_I - TS_I) = -S_I dT + V_I dP + \delta W + \sum_l \sum_k \frac{\partial U_I}{\partial n_{k,l}} \cdot \delta n_{k,l} \quad (3.23)$$

Applying the conditions $dT = 0$ and $dP = 0$ to equation (3.23), one gets

$$dG_I = \delta W + \sum_l \sum_k \frac{\partial U_I}{\partial n_{k,l}} \cdot \delta n_{k,l}, \quad (\text{constant } T, P) \quad (3.24)$$

where $G_I = U_I + PV_I - TS_I$ is the Gibbs free energy, and δW is the mechanical work done on system I by the external stress.

In the above derivation, equation (3.20) is based on the definition of internal energy, and from equation (3.20) to (3.24), only the thermal and mechanical equilibrium conditions are applied. Therefore, equation (3.24) is a general equation for system I under thermal and mechanical equilibrium.

The second term on the right side of equation (3.24) is due to the material exchange between different phases within system I. When system I is in material equilibrium, because the chemical potential of each interstitial solute is constant and its mass is conserved, this quantity is zero and we have:

$$\sum_l \sum_k \frac{\partial U_I}{\partial n_{k,l}} \cdot \delta n_{k,l} = 0. \quad (3.25)$$

So if we invoke the material equilibrium condition, from equation (3.24) we obtain

$$dG_I = \delta W. \quad (3.26)$$

When system I is under thermal and mechanical equilibrium, equation (3.25) is equivalent to equation (3.26), since equation (3.24) generally holds under the specified conditions. And when system I consists of only two phases containing one interstitial solute, equation (3.25) actually represents the material equilibrium condition. This is because, when the system consists of two phases containing one interstitial solute, as we later assume in our model of hydride precipitation in zirconium, we have $l = 2$ and $k = 1$. Here the two phases are zirconium and hydride respectively, and the one interstitial solute is hydrogen. Equation (3.25) can thus be rewritten as:

$$\frac{\partial U_\alpha}{\partial n_{H,\alpha}} \cdot \delta n_{H,\alpha} + \frac{\partial U_\delta}{\partial n_{H,\delta}} \cdot \delta n_{H,\delta} = 0, \quad (3.27)$$

where α and δ represent the zirconium and hydride phase respectively. Since the hydrogen in the closed system is conserved, i.e.

$$\delta n_{H,\alpha} + \delta n_{H,\delta} = 0, \quad (3.28)$$

one has, from equations (3.27) and (3.28),

$$\frac{\partial U_\alpha}{\partial n_{H,\alpha}} = \frac{\partial U_\delta}{\partial n_{H,\delta}}, \quad (3.29)$$

which represents the material equilibrium condition of the system.

Therefore, equation (3.26) also expresses the material equilibrium for system I. We will see that equation (3.26) is more suitable for deriving the effect of stress on the hydrogen solubilities.

3.3. THE EFFECT OF STRESS ON HYDRIDE PRECIPITATION SOLVUS IN STRESSED ZIRCONIUM

Now we will establish the relationship between the precipitation solvi of hydrogen in stressed and in non-stressed zirconium matrices, by introducing the material equilibrium criterion obtained above.

Figure 3.1(a) and (b) illustrate the precipitation of hydride from the non-stressed and stressed zirconium matrices, respectively. For simplicity, here it is assumed that the precipitation of hydride from the zirconium matrix is completely coherent. The interfacial energy and its possible effect are not considered. Small elastic strain is also assumed, so that the procedure of applying the stress to the system is reversible, and the simplified relationship between the chemical potential of hydrogen in stressed and in non-stressed zirconium is valid [31]. The thermodynamic system considered here consists of the whole zirconium matrix before the transformation, and the precipitated hydride phase plus the

untransformed zirconium matrix after the transformation.

In this work, when we describe the hydride transformation in a non-stressed state, we define it as an absolutely stress-free procedure: i.e. no constraint in either matrix or precipitate is considered. It is assumed that the volume change due to hydride formation and the taking away of hydrogen from the zirconium matrix is completely accommodated by the volume change of the entire system, without creating any, or only a negligible amount of, strain in the zirconium matrix and hydride precipitate. This, we suppose, might be the meaning of a true "stress-free" hydrogen solubility. In our description of the hydride precipitation in a stressed state, we first consider it as a constant-traction boundary condition: the external stress will not be changed by the volume change due to hydride formation, and the stresses are constant and uniform throughout the matrix before and after the transformation, and uniform throughout the precipitate after the transformation. This is because any attempt to consider the non-uniformity of stress and strain must take into account the geometry and position of the precipitate and the relative amount of precipitate and matrix. Here, we use this model to reflect the effect of stress on the hydride precipitation solvus. In section 3.4, the precipitation is considered for a different boundary condition, and the non-uniformity effect will be considered. Therefore, in the balance of this section, average strain energy densities are used to describe the strain energy stored in both the zirconium matrix and the hydride precipitate.

In figure 3.1(a), the total change in the Gibbs free energy of the system, when δn moles of non-stressed zirconium matrix absorbs $x\delta n$ moles of hydrogen (here $x = 1.67$) and

forms δn moles of non-stressed hydride, is

$$dG_{\alpha-\delta}^{n-s} = (\bar{G}_{\delta}^{n-s} - \bar{G}_{\alpha}^{n-s}) \cdot \delta n - \mu_{H,\alpha}^{n-s} \cdot x\delta n, \quad (3.30)$$

where α and δ denote zirconium matrix and hydride, respectively; the superscript 'n-s' denotes the non-stressed state; \bar{G}_{α}^{n-s} and \bar{G}_{δ}^{n-s} are the molal Gibbs free energy of the non-stressed zirconium matrix and the non-stressed hydride, respectively; and $\mu_{H,\alpha}^{n-s}$ is the chemical potential of hydrogen in the non-stressed zirconium matrix. To obtain equation (3.30), we first separate the system into two parts: the δn moles of zirconium matrix which is to transform into the δn moles of hydride, and the remaining zirconium matrix. For the δn moles of zirconium matrix, its Gibbs free energy before and after the transformation is $\bar{G}_{\alpha}^{n-s} \cdot \delta n$ and $\bar{G}_{\delta}^{n-s} \cdot \delta n$, respectively. Hence, the change in the Gibbs free energy of this part of the system is given by $(\bar{G}_{\delta}^{n-s} - \bar{G}_{\alpha}^{n-s}) \cdot \delta n$. During the transformation, $x\delta n$ moles of hydrogen is taken from the remaining zirconium matrix, so the change in the Gibbs free energy of the remaining zirconium matrix is $-\mu_{H,\alpha}^{n-s} \cdot x\delta n$. The total change in the Gibbs free energy of the whole system is therefore given by equation (3.30).

Similarly, in figure 3.1(b), the total change in the Gibbs free energy of the system, when δn moles of stressed zirconium matrix absorbs $x\delta n$ moles of hydrogen and forms δn moles of stressed hydride, is:

$$dG_{\alpha-\delta}^a = (\bar{G}_{\delta}^a - \bar{G}_{\alpha}^a) \cdot \delta n - \mu_{H,\alpha}^a \cdot x\delta n - p \cdot \bar{V}_{H,\alpha} \cdot x\delta n, \quad (3.31)$$

where the superscript 'a' denotes that the phases are under applied external stress; \bar{G}_{α}^a and \bar{G}_{δ}^a

are the molal Gibbs free energy of the stressed zirconium matrix and the stressed hydride, respectively; $\mu_{H,\alpha}^a$ is the chemical potential of hydrogen in the stressed zirconium matrix; $p = (\sigma_{ii} + \sigma_{jj} + \sigma_{kk})/3$ being the hydrostatic stress and $\bar{V}_{H,\alpha}$ being the partial molal volume of hydrogen in zirconium. In obtaining equation (3.31), we still divide the system into two parts: the δn moles of zirconium matrix to be transformed into the δn moles of hydride, and the remaining zirconium matrix. Here when we consider the change in the Gibbs free energy of the remaining zirconium matrix, when $x\delta n$ moles of hydrogen is taken from it to form δn moles of hydride, beside the term $-\mu_{H,\alpha}^a \cdot x\delta n$, the mechanical work done on this part of the zirconium matrix by the external stress due to the taking away of $x\delta n$ moles of hydrogen from it, which is $-p \cdot \bar{V}_{H,\alpha} \cdot x\delta n$, should also be included.

When the material equilibrium condition, as given in equation (3.26), is applied to equations (3.30) and (3.31), we can get the relationship between the precipitation solvi of hydrogen in the stressed and in the non-stressed zirconium matrix. In figure 3.1(b), the total mechanical work done by the external stress on the system during the hydride precipitation is:

$$\delta W = -p \cdot \bar{V}_{H,\alpha} \cdot x\delta n + p \cdot \bar{V}_{\alpha-\delta} \cdot \delta n, \quad (3.32)$$

where $\bar{V}_{\alpha-\delta}$ is the volume increase when one mole of zirconium matrix absorbs x moles of hydrogen (here $x = 1.67$) and forms one mole of hydride. In figure 3.1(a), this total mechanical work is zero, since there is no external stress applied on the system. So we have, by applying $dG = 0$ and $dG = \delta W$ to equations (3.30)-(3.32):

$$(\bar{G}_{\delta}^{n-s} - \bar{G}_{\alpha}^{n-s}) - x \cdot \mu_{H,\alpha}^{n-s} = 0, \quad (3.33)$$

and

$$(\bar{G}_{\delta}^a - \bar{G}_{\alpha}^a) - x \cdot \mu_{H,\alpha}^a - p \cdot \bar{V}_{\alpha-\delta} = 0. \quad (3.34)$$

Combining equations (3.33) and (3.34), we get

$$x \cdot (\mu_{H,\alpha}^a - \mu_{H,\alpha}^{n-s}) = (\bar{G}_{\delta}^a - \bar{G}_{\delta}^{n-s}) - (\bar{G}_{\alpha}^a - \bar{G}_{\alpha}^{n-s}) - p \cdot \bar{V}_{\alpha-\delta}. \quad (3.35)$$

In equation (3.35), assuming an ideal solution, we obtain:

$$\mu_{H,\alpha}^a - \mu_{H,\alpha}^{n-s} = (RT \ln x_2 - p \cdot \bar{V}_{H,\alpha}) - RT \ln x_1, \quad (3.36)$$

where x_1 , x_2 are the precipitation solvi of hydrogen in the non-stressed and the stressed zirconium, respectively; and $\bar{V}_{H,\alpha}$ is the partial molal volume of hydrogen in zirconium. Under the elastic strain assumption, the procedure of applying stress to a solid is reversible, and the difference in Gibbs free energy of a solid in stressed and non-stressed states is equal to its elastic energy, as reflected in equation (3.26). Therefore we have:

$$\bar{G}_{\delta}^a - \bar{G}_{\delta}^{n-s} = \bar{W}_{\delta}^a, \quad (3.37)$$

where \bar{W}_{δ}^a is the strain energy per mole of the stressed hydride. In a similar way as for obtaining equations (3.36) and (3.37), we have:

$$\begin{aligned} \bar{G}_\alpha^a - \bar{G}_\alpha^{a-s} = & [(1 - x_2)RT\ln(1 - x_2) + x_2RT\ln x_2] + \bar{W}_\alpha^a \\ & - [(1 - x_1)RT\ln(1 - x_1) + x_1RT\ln x_1], \end{aligned} \quad (3.38)$$

where \bar{W}_α^a is the strain energy per mole of the stressed zirconium matrix. Applying equations (3.36) through (3.38) to equation (3.35), and since $x_1, x_2 \ll 1$, we get

$$xRT\ln(x_2/x_1) = (\bar{W}_\delta^a - \bar{W}_\alpha^a) - p \cdot \bar{V}_{\alpha-\delta} + xp \cdot \bar{V}_{H,\alpha}, \quad (3.39)$$

i.e.

$$\frac{x_2}{x_1} = \exp\left(\frac{\bar{W}_\delta^a - \bar{W}_\alpha^a}{xRT}\right) \cdot \exp\left(\frac{-p \cdot \bar{V}_{\alpha-\delta}}{xRT}\right) \cdot \exp\left(\frac{p \cdot \bar{V}_{H,\alpha}}{RT}\right), \quad (3.40)$$

which is the expression for the relationship between the precipitation solvus of hydrogen in the stressed zirconium matrix and the precipitation solvus of hydrogen in the non-stressed zirconium matrix. Equation (3.40) is obtained based on a constant-traction boundary condition, and the assumption of uniform stress in both the zirconium matrix and hydride precipitate. In the following, by considering a different boundary condition, we will develop an expression for a more general case.

3.4. CONSIDERATION OF A DIFFERENT BOUNDARY CONDITION

In section 3.3, we considered the hydride formation under stress to happen in a system with a constant-traction boundary condition. In the following, by using the material equilibrium condition given by equation (3.26), we will discuss a similar precipitation but in a system with a zero displacement boundary condition.

We suppose the system is initially stressed at the outer periphery, but subject to a zero displacement boundary condition during the hydride formation, i.e. the boundary of the system has a zero displacement, and the mechanical work done on the system by the external stress is therefore zero. The volume change due to the hydride formation and the taking away of hydrogen from the zirconium matrix is assumed to be completely accommodated by the change of strain in the zirconium matrix and the strain in the precipitate. (This situation may correspond to that of a small hydride precipitated in a large volume of zirconium matrix. The volume change effect decreases with distance from the hydride, and beyond a certain distance we may assume it to be negligible. The change in hydrogen concentration due to the hydride formation also decreases with distance, until beyond a certain distance where the change is negligible. The more remote one of these two distances is taken as the outer periphery of the system, so that the system has no mass exchange with its environment and its periphery will neither expand nor contract during the hydride formation.) The stress and strain energy distribution in the zirconium matrix and hydride precipitate depends on the geometry of the

precipitate, the precipitate distribution in the matrix and the external stress. Here we will not go into any specific case, but give the general relation between the stress and strain energy terms and the hydride precipitation solvus. We still use average strain energy densities to describe the elastic strain energy stored in both the hydride precipitate and zirconium matrix. By using analytical or numerical methods, the average strain energy densities associated with different cases can be calculated once the geometry and stress condition for each case are determined. We also assume that the redistribution of hydrogen in the zirconium matrix due to the non-uniformity of stress [31] has reached equilibrium both before and after the hydride transformation, so that the chemical potential of hydrogen in the zirconium matrix is uniform.

The total change in Gibbs free energy of the system during the hydride formation is given by:

$$dG_{\alpha-\delta}^{a-inc} = (\overline{G}_{\delta}^{a-inc} - \overline{G}_{\alpha}^a) \cdot \delta n + (\overline{G}_{\alpha'}^{a-inc} - \overline{G}_{\alpha}^a) \cdot (n_{\alpha} - \delta n), \quad (3.41)$$

where the superscript 'a' denotes that the phases are under the initial applied external stress, and 'a+inc' denotes the phases are under the external stress modified by the formation of hydride precipitates; $\overline{G}_{\delta}^{a-inc}$ is the molal Gibbs free energy of hydride under the specified stress; $\overline{G}_{\alpha'}^{a-inc}$ and \overline{G}_{α}^a are molal Gibbs free energy of zirconium matrix after and before hydride transformation, respectively; α' denoting the zirconium with a lower hydrogen concentration than original due to hydride formation; here the molal Gibbs free energy terms are mole average values, since the phases may not be uniform; n_{α} is the number of moles of

zirconium matrix before transformation. By equation (3.26), one knows the total change in the Gibbs free energy of the system should equal zero, since the work done by the external stress on the system is zero. One has:

$$(\bar{G}_{\delta}^{a-inc} - \bar{G}_{\alpha}^a) \cdot \delta n + (\bar{G}_{\alpha'}^{a-inc} - \bar{G}_{\alpha}^a) \cdot (n_{\alpha} - \delta n) = 0. \quad (3.42)$$

By going through a similar discussion as in section 3.3, one gets:

$$\frac{x_2}{x_1} = \exp\left(\frac{\bar{W}_{\alpha-\delta}^{a-a-inc}}{xRT}\right), \quad (3.43)$$

where $\bar{W}_{\alpha-\delta}^{a-a-inc}$ is the total change in strain energy of the system during the hydride formation, if one mole of hydride is formed in this way. Equation (3.43) is similar in appearance to the result of the fully constrained hydride precipitation solvus as given by Puls [77]. This indicates that, as far as the effect of strain energy on the hydride precipitation solvus is concerned, the situation when the precipitation is subject to misfit constraint but under no external stress is similar to the situation when there is external stress but the system is subject to a zero displacement boundary condition so that the mechanical work by the external stress is zero, although the stress and strain distribution in the two cases can be quite different.

The results given by equations (3.40) and (3.43) actually represent two extreme conditions: In the former case, the volume change is completely accommodated by the volume change of the whole system, while in the latter one, the volume change due to the

hydride formation and the taking away of hydrogen from the zirconium matrix is completely accommodated by the change of strain in the matrix and the strain in precipitate. In a more general way, the effect of external stress on the hydride precipitation solvus in zirconium, under the assumptions of coherent precipitation and small elastic deformation, can be expressed as

$$\frac{x_2}{x_1} = \exp\left(\frac{\overline{W}_{\alpha-\delta}^{a-a-inc} - \delta W}{xRT}\right), \quad (3.44)$$

where $\overline{W}_{\alpha-\delta}^{a-a-inc}$ is the total change in strain energy of the system during the hydride formation, and δW the total mechanical work done on the system by the external stress during the hydride formation, which are all measured by considering that one mole of hydride is formed in this way. Here, the periphery of the system must be so defined that there is no hydrogen diffusing across it, so as to insure a closed thermodynamic system; and the hydrogen redistribution in the zirconium matrix due to the non-uniformity of stress is assumed to have reached equilibrium before and after the hydride transformation.

3.5. DISCUSSION

The equation given by Puls [77] for the effect of stress on the hydrogen precipitation solvus can be written as

$$\frac{x_2}{x_1} = \exp\left(\frac{\overline{W}_t^{inc}}{xRT}\right) \cdot \exp\left(\frac{\overline{W}_t^a}{xRT}\right) \cdot \exp\left(\frac{p \cdot \overline{V}_{H,\alpha}}{RT}\right), \quad (3.45)$$

where \overline{W}_t^{inc} is the strain energy due to the misfit between the hydride precipitated and the matrix, and \overline{W}_t^a is the Eshelby's interaction energy term [88]. If we compare equation (3.45) with the results obtained in this work for a similar precipitation, *i.e.* equation (3.40), we can see that: the last terms for both equations are identical, and they all refer to the mechanical work due to the taking away of a certain amount of hydrogen in the surrounding matrix due to the hydride formation. The second terms in both equations refer to the mechanical work by the external stress due to the volume increase during the hydride formation. But here the hydride precipitation considered in this work is a little different from the phase transformation considered in Eshelby's work [88], because in the latter work, the mass transfer from the surrounding matrix into the new precipitate is not explicitly considered. Therefore, applying the Eshelby's interaction energy term here to the hydride precipitation may not be accurate. The first term in equation (3.45) is due to the misfit strain energy caused by the volume dilation of hydride precipitation. This term does not apply to the

situations considered in equation (3.40), because for equation (3.40) it is assumed that this volume dilation is completely accommodated by the volume increase of the whole system (system I), and therefore does not cause any misfit strain energy. Now one can see that there is one energy term left, that is the first term in equation (3.40). This term is caused by the difference between the strain energy in the hydride that is formed and the zirconium matrix that is transformed into this hydride. This term is missing in equation (3.40).

Compared with equations (3.40) and (3.45), equation (3.44) is for a more general case and is accurate under the assumptions of elastic deformation and coherent precipitation.

When we establish the material equilibrium conditions such as given by equations (3.33) and (3.34) for hydride precipitation in both non-stressed and stressed zirconium matrices, assumptions on the hydride precipitation mechanism are avoided, by directly discussing the initial and the final states of the system. Whether or not the transformation can actually occur still depends on the potential energy barrier the system needs to overcome, when changing from the initial state to the final state. This potential barrier is related to the actual hydride precipitation mechanism in the zirconium matrix, and is beyond the capability of classical equilibrium thermodynamics.

The application of equation (3.26) has its limitation. As one can see from section 3.2 of this work, equation (3.25), and therefore equation (3.26), express the material equilibrium condition only when the closed system (system I) consists of two solid phases containing one interstitial solute (or one independently variable component). When more phases or more solutes are present, equation (3.25) or (3.26) is only the necessary condition and not the

sufficient condition for material equilibrium of the system. In this sense, when the closed system contains more than two solid phases or more than one independently variable component, an infinitesimal thermodynamic process of the system that can be described by equation (3.26) is not necessarily associated with the material equilibrium state of the system. Therefore, equation (3.26) may not be applicable for studying the material equilibria in those cases.

Our model for the hydride precipitation, as illustrated in figure 3.1 and discussed in sections 3.3 and 3.4, may need to be refined. From the hysteresis phenomenon of hydrogen solvi in zirconium, we know that the plastic deformation and surface energy are involved in hydride precipitation and the precipitation may not be coherent [77]. Therefore, the interfacial energy and its effect, and the plastic deformation may need to be taken into account.

3.6. CONCLUSIONS

The material equilibrium of a closed system under external stress, which consists of two or more solid phases containing only interstitial solutes, is discussed using the internal energy minimization method. For the closed system corresponding to a simplified model of hydride precipitation in zirconium, the material equilibrium condition has an alternative expression which is more suitable for studying the effect of stress on the hydride precipitation solvus. By applying this alternative material equilibrium expression, a general relationship for the effect of external stress on the hydride precipitation solvus in zirconium is obtained for the simplified model.

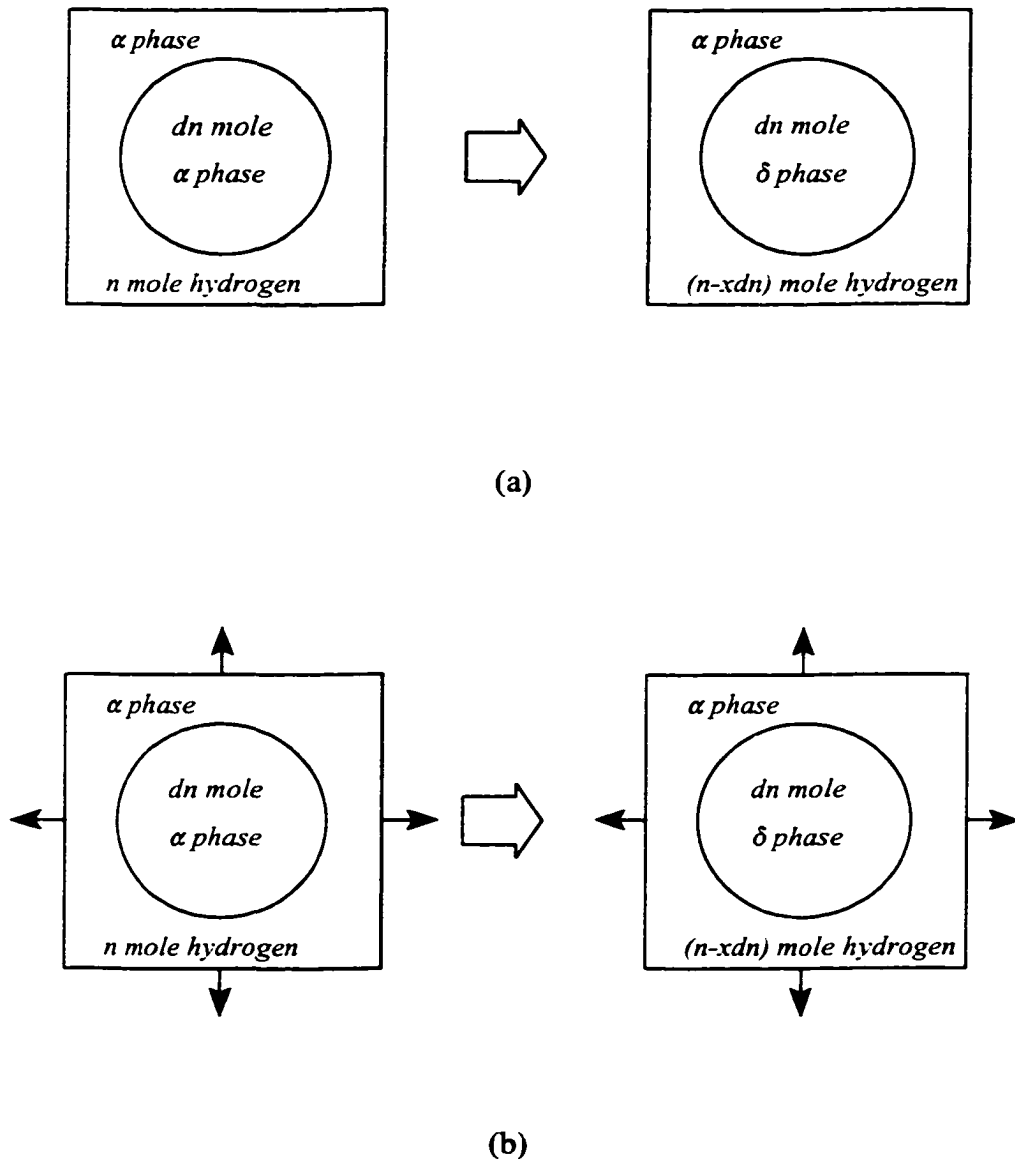


Figure 3.1. Diagram illustrating the hydride (denoted as δ phase) precipitation from the zirconium matrix (denoted as α phase) under (a) no stress; and (b) stress.

CHAPTER 4. THE MECHANISM OF K_{IH} IN DELAYED HYDRIDE CRACKING OF Zr-2.5wt% Nb AT 150°C**ABSTRACT**

The K_{IH} mechanism in delayed hydride cracking (DHC) of Zr-2.5wt% Nb alloys was studied using a modified experimental method. A new R-curve phenomenon that characterizes the resistance to DHC was observed. K_{IH} is thus defined. The critical hydride cluster length at different K_I was measured. It was found that this curve could be used to explain the behavior of the DHC velocity vs. K_I curve. Using the theoretical work of Zheng *et al.*, the energy required to form the fracture surfaces was determined from the experiments. These energies were used to analyze the results. This experimental work also showed that cracking sometimes started in hydrides in the middle of the hydride cluster while the cluster end closer to the crack tip was still unfractured. A qualitative K_{IH} model that incorporates the effect of both stress and energy is proposed.

4.1. INTRODUCTION

4.1.1. The K_{IH} Issues

The Zr-2.5wt% Nb alloy has long been used to fabricate the pressure tubes of the primary heat transport system in CANDU (Canadian Deuterium Uranium) nuclear reactors. This kind of alloy, despite its excellent combination of mechanical properties and low neutron absorption, is sometimes susceptible to a fracture mechanism called delayed hydride cracking (DHC). Since the first observation of cracking in Zr-2.5wt% Nb pressure tubes in the early 1970's, extensive research has been conducted in this area. In general, DHC has been accepted as a repeating process that involves stress-induced hydrogen diffusion, hydride precipitation and hydride fracturing [40, 84]. The process usually begins at the tip of preexisting cracks in the alloys that act as stress raisers. Usually, the stress intensity factor, K_I , is used to characterize the stressed state of the crack tip. The threshold value for the initiation of DHC, K_{IH} , is a key issue for reactor operators and licensors.

K_{IH} is important, because it defines the stress levels for an assumed or measured pressure tube flaw size at which the pressure tubes may be operated without concern for leakage for their life time. CANDU designers and researchers are seeking pressure tube alloys with a K_{IH} higher than $10 \text{ MPa}\sqrt{\text{m}}$ through improved alloys or processing. Whether this is a realizable goal and how it may be achieved are still unknown due to a lack of knowledge about K_{IH} . This lack of understanding is manifested in the following two

aspects.

(1) The definition and method of determination of the K_{IH} parameter are still not uniquely defined.

Various techniques are used experimentally and the results of those different techniques are usually used to define the parameter. K_{IH} has been related to the three-stages that the DHC velocity curve exhibits with variation of the stress intensity factor [43, 84]. When the applied K_I is within a certain range, the DHC velocity remains almost constant - this forms stage II (the plateau) of the curve. At very high K_I , the velocity increases rapidly at the onset of fast fracture (stage III). When the applied K_I is below a certain value, the DHC velocity drops drastically and vanishes (stage I). The threshold value of K_I is taken as K_{IH} . However, as will become clear in this work, the actual events leading to cessation have not been studied in detail nor have the effects of some important experimental parameters been evaluated. Neither has the transition from stage I to stage II been satisfactorily explained.

Experimentally, the definition of K_{IH} is imprecise. In measuring K_{IH} , usually a decreasing load method is adopted, but a rising method is also used. In the decreasing method K_I is decreased in small steps until, at a certain level, there is no cracking detected during a certain significant test time. This K_I is then taken as K_{IH} . Acoustic emission (AE) and electrical potential drop (PD) have long been the main two techniques that are used for detecting the cracking events or measuring the crack length increments in the specimen [89]. AE signals are generally considered to be related to the fracture of hydrides [90, 91] which are formed at the crack tip during DHC, and thus indicate the cracking events. PD signals,

which are obtained by measuring the voltage across the crack with constant current, reflect the crack length increment. However, the resolution of the PD technique is limited and it may be difficult to decide when DHC has completely stopped. Usually the waiting period is arbitrarily set without a well-defined rationale. This may result in a higher measured K_{IH} for a zirconium alloy in which DHC velocity is lower, although in fact the K_{IH} may be very close for those alloys. The AE technique, although more sensitive, can sometimes give signals that are difficult to correlate to the cracking events. Therefore, sometimes one gets AE signals but no increase in PD signals during the experiment. AE has also been shown to be sensitive to temperature [89].

(2) The micromechanism of K_{IH} is not well understood.

Very little detailed characterization of the conditions existing at the crack tip when a K_{IH} condition has been reached has been published. Several different models have been proposed to account for the critical conditions for hydride fracture. They are the critical stress model [55, 92], the energy balance model [56, 93], and the combined critical stress-and-strain model [57, 83].

The critical stress model [55, 92] represents the first attempt to theoretically model the critical conditions at the crack tip when K_{IH} is reached. In this model, it is assumed that hydride will fracture when a critical tensile stress is reached. This model accounts for the dependency of K_{IH} on temperature quite successfully, but has some limitations in predicting K_{IH} when compared with the experimental data [55]. More recent work [57, 83] takes into account the effect of strain in considering the fracture of hydrides. Some previous experimental work on the criteria for hydride fracture suggested that plastic deformation

might be a prerequisite for hydride fracture [94]. But in general it seems that we still lack direct experimental evidence to prove whether hydride fracture is controlled by a critical stress or strain or both. In this work, based on some experimental observations, the authors would like to suggest that, at least in considering the K_{IH} issue, plastic deformation and fracture of the ductile matrix may need to be considered. This is because, when K_{IH} is considered, the region at the crack tip that is fractured contains both hydrides and matrix ligaments. The physical basis will be elaborated in later sections.

Zheng *et al.* [56, 93] assume that the stress acting on the hydrides at the crack tip is always sufficient for fracture, and invoke the thermodynamic argument that free energy must decrease during any spontaneous event. Then the energy balance condition becomes the necessary and sufficient condition for the fracture of hydrides. By considering the energy required to form a plastic zone at the crack tip, their model is capable of explaining why the hydride cluster formed at the crack tip needs to grow to a certain length before it fractures. However, the role and effect of stress are not clear in the model. Also the variation of the energy necessary to form the fracture surface, G_c , is seen as a constant rather than a variable and the micromechanism for hydride fracture is not provided.

4.1.2. The Objectives Of This Work

This work aims at a better understanding of K_{IH} in the above two aspects. The detailed formation and fracture of individual hydride clusters at the crack tip close to K_{IH} is experimentally studied for the first time. The results of this work provide an unambiguous

picture of the cracking/non-cracking of each individual hydride cluster at the crack tip. A new phenomenon for crack initiation, the R-curve, is proposed for the first time. Based on these results, K_{IH} is more carefully defined both theoretically and from the perspective of experimental measurement.

Based on the study of the critical hydride cluster length at different applied K_I , the stages I and II behavior of DHC velocity is explained. The specific energy required to create the fracture surface is estimated from the experimentally measured critical hydride cluster length at different K_I , and is found to increase with applied K_I .

Based on the experimental observation of hydride cluster fracture when close to K_{IH} , a hydride-fracture-micromechanism that incorporates the effect of both stress and energy is proposed. This model is for the case of partial fracture initiating inside the hydride cluster. For this case, the new model reconciles the contradiction between the critical stress model and the energy balance model.

In this work, a modified experimental method has been used which enables the hydride clusters formed and fractured during DHC to be observed and studied one by one. In this modified method, the specimens were fatigued between consecutive experiments, so that the hydride clusters in each DHC experiment were separated.

4.2. EXPERIMENTAL

4.2.1. Materials

The Zr-2.5wt% Nb alloys used in this work were provided by the Chalk River Laboratory (CRL) of the Atomic Energy of Canada Ltd. (AECL). The "as-received" alloys were in the form of a section of pressure tube about 600 mm long. Three batches of Zr-2.5wt% Nb alloys that arrived separately were used in this work. The compositions of the three batches of alloys were basically the same as listed in Table 4.1. The microstructures of these Zr-2.5wt% Nb alloys mainly consisted of α and β phases in the proportion 92% to 8%.

Table 4.1. Composition of the Zr-2.5wt% Nb alloys used in this work

	Zr	Nb	Sn	Fe	Cr	Ni	Mo	O ($\mu\text{g/g}$)	H ($\mu\text{g/g}$)
Wt %	balance	2.6	0.0025	0.05	0.01	0.0035	0.0025	1200	5

4.2.2. Specimen Preparation

A section about 50 mm long was first cut from the pressure tube. The ring-like section was then sawed open and flattened. After flattening, the alloy was cut into desirably sized pieces - usually just big enough to make two tapered double cantilever beam specimens (constant- K_I specimen). The alloy pieces were then annealed at 400°C for 24 hours to relieve the residual stress from the flattening process.

Before electrolytically hydriding the alloy, the oxidation layer on the alloy surface was removed by grinding and the surface conditioned by sand blasting. The aqueous electrolyte used was 0.5% by volume H_2SO_4 . After hydriding, the alloy piece was diffusion annealed for 48 hours at $400^\circ C$ to obtain a nearly uniform hydrogen level of $165 \mu g/g$ in the specimens. The alloy piece was then ground again to remove any remaining hydride layer on the surface.

Tapered double cantilever beam specimens, which give a constant stress intensity factor K_I when crack length a is between 8 - 19.3 mm, were used. The specimens were precisely machined using the electrical discharge machining (EDM) method at Excel Wire Erosion, in Mississauga, Ontario. The specimens were cut so that the cracking was on the axial-radial plane. The dimensions of the specimen are as given in Figure 4.1 [95].

To obtain a sharp crack tip, the specimens were fatigue pre-cracked. The ΔK_I was decreased as soon as a crack had been observed at the side surfaces of the specimen with the aid of a magnifier (5 x). The maximum K_I used during the finishing stage of fatigue pre-cracking was about $2.0 \text{ MPa}\sqrt{m}$, and the total length of pre-crack was not less than 1.0 mm, which conforms to the ASTM standard for pre-cracking (ASTM E 1681-95).

4.2.3. Experimental Equipment

Two testing rigs were simultaneously used for the K_{IH} experiments in this work. Rig 1 was a Model TTS-25KN Tension/Compression Testing Machine, manufactured by Adelaide Testing Machines Inc., Toronto, Ontario. The loading was computer-controlled

through a step-motor. The load measurement had an accuracy of ± 1 kg, and the load control was set to have an accuracy of ± 1 kg. Both acoustic emission (AE) and electrical potential drop (PD) methods were used with this rig to monitor the onset and propagation of cracking in the specimen. Rig 2 used a lever with a mechanical advantage of 10 to 1 and dead weights for loading. Loading was manual on this rig. Only the AE technique was used with this rig to monitor cracking in the specimen.

For both rigs, an AE transducer was attached to the end of the loading rods. Those loading rods, made of mild steel, were machined as whole pieces except for the clevis, to achieve the minimum loss in AE signals. A dummy specimen, which was made of Zr-2.5wt% Nb alloy, neither pre-cracked nor hydrided, was used to test the noise level in AE signal collection. It was found that for the same type of experiment on this dummy specimen, no appreciable AE signals were detected. This means that when appreciable AE signals are read by the system, one has reason to believe that the signals come from the specimen.

For rig 1, a Hewlett Packard (HP) Analog Programmable DC Power Supply model 6542A was used as the source of a 10-ampere DC electrical current. Each time the current was turned on for only a few seconds, while the PD signal was collected. To eliminate the effect of current fluctuation on the voltage measurement, a current gage with a standard resistance was connected into the circuit in series. The PD signal was defined as the voltage measured on the specimen divided by the voltage on the current gage. The PD voltage signal wires were welded onto the specimen. For a typical experiment, PD could define the change in crack length with a resolution of about 6 μm .

For both rigs, Eurotherm model 818 digital programmable temperature controllers were used to control the temperature of the furnace.

4.2.4. K_{IH} Experiments

The temperature 150°C was chosen for the K_{IH} experiments, because at this temperature the effect of oxidation on both the fracture and specimen surfaces was not obvious. Before each experiment, the two side surfaces of the specimen were attack-polished [96] to obtain a mirrorlike surface. The specimen was installed in the testing rig and held in place with a small load, which gave a K_I of about 0.5 MPa \sqrt{m} . Then the temperature of the furnace was raised to the peak temperature of 210°C. The temperature was held there for 1 hour (2 hours for rig 2), and then decreased to the testing temperature 150°C at a rate of 1 - 2 degrees per minute. Then the selected K_I was applied to the specimen. The K_I was kept constant during each experiment. When the experiment was finished, the load was first removed and then the specimen was furnace cooled to room temperature. Between any two consecutive experiments, the specimen was fatigued to obtain a crack length increment of about 400 μm , so that the specimen started with a similarly conditioned crack tip for each experiment.

Four constant- K_I specimens, made of three batches of Zr-2.5wt% Nb alloys (referred to as batch 1, 2, and 3 respectively in the following), were used for the K_{IH} experiments in this work. The experiments are summarized in the following table:

Table 4.2. Summary of K_{IH} experiments in this work

Specimen 1 (Batch 1)		Specimen 2 (Batch 1)		Specimen 3 (Batch 2)		Specimen 4 (Batch 3)	
Rig 1 (AE & PD)		Rig 1 (AE & PD)		Rig 2 (AE)		Rig 2 (AE)	
No. of Experi.	K_I (MPa√m)	No. of Experi.	K_I (MPa√m)	No. of Experi.	K_I (MPa√m)	No. of Experi.	K_I (MPa√m)
A1	2.0	B1	5.9	C1	2.0	D1	7.1
A2	4.1	B2	6.7	C2	3.4	D2	5.6
A3	6.0	B3	9.0	C3	4.9		
		B4	7.0	C4	6.3		
		B5	5.0	C5	5.6		
				C6	6.0		
				C7	4.0		

4.2.5. Post-Testing Examinations

The polished specimen side surfaces were examined for crack tip advance and plastic deformation zones. If either was present, the surfaces were photographed using a Zeiss Ultraphot optical microscope. Then a layer of about 0.1 mm was ground off one side of the specimen. The other side of the specimen was never ground, so that the shape of the crack front at that side was preserved for future fractographic study. The specimen was then repolished on the ground side and etched to reveal the hydride cluster(s), if any, along the crack path.

Some of the specimens were also opened for fractography study of the fracture

surface after all the experiments were done, mainly to see the variation of crack length in the specimen thickness direction.

4.3. RESULTS

4.3.1. R-Curve Phenomena

The results of the K_{IH} experiments can be divided into three categories, according to the K_I and corresponding DHC behavior.

In the first category, when $K_I \geq 7.0 \text{ MPa}\sqrt{\text{m}}$, steady DHC was observed, and the cracking rate detected by AE and PD was almost linear with test time. Figure 4.2 gives the results of a typical experiment in this category. Figure 4.2(a) shows the AE and PD signals vs. test time curves, and one can see that both AE and PD signals increased linearly with test time. This means the applied K_I was sufficiently high to maintain a steady DHC in the specimen. Figure 4.2(b) is the corresponding optical photograph taken from a side surface of the specimen after the experiment. Plastic deformation zones about $40 \mu\text{m}$ long and a small crack advance on the specimen surface, about $2.3 \mu\text{m}$ long, can be seen in the photograph. After photographing Figure 4.2(b), a layer of about 0.1 mm thick was ground off this specimen surface, and the hydride clusters along the crack path were revealed by etching as shown in Figure 4.2(c). One can see the length of the first few hydride clusters is smaller than that of the later hydride clusters, a phenomenon that relates to the R-curve phenomenon and which will be further elaborated in section 4.3.2.

In the second category, when $5.9 \text{ MPa}\sqrt{\text{m}} \leq K_I < 7.0 \text{ MPa}\sqrt{\text{m}}$, DHC first occurred in the specimen by forming and fracturing one to several hydride clusters, and then stopped.

The occurrence and cessation of DHC in the specimen were determined by AE signals during the experiment, and confirmed later by examining the hydride clusters on one side of the specimen. Figure 4.3 gives typical results from an experiment in this category. In Figure 4.3(a), one sees that the cumulative AE signals first increased quickly, then gradually slowed and finally stopped. Small plastic deformation zones were observed on the side surfaces of the specimen as shown in Figure 4.3(b). However, one sees no crack length increment on the specimen surface, *i.e.* the surface matrix ligament was not broken although underneath the surface the crack front had advanced by forming and fracturing several hydride clusters. This phenomenon is very important in explaining the R-curve phenomenon and will be discussed later. Figure 4.3(c) shows the hydride clusters revealed after grinding and etching. One can see in Figure 4.3(c) that three hydride clusters had been fractured along the crack path, which resulted in a crack length increment of about $41.2 \mu\text{m}$ as measured from the photograph. The crack had stopped in front of a hydride cluster that had not fractured. This indicates that, under the applied K_I in this experiment, the crack front could only advance by approximately $41.2 \mu\text{m}$. Figure 4.3(d) is the SEM photograph showing the crack tip area of Figure 4.3(c) before etching. The unfractured hydride cluster mixed with some matrix ligaments can be clearly seen in the SEM using the backscattering mode.

In the third category, when $K_I < 5.9 \text{ MPa}\sqrt{\text{m}}$, either there was no hydride cluster observed at the crack tip (when $K_I \leq 4.1 \text{ MPa}\sqrt{\text{m}}$), or the hydride cluster observed at the crack tip was not fractured. Figure 4.4 gives the results from a typical experiment in this category. Figure 4.4(a) gives the typical AE signals vs. test time curve when AE signals

were detected during the experiment. One can see that the cumulative AE signals first increased quickly, then after making one or two small jumps, formed a plateau. The reasons that AE signals could be detected with no crack advance (hydride cluster fracture) will be discussed later. In this category, no plastic deformation zones were observed on either side of the specimen after the experiment. The side surfaces of the specimen were similar to that given in Figure 4.4(b), showing neither plastic deformation zones nor crack advance. The unfractured cluster of crack tip hydrides is exemplified in Figure 4.4(c).

Figure 4.5 gives the distance the crack front could advance vs. the applied K_I in all the experiments performed. When the applied $K_I < 5.9 \text{ MPa}\sqrt{\text{m}}$, the distance the crack tip could advance was zero, because either no crack tip hydride cluster was observed or the crack tip hydride cluster observed was not fractured. When the applied $K_I \geq 7.0 \text{ MPa}\sqrt{\text{m}}$, steady DHC was observed in the specimen, so the distance the crack front could advance was unlimited. When $5.9 \text{ MPa}\sqrt{\text{m}} \leq K_I < 7.0 \text{ MPa}\sqrt{\text{m}}$, DHC first occurred in the specimen and then stopped, so the distance the crack front could advance is neither zero nor unlimited. All these latter cases form the R-curve phenomenon, which is proposed here for the first time in relation to crack initiation in this alloy.

4.3.2. Length Of Hydride Clusters

Another important phenomenon observed in this work was that along the crack path, when more than one hydride cluster formed, the first cluster had the smallest length. The lengths of the hydride clusters increased for the first few hydride clusters, and then reached a

relatively stable length, as shown in Figure 4.2(c). Figure 4.6 gives the change in hydride cluster length along the crack path for all three experiments in the first category ($K_I \geq 7$ MPa \sqrt{m}) in section 4.3.1. The total number and average length of hydride clusters for these experiments are summarized in Table 4.3.

Table 4.3. Summary of the total number and average length of hydride clusters for the three experiments of the first category in section 4.3.1

	Specimen 2, $K_I = 7.0$ MPa \sqrt{m}	Specimen 2, $K_I = 9.0$ MPa \sqrt{m}	Specimen 4, $K_I = 7.1$ MPa \sqrt{m}
Length of first hydride cluster (μm)	11.1	7.5	11.1
Number of total hydride clusters	7	25	34
*Average length of hydride clusters (μm)	14.0	10.9	14.1

*In calculating the average, if the last cluster was unfractured, it was excluded from the calculation.

One sees that, for the two experiments with $K_I \approx 7.0$ MPa \sqrt{m} , the lengths of the first hydride cluster coincide. Despite the variation in hydride cluster length along the crack path as seen in Figure 4.6 and the total number of hydride clusters being quite different, the average lengths of hydride clusters for these two experiments also coincide. For the experiment with $K_I = 9.0$ MPa \sqrt{m} , both the length of the first hydride cluster and the average length of hydride clusters are smaller than those of the two experiments with $K_I \approx 7.0$ MPa \sqrt{m} .

4.3.3. Critical Length Of Hydride Cluster At Different Applied K_I

Figure 4.7 gives the hydride cluster lengths observed at different applied K_I . At low K_I (category 3), not more than single hydride clusters were observed at the crack tips. Those clusters were unfractured, and the cluster length was the maximum to which the cluster will grow for that K_I . At higher K_I (categories 1 and 2), more than one hydride cluster was observed. The length of the first cluster was taken as the critical length for fracture of the cluster. One sees that as K_I increases, the hydride cluster length first increases for low K_I and then reverses direction when K_I exceeds $6.0 \text{ MPa}\sqrt{\text{m}}$. The solid line in Figure 4.7 gives the critical length of the (first) hydride cluster that can be fractured at different applied K_I , and is drawn along the experimental data. The dotted line shows the maximum length to which the hydride cluster can grow. It fits the relation $L \propto K_I^2$, where L is the hydride cluster length, and is the closest fit (by eye) to the three experimental measurements in the figure. One experimental measurement is considered as possibly unrepresentative, and is not included when drawing the dotted line. For small K_I this length is insufficient for fracture. A more explicit relationship would require significantly more data.

4.3.4. Effect Of Stress Level And Triaxiality

Table 4.4 shows the details about AE, the existence of a cluster and its fracture for all the experiments done in this work.

Table 4.4. Summary of experimental observations

Experiment No.	Specimen No.	K_I (MPa \sqrt{m})	Detection of AE signals	Crack tip hydride cluster(s) observed	Crack tip hydride cluster fracture
A1	1	2.0	No	No	--
C1	3	2.0	No	No	--
C2	3	3.4	Yes	No	--
C7	3	4.0	No	No	--
A2	1	4.1	Yes	No	--
C3	3	4.9	No	Yes	No
B5	2	5.0	Yes	Yes	No
C5	3	5.6	Yes	Yes	No
D2	4	5.6	Yes	Yes	No
B1	2	5.9	Yes	Yes	Yes
A3	1	6.0	Yes	Yes	No
C6	3	6.0	Yes	Yes	No*
C4	3	6.3	Yes	Yes	Yes
B2	2	6.7	Yes	Yes	Yes
B4	2	7.0	Yes	Yes	Yes
D1	4	7.1	Yes	Yes	Yes
B3	2	9.0	Yes	Yes	Yes

* A fractured hydride cluster was observed when the specimen was ground to mid-thickness.

When $K_I \leq 4.1$ MPa \sqrt{m} , no hydride cluster was observed at the crack tip, even when the specimen was ground to mid-thickness. For the five experiments in this K_I range, AE signals were detected only in two experiments and were very small. For all experiments with 4.9 MPa $\sqrt{m} \leq K_I < 7.0$ MPa \sqrt{m} , if AE signals were observed, the cumulative AE

signals first increased quickly, then slowed down, and finally leveled off. No fractured hydride cluster at the crack tip was observed until K_I increased to about $6.0 \text{ MPa}\sqrt{\text{m}}$. In one case, experiment C6, when the specimen was ground off by 0.1 mm, only an unfractured hydride cluster was observed at the crack tip. When the specimen was subsequently ground from one side surface to its mid-thickness (from 3.5 mm to 1.8 mm), two hydride clusters were observed at the crack tip: one fractured and the other unfractured.

Figure 4.8 shows a partially fractured hydride cluster at a crack tip.

4.3.5. Fractography

Figure 4.9 shows the variation of crack length along the specimen thickness. Figure 4.9(a) gives the fracture surface of specimen 1 after the specimen had finished the K_{IH} experiments of this work and a few other experiments. The crack regions corresponding to the three K_{IH} experiments in this work are marked by arrows. For specimens that had undergone many polishing and etching procedures like this one, we found that the fracture surface was smeared as in Figure 4.9(a). This is probably because during the etching process, the etching solution leaked through the spacing between two cracked surfaces and spoiled the fracture surfaces. Figure 4.9(b) shows the fracture surface of a reference specimen that was identical to specimen 3 used in this work. This specimen had undergone three K_{IH} experiments and some other experiments but very little polishing and no etching. The crack regions corresponding to the three K_{IH} experiments are much more clearly defined on this fracture surface. From Figure 4.9, one

can see that

- (1) the crack front curves in general towards the cracking direction in the middle of the specimen;
- (2) the crack length varies to some degree, but not very much, along the specimen thickness direction for the K_{IH} experiments conducted in this work;
- (3) the crack length is slightly longer close to the middle of specimen thickness than close to the specimen side surfaces;
- (4) unbroken matrix ligaments can be seen close to the specimen side surfaces, especially in Figure 4.9(b), in which the fracture surface was not smeared by the etching solution. The thickness of the unbroken matrix ligaments is about 10-20 μm in the specimen thickness direction. This means that grinding 0.1 mm off the specimen side surface is enough to show the crack length "inside" of the specimen.

4.4. DISCUSSION

4.4.1. R-Curve Phenomena

In fracture mechanics, the R-curve is used to describe the change in a material's resistance to fracture with an increasing stress intensity factor. Usually the R-curve increases with K_I . The rising R-curve is usually explained based on the amount of shearing fracture that is observed on the fracture surface [97]. The shearing fracture results from the plane stress regions close to the side surfaces of the specimen. (In contrast, plane strain exists under the surface.) Shearing fracture is more ductile than the flat fracture that occurs in plane strain. Consequently, the shearing fracture requires more energy. When the specimen is loaded to fracture, the amount of shearing fracture on the fracture surface is found to increase with K_I , resulting in an increase in the energy required for fracture.

The "R-curve phenomenon" observed in this work can also be attributed to the plane stress effect near the surface. When K_I is low and the energy balance condition for fracture is not met, the hydride cluster at the crack tip is not fractured, therefore there is no crack front advance. When K_I is high enough to meet the energy balance condition, the first hydride cluster at the crack tip fractures. However, due to the plane stress effect, no hydrides will have precipitated close to the specimen surface, thus leaving a ductile matrix ligament that is not fractured at each side surface of the specimen. Thus, the crack front tunnels underneath the specimen surface over the length of the first hydride cluster.

Fracturing the second cluster will be more difficult than fracturing the first, because the crack tip opening is now restricted by the matrix ligament at both sides of the crack front. This causes the resistance to fracture to be higher at the new crack tip since it includes energy to deform or fracture these ductile ligaments. If the K_I is not high enough to fracture the second hydride cluster, then DHC will just stop here. If the K_I is sufficient, resulting in the fracture of the second hydride cluster (and further deformation and/or fracture of the ligaments), the tunneled length will increase. The fracturing of the third hydride cluster will be even more difficult because the resistance to fracture is increased by the longer ligaments and so on. This explanation is supported by the experimental observation that the hydride cluster length increased for the first few hydride clusters formed and fractured along the crack path. At the same time as the tunneling of the crack front occurs, the stress on the unfractured matrix ligament at the specimen surfaces also increases. The two matrix ligaments will be strained more severely, and slip will occur along the 45° maximum shear stress direction. This deformation results in the plastic deformation zones observed on the attack-polished specimen side surfaces. After the fracture of several hydride clusters, DHC will stop if the resistance to fracture increases so that K_I is not sufficient to fracture the next hydride cluster and deform or fracture the growing ligaments. This region of tunneling forms the rising R-curve, which in these experiments falls between $5.9 \text{ MPa}\sqrt{\text{m}}$ and $7.0 \text{ MPa}\sqrt{\text{m}}$. As the ligaments get longer and with sufficient K_I , the plastic strain for the matrix ligaments farthest behind the tunneled crack front exceeds the level the matrix can sustain. Now the matrix ligaments will start to fracture and the resistance-to-fracture will no longer increase. With reference to the R-curve phenomenon, this implies there is no further

increase in this curve. This was the case for the crack advance observed on the specimen surfaces shown in Figure 4.2(b). When this happens, DHC can continue indefinitely in the specimen, because the applied K_I is high enough to fracture both the hydride cluster and portions of the matrix ligament at the specimen surfaces. This was observed when $K_I \geq 7.0$ $\text{MPa}\sqrt{\text{m}}$.

Since the R-curve phenomenon is related to the plane stress effect, it is also related to the specimen thickness, as is the conventional R-curve in fracture mechanics. It is assumed that the thickness of the unfractured matrix ligament is comparable to the plastic zone size in plane stress. This is given by $r_p = \frac{1}{2\pi} \left(\frac{K_I}{\sigma_{ys}} \right)^2$, where r_p is the radius of the plastic zone, and σ_{ys} is the yield stress. The thickness of the unfractured matrix ligaments is thus constant for a given K_I , even when the specimen thickness changes. However, for tunneling in a thicker specimen, a smaller percentage of the load will rest upon the matrix ligaments since the load for a given K_I increases with thickness. Hence, the restraining effect decreases with increasing specimen thickness. By the same logic, as the specimen thickness decreases, the rising part of the R-curve will become larger. Thus, one may conclude that the experimental measurement of K_{IH} can be affected by the following two factors:

(1) The specimen thickness. According to this analysis, specimens with smaller thickness will give a larger rising part of the R-curve. Since there are no ligaments, the fracture of the first hydride cluster is not affected by the specimen thickness and the starting point of the rising part of the R-curve remains the same for specimens of different thickness. Thus, a

thinner specimen will give a higher R-curve, which results in a higher measured K_{IH} since it is taken as the point where the crack will not stop.

(2) The type of specimen. When a constant- K_I specimen is used, as in this work, the measured K_{IH} will be at the top of the R-curve, since for the constant- K_I specimen, K_I does not increase with crack length. For a compact toughness specimen, K_{IH} would occur at the point on the rising part of R-curve, where the K_I vs. crack length curve is tangent to the R-curve. Therefore, using constant- K_I specimens will result in a slightly higher K_{IH} .

If K_{IH} is to be considered as a property of the material, as is K_{IC} , then K_{IH} should be defined in a way that its measurement does not vary with the specimen thickness or the type of specimen used. Thus, K_{IH} should be defined as the starting point of the rising part of R-curve. Then, the physical meaning of K_{IH} is the minimum applied K_I that can fracture the first hydride cluster. It should be understood that if the specimen thickness were large enough, then DHC could continue indefinitely under this K_I .

4.4.2. Length Of Hydride Clusters

The average Vickers hardness values measured from the side surfaces of the four specimens are given in Table 4.5. From this hardness data, one knows that the Zr-2.5wt% Nb alloys used in this work have similar yield stresses. Based on this information and the cluster length data in Table 4.3, one may conclude that the hydride cluster length for DHC of "as-received" Zr-2.5wt% Nb alloys with similar yield stress is determined by the applied K_I . Since the specimens were fatigued between experiments, each experiment started with

an identical “fresh” crack tip. Probably that is why such good consistency was obtained in the lengths of the first clusters for the two experiments with $K_I \approx 7.0 \text{ MPa}\sqrt{\text{m}}$. It was observed that there was considerable variation in the length of hydride clusters along the crack path in Figure 4.6, but consistency in the average length of hydride clusters for the two experiments. Thus, one may conclude that hydride cluster length is related in a statistical sense to the applied K_I during the complicated process of DHC.

Table 4.5. Hardness of Zr-2.5wt% Nb alloys used in this work

	Specimen 1	Specimen 2	Specimen 3	Specimen 4
*Average hardness (HV10)	223	225	229	228

* The average was taken from six measurements, three on each side surface of the specimens.

The fact that the first hydride cluster had the shortest length indicates that the first hydride cluster was the easiest to fracture. Based on the discussion in section 4.4.1, it would have the lowest R value. Notice that for the three experiments given in Table 4.3, the length of the fractured hydride clusters increased for the first 3 - 4 hydride clusters only, and then stayed at the average level. This average hydride cluster length, although it increases as K_I decreases, is lower than the critical hydride cluster length (about $22 \mu\text{m}$) corresponding to K_{IH} , which is close to $6.0 \text{ MPa}\sqrt{\text{m}}$ according to this work. This suggests that the restrictive effect from the matrix ligament is limited to 3 or 4 hydride clusters and produces a maximum R effect of $1 \text{ MPa}\sqrt{\text{m}}$ (in terms of the increase in K_I required for fracture). Presumably 3 - 4 cluster lengths is the limit of tunneling for these experimental conditions.

4.4.3. Critical Length Of Hydride Cluster At Different Applied K_I

There are two concepts that interact here. One is that the growth of the hydride cluster is limited to some value, which increases as K_I increases. The second is that the propensity for the fracture of a hydride cluster increases as the hydride cluster gets longer. Both of these concepts are supported by the experimental evidence in this work.

To understand the limited growth of hydride cluster, it is necessary to apply the calculated results of Metzger *et al.* [98]. They showed using finite element analysis that the expansion of the hydrides leads to a reduction in the stresses at the crack tip. Because these stresses are the driving force for hydrogen diffusion, hydride growth can be a self-limiting process, which will cease when the stresses drop below the level required for further growth. This cessation will not occur of course if the hydride growth is truncated by a fracture event, which restarts the growth at a new crack tip. The stress level at which hydride growth will stop has not been determined definitively. It has been conjectured that it might be close to the stress level of 400 MPa that is required for a reoriented hydride to form [99]. The other important result from Metzger *et al.*'s work is that the stress drop per increment of hydride growth becomes increasingly more significant as the applied stress intensity factor decreases. Thus, the effect is very important in the region of K_{IH} .

The results in Figure 4.7 might then be explained as follows. The experiments show that the length of the hydride cluster at fracture increases very quickly as the applied K_I drops below about $7 \text{ MPa}\sqrt{\text{m}}$. This length is the critical length for fracture. This effect is

described by the solid line in the figure. From our observation of the length of the unfractured hydride cluster at low K_I , the length of the hydride cluster is growth limited at the values along the dotted line in Figure 4.7. Fracture can only begin to occur when the curve for the length of maximum growth and the curve for the necessary length for fracture intersect. This explains the threshold phenomenon for delayed hydride cracking.

The critical hydride cluster length we experimentally measured as given by the solid line in Figure 4.7 shows a similar dependency on K_I as that given by numerical [56] and theoretical [100] analysis.

4.4.4. The Energy Required To Create The Fracture Surface Of The Hydride Cluster

The energy required to fracture the hydride cluster consists of two parts. The first part is the energy to break the matrix and hydride atomic bonds along the fracture surface and the plastic deformation energy related to the required deformation of ductile matrix ligaments on the fracture surface. The second part is the energy to create the plastic deformation zone at the new crack tip. In the literature of fracture mechanics [101], both parts constitutes the “fracture energy” that is distinguished from the “surface energy”. For brittle materials such as amorphous glasses, the difference between the “fracture energy” and the “surface energy” is insignificant. But for metals and polymers, the “fracture energy” consists of the plastic deformation energy, γ_p , and the “surface energy”, γ_s , and this is much larger than the “surface energy” γ_s alone. When applied to the

fracture of a hydride cluster in DHC, the plastic deformation energy, γ_p , should include the energy of both the plastic deformation of the matrix ligaments and the plastic deformation at the new crack tip. Zheng *et al.* [56] called this first part the “surface energy”, and it was denoted as G_c . This usage is different from that in the literature. In this work, in order to conform to the literature, we will call the first part the “energy required to create the fracture surface”, but denote it as G_c .

Based on the numerical analysis, Zheng *et al.* first calculated the elasto-plastic energy release rate with respect to the length of crack extension. Then they approximated the calculated curve by a closed formula by using curve fitting. The closed formula they used was a function of (L/r_p) , where L is the length of crack extension and r_p the plastic deformation zone size in plane strain conditions. By using this closed formula, they were able to obtain the Equation (8) in their paper that can be rewritten as:

$$G_c = \frac{1.556L_c}{1.556L_c + K_I^2 / (6\pi\sigma_{ys}^2)} \frac{1 - \nu^2}{E} K_I^2, \quad (4.1)$$

where G_c is defined above, L_c is the critical hydride cluster length, and K_I is the applied stress intensity factor. From [56], Young’s modulus $E = 81.541 \times 10^3$ MPa, and Poisson’s ratio $\nu = 0.329$. We measured the yield stress, σ_{ys} , of the Zr-2.5wt% Nb alloy (batch 1) to be 630 MPa at 150°C. From Equation (4.1) the G_c ’s for the different experiments in this work were determined as shown in the following table:

Table 4.6. The specific energy required to create the fracture surface
(calculated from the experimental results in this work)

Experiment No.	B1	C4	B2	B4	D1	B3
K_{IH} (MPa \sqrt{m})	5.9	6.3	6.7	7.0	7.1	9.0
$G_c(I)^*$ (J/m 2)	336	364	364	392	393	460
$G_c(\text{Ave.})^{**}$ (J/m 2)	-	-	-	412	417	541

* the "I" denotes the G_c calculated from the first hydride cluster that was formed and fractured;

** the "Ave." denotes the G_c calculated from the average hydride cluster length, if applicable.

From the above table, one sees that the *specific* "energy required to create the fracture surface" increased with the applied K_I . We know the energy required to create the fracture surface is determined by the relative portions of matrix ligaments and hydrides in the hydride cluster. When the hydrides get denser, this energy term will decrease. Therefore, the results in Table 4.6 indicate that the densities of hydrides in the cluster are higher for lower K_I and longer clusters. At lower K_I , it took a longer time for the hydride cluster to grow to the critical length for fracture, and thus provided more time for hydrides to precipitate. Therefore, one sees that during the growth of the hydride cluster, this specific energy required to create the fracture surface is decreasing. Consequently, the critical cluster length for fracture is also dropping. Figure 4.10 shows the calculated critical cluster length vs. applied K_I curves when the specific energy required to create the fracture surface is constant, based on equation (4.1). The thick solid line is the best-fit line (by eyes) to our experimental results. The curve shows that

the specific energy required to create the fracture surface decreases as K_I decreases. This is an extension of the original theory as presented by Zheng *et al.* and emphasizes the contribution of decreasing G_c in modifying the critical length for hydride cluster fracture. Thus, it is not only the decreasing contribution of the plastic energy at the crack tip for longer clusters, but also the fact that the energy to create the fracture surface decreases with the growth as well.

4.4.5. Stage I/Stage II DHC Velocity

The arguments in section 4.4.3 can be extended to explain the stage I and stage II velocity phenomenon for DHC. Time-dependent growth is considered in Figure 4.11. The dotted-lines are a series of lines that meet the relation $L \propto K_I^2$, where L is the hydride cluster length. The dotted line on the top is the same as the one in Figure 4.7, and gives the maximum length to which the hydride cluster can grow for different applied K_I , corresponding to infinitely long diffusion times t_{gl} (here “gl” means “growth limit”). The other dotted lines correspond to hydride cluster lengths at the same K_I 's for smaller diffusion times $t_{gl} > t_1 > t_2 > t_3$, *etc.* All dotted lines intersect the critical hydride cluster length for fracture line at l_{gl} , l_1 , l_2 , and l_3 *etc.* The DHC velocities at different applied K_I can be calculated as $\frac{l_{gl}}{t_{gl}}$, $\frac{l_1}{t_1}$, $\frac{l_2}{t_2}$, and $\frac{l_3}{t_3}$ *etc.* Thus we see that the boundary between stages I and

II of the DHC velocity vs. K_I is decided by the turning point of the solid critical hydride cluster length curve. On the left side of this turning point, a small change in K_I results in

relatively small change in l_i , but relatively large change in diffusion time t_i , since here the diffusion time t_i ranges from several hours to infinity. This results in a significant change in DHC velocity, and thus corresponds to stage I. On the right side of the turning point, the situation is just the opposite. Both the solid line and the dotted lines are almost all parallel to the K_I axis, and thus the resulting DHC velocities are relatively insensitive to the change of K_I . This is the situation in stage II.

4.4.6. Absence Of Hydride Cluster At Low K_I

The reasons that hydride clusters were not observed at the crack tips when $K_I \leq 4.1$ $\text{MPa}\sqrt{\text{m}}$ are unknown. It is possible that there were experimental difficulties involving compressive zones, which could be associated with reducing the stress intensity factor during the fatigue pre-cracking. Another possible explanation is that when the plastic zone or the effective-stress zone decreases to a certain size, *e.g.* the grain size, the mechanisms for hydrogen diffusion or hydride precipitation are altered, so that no hydride cluster can form.

4.4.7. Acoustic Emission Without Striation Formation And Partially Fractured Hydride Cluster

In Table 4.4, one sees that when $4.9 \text{ MPa}\sqrt{\text{m}} \leq K_I \leq 6.0 \text{ MPa}\sqrt{\text{m}}$, a hydride cluster was observed at the crack tip, but for six of the seven experiments in this category, the hydride cluster was not fractured. However, for the seven experiments, AE signals were

detected in all but one experiment. It seems likely that these AE signals came from the fracture of hydrides in the seemingly unfractured hydride cluster at the crack tip.

This hypothesis is supported by another important phenomenon observed in this work. It was seen that the fracture of hydride cluster might start in the middle of the cluster, rather than from the cluster end that is closer to the crack tip as suggested by the “hinged-hydride” model [43]. This is evident from Figure 4.8 in which there are cracks along and inside the hydrides, but the end of hydride cluster which was closer to the crack tip has not yet fractured. For this local fracture without crack advance, the following observations are pertinent.

- (1) Although DHC is in general a step-wise cracking feature, the cracking process of a hydride cluster when hydrides have formed and/or are forming might also be a slow one as well as a sudden one, because otherwise situations as in Figure 4.8 could not be observed;
- (2) When some hydrides in the hydride cluster have cracked, the loading at the crack tip could still be balanced by both the remaining material in the hydride cluster and the hydride cluster end closer to the crack tip, since no new hydride cluster is forming.
- (3) Cracks seem to initiate somewhere in the mid-length of the hydride cluster, *e.g.* in the hydrides, and then propagate towards the two ends.

This behavior is in contrast to the observations of Shek *et al.* [76] who experimented with some special Zr-2.5wt% Nb material at higher temperatures. They observed that large DHC jumps (as indicated by changes in potential drop signals and by metallography) were exactly correlated with the acoustic emissions indicating that the entire region of the

striation was fracturing simultaneously. It appears that both kinds of fracture events can occur in DHC.

Thus, one sees that the K_{IH} issue is not simply the fracture of hydrides. The fracture of hydrides may need to be distinguished from the fracture of the whole hydride cluster. The latter constitutes a complete step in DHC and it is this fracture on which the definition of K_{IH} is based. A hydride cluster consists of hydrides mixed with ductile matrix ligaments. It is apparent that hydrides in the hydride cluster can sometimes fracture before the cluster itself is fractured. In the work of Shi *et al.* [55], modeling of K_{IH} was based on the fracture of pure hydrides. Therefore, as they observed themselves, the above reason may account for the difference between their theoretically predicted K_{IH} and the experimentally measured K_{IH} , which is based on the fracture of the hydride cluster. The above observation, if being general, may also help resolve another controversial point, as first raised by Zheng *et al.* [56], that if hydride fracture were controlled by a critical stress, hydrides should fracture as soon as they were formed. Their point was that if hydrides fracture as soon as they form, they would not be able to grow to a certain length. Based on Figure 4.8, we now know that even if some hydrides have fractured, the crack tip may still effectively remain in its original place held by the restrictions from the remaining material in the hydride cluster. Then the stress peak on the hydride cluster still exists and hydrides can continue to precipitate. We may imagine that the remaining matrix ligaments in the hydride cluster and the matrix at the cluster end closer to the crack tip are like mini-tensile specimens. When these mini-tensile specimens are stretched to fracture, they show a stress-strain curve similar to that of the matrix alloy. The area underneath the curve is the energy required to break those matrix

ligaments, and to make one step - a striation, in DHC. In addition, when these matrix ligaments and the cluster end are close to fracture, a plastic zone will form at the new crack tip and this requires energy. All this energy is provided by the mechanical work done by the external load less any increase in the elastic stored-energy in the specimen. In the balance of this section, this energy is the energy available for cracking. According to Zheng *et al.* [56], this energy is not sufficient to fulfill the crack length increment unless the increment is long enough. This energy term exerts a separating force along the length of the hydride cluster. This force can be replaced by an average force (referred to as the crack-driving force in the balance of this section) exerted in the middle of the cluster. This force is balanced by the contiguous stresses in the hydride cluster (referred to as the balancing force in the following discussion) at the crack tip. The source of this balancing force is the atomic bonds of matrix material and the hydrides along the cracking plane in the hydride cluster. When hydrides form, because hydrides have less ductility than the matrix, hydrides will fracture before the matrix. Then as hydrides form and fracture in the cluster, more load will rest upon the unfractured matrix ligaments, and the matrix will be stretched more severely. However, as soon as this happens, the energy available for cracking is relaxed to a certain extent since local tensile deformation leads to local unloading. Therefore, the crack-driving force decreases, and the balancing force may increase due to strain hardening. As the hydride cluster continues to grow in length, the energy available for cracking increases (as shown by Zheng *et al.*), resulting in an increase in the crack-driving force. Thus more new hydrides crack and the stretching increases. Then the crack-driving and the balancing forces reach equilibrium again, and the process repeats through further hydride growth. In this way, the

total energy required to make a DHC striation is being gradually fulfilled by the release/increase of the energy available for cracking and the increase in hydride cluster length. When the hydride cluster length becomes long enough the energy available for cracking becomes sufficient to make a DHC striation. Then the crack-driving force exceeds the balancing force, and the remaining matrix ligaments in the hydride cluster and the cluster end closer to the crack tip are finally torn apart.

4.4.8. Measurement Of Hydride Cluster Length

In this work, the lengths of hydride clusters were measured at a depth of about 0.1 mm from one of the specimen side surfaces. This may raise questions as to whether a hydride cluster length so measured can really represent the average hydride cluster length across the specimen thickness.

Measuring hydride cluster lengths at different depths from one specimen side surface and then taking an average will not help solve this problem. This is because, as one can see in Figure 4.9(b), the crack length sometimes was almost uniform within nearly half the specimen thickness (as on the right side), but was still different from that in the other half of the specimen thickness. The best way is probably to measure the hydride cluster lengths at 0.1 mm depth from both side surfaces as well as in the middle of the specimen thickness, and then take an average. But this will present some experimental difficulties when only limited number of specimens are available for doing the experiments.

However, the hydride cluster lengths we measured may still be valid for the thesis of

this work for the following reasons:

- (1) the hydride cluster lengths measured in this work are only used for relative comparison purposes, to show the trend the hydride cluster length varies with applied K_I . The same applies to section 4.4.4, where the critical hydride cluster lengths were substituted into equation (4.1) to calculate the specific energy required to create a fracture surface at different K_I 's;
- (2) the reasons the crack length in the middle of the specimen thickness is longer are likely because there are more hydride clusters formed and fractured there, as in experiment C6 in which only one hydride cluster was found at 0.1 mm from one specimen surface but two were found at the middle of the specimen thickness. This means that the variation in hydride cluster length may not be as much as the variation of the crack length as seen on the fracture surface;
- (3) as one can see in Figures 4.8(a) and (b), for small applied K_I (*i.e.* $K_I \leq 7.0 \text{ MPa}\sqrt{\text{m}}$, the K_I range in which we did most of the experiments), the variation of crack length along the specimen thickness is small.

4.5. CONCLUSIONS

- (1) A modified K_{IH} experimental method has been developed in this work, by which individual hydride clusters formed and fractured at the crack tip can be observed and studied one by one.
- (2) A total of seventeen K_{IH} experiments which covered the K_I range from 2.0 - 9.0 MPa \sqrt{m} were performed on four constant- K_I specimens of three Zr-2.5wt% Nb batches with similar yield stress. The experimental results can be divided into three categories according to the applied K_I and corresponding DHC behavior:
 - (i) when $K_I \leq 6.0$ MPa \sqrt{m} , no crack front advance was observed in the specimen. For these experiments, either no hydride cluster was observed at the crack tip or the crack tip hydride cluster observed was not fractured;
 - (ii) when 6.0 MPa $\sqrt{m} < K_I < 7.0$ MPa \sqrt{m} , the crack front first advanced by forming and fracturing one to several hydride clusters at the crack tip, and then came to a stop; and
 - (iii) when $K_I \geq 7.0$ MPa \sqrt{m} , steady DHC was observed in the specimen, and the crack front could advance indefinitely with test time.
- (3) The length of hydride cluster was found to increase for the first few hydride clusters along the crack path, and then stay at a relatively stable level.
- (4) Based on the above phenomena, a new concept of R-curve has been proposed to describe Zr-2.5wt% Nb alloys' resistance to DHC. Using the R-curve concept, K_{IH} is defined.
- (5) The critical length of the hydride cluster that could be fractured at the crack tip at

different applied K_I was experimentally measured, and was found to increase drastically when the applied K_I drops below $7.0 \text{ MPa}\sqrt{\text{m}}$. The position of this transition part is found to be related to the position of the turning point between stages I and II on the DHC velocity vs. K_I curve. The critical hydride cluster length curve can be used to account for the stages I and II behavior in the DHC velocity vs. K_I curve.

(6) The specific energy required to create the fracture surface in DHC is estimated from the critical hydride cluster length at different K_I measured in this work, by using the equation from some previous theoretical work of Zheng *et al.* [56]. This fracture energy decreases with increasing hydride cluster length and this change is part of the K_{IH} phenomenon.

(7) Based on experimental observations, it is suggested that fracture of hydrides in a hydride cluster should be distinguished from the fracture of the hydride cluster itself. The former can happen before the latter, which constitutes a striation in DHC. A qualitative micromechanical model which incorporates the effect of both stress and energy has been proposed to explain the details of the K_{IH} mechanism and some AE phenomena.

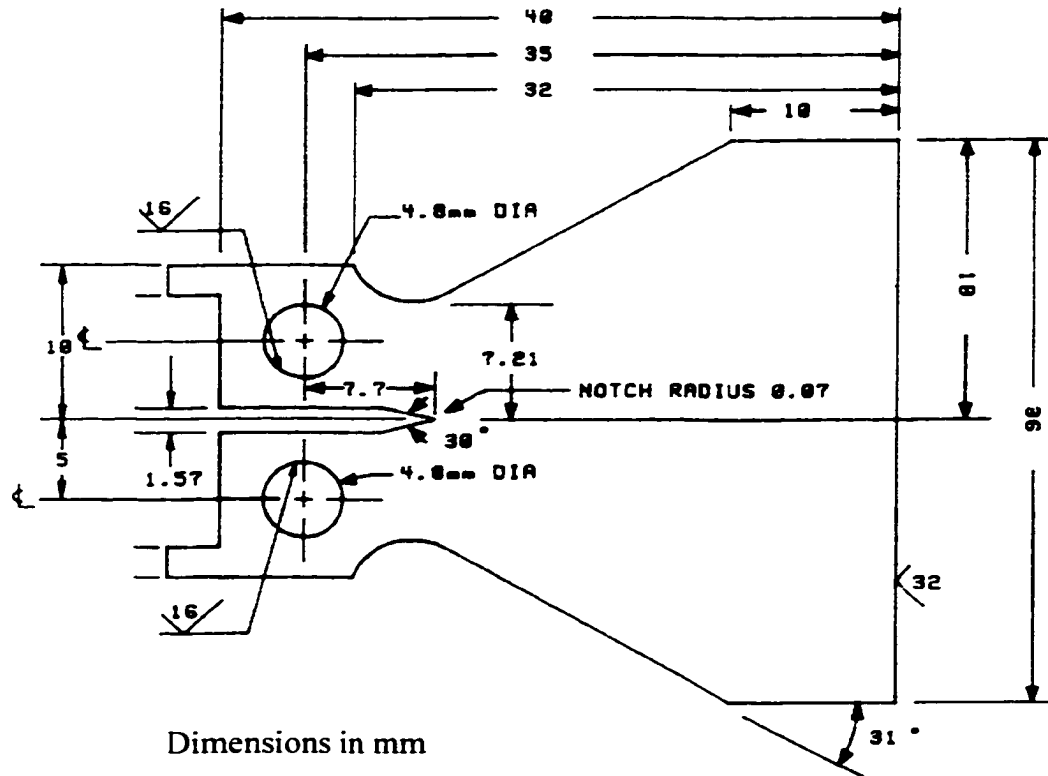
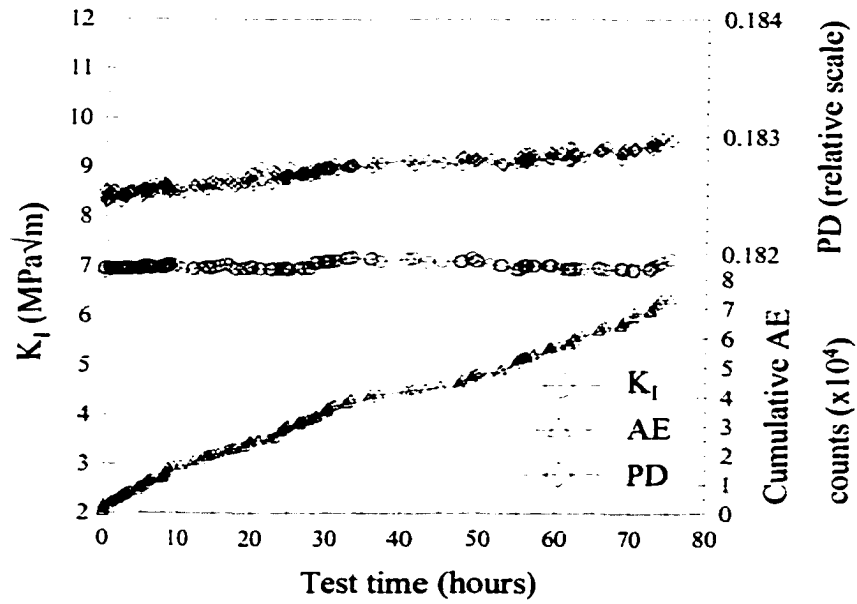


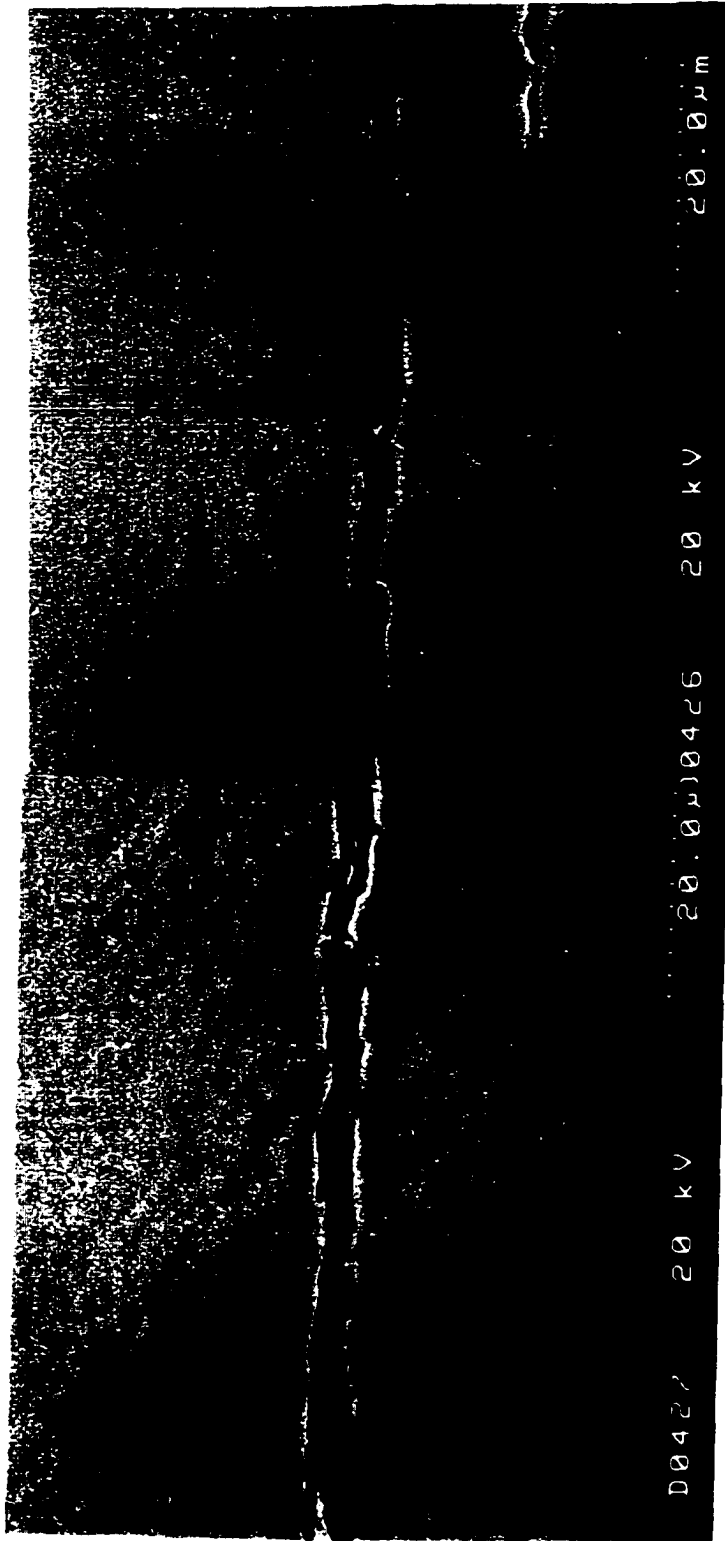
Figure 4.1. The dimensions of a double cantilever beam (constant- K_I) specimen (Shek and Graham [95]).



(a)

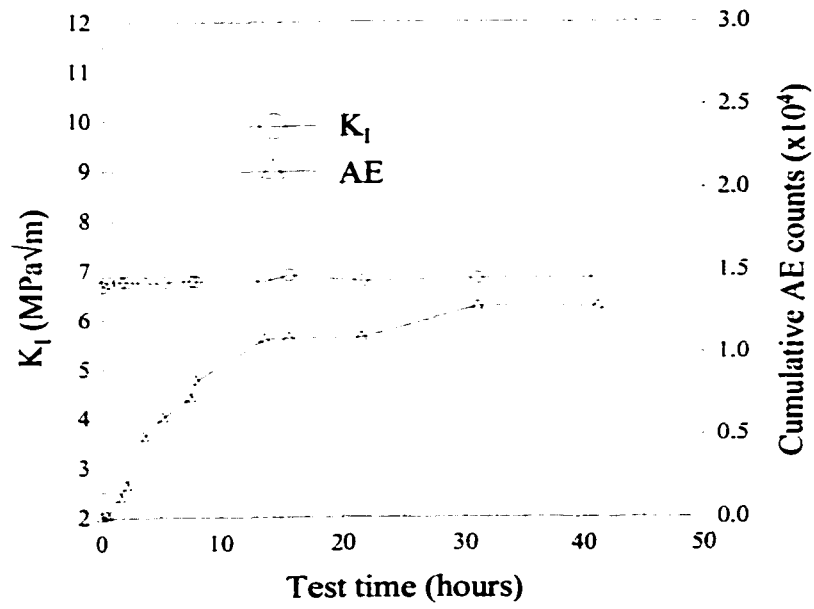


(b)

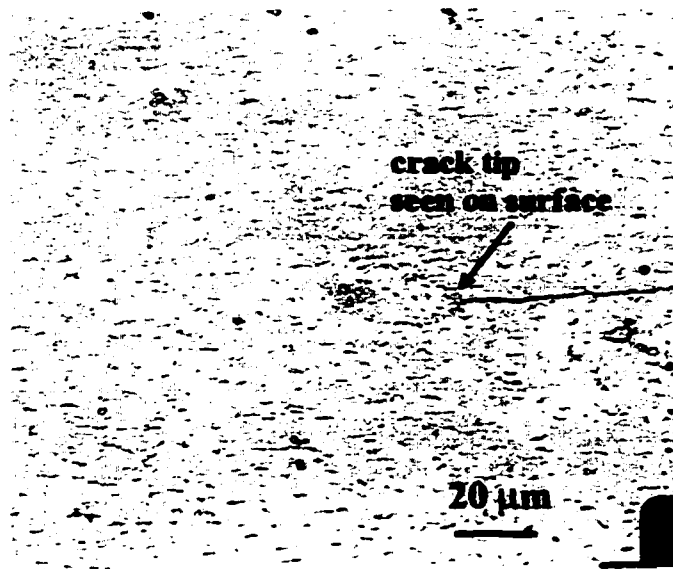


(c)

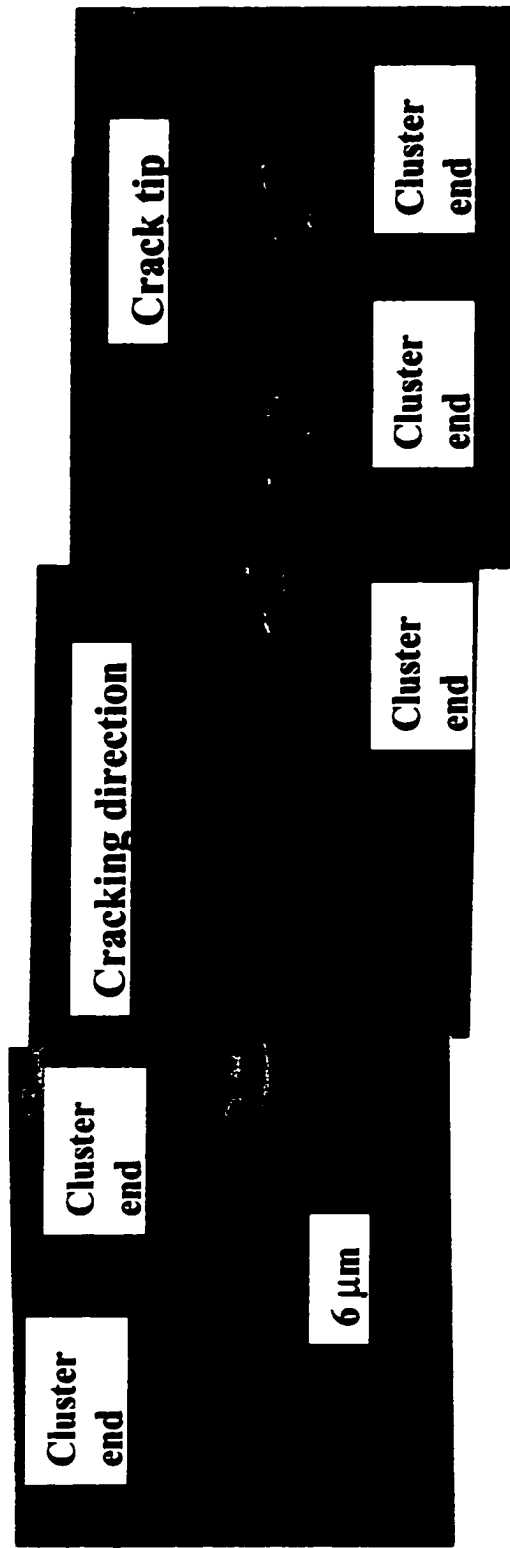
Figure 4.2. Experimental results when $K_I = 7.0 \text{ MPa}\sqrt{\text{m}}$. (a) AE and PD signals vs. test time; (b) Plastic deformation zones at crack tip (optical); (c) Hydride clusters along crack path (SEM).



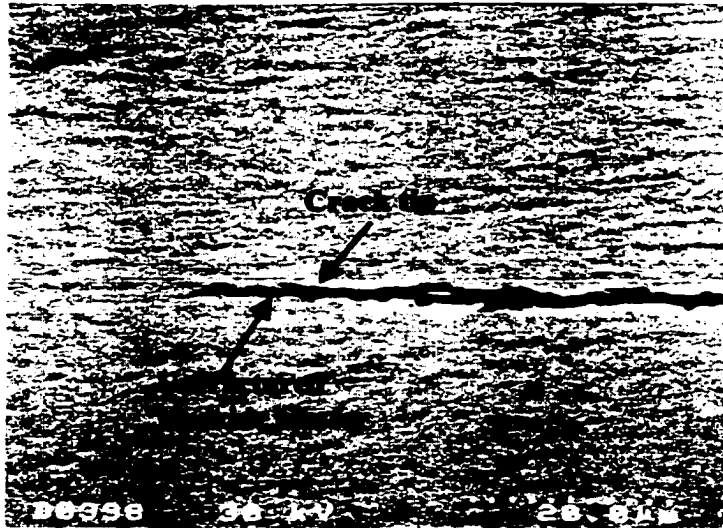
(a)



(b)

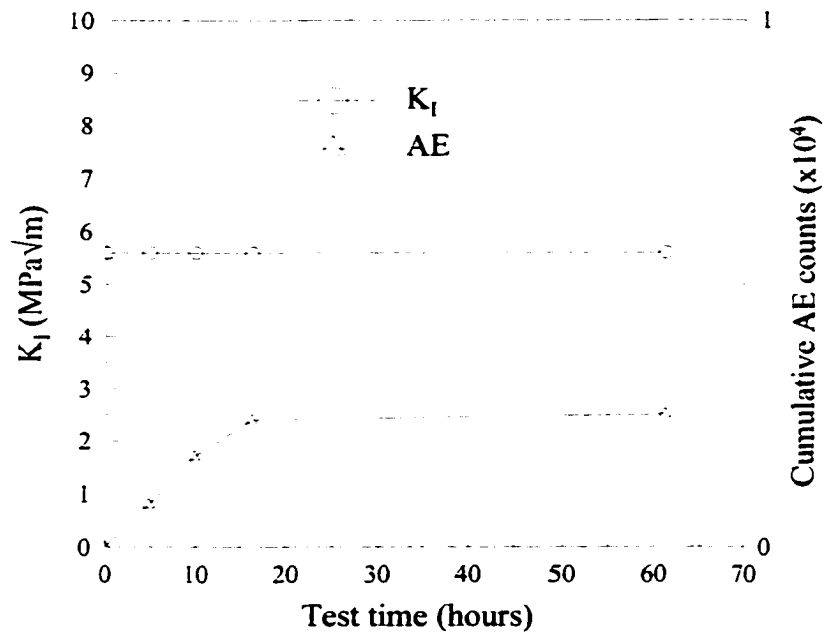


(c)

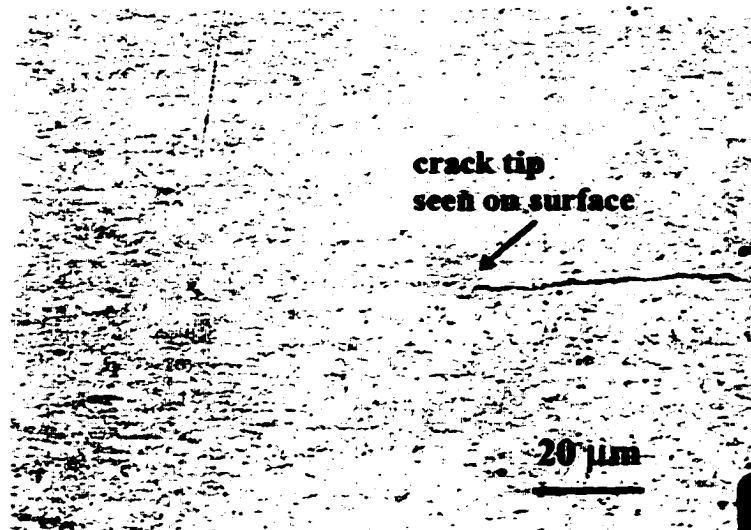


(d)

Figure 4.3. Experimental results when $K_I = 6.7 \text{ MPa}\sqrt{\text{m}}$. (a) AE signals vs. test time; (b) Plastic deformation zones at crack tip (optical); (c) Hydride clusters along crack path (SEM); (d) Backscattered SEM image of hydrides at crack tip.



(a)



(b)



(c)

Figure 4.4. Experimental results when $K_I = 5.6 \text{ MPa}\sqrt{\text{m}}$. (a) AE signals vs. test time; (b) No plastic deformation zones at crack tip (optical); (c) An unfractured hydride cluster at crack tip (SEM).

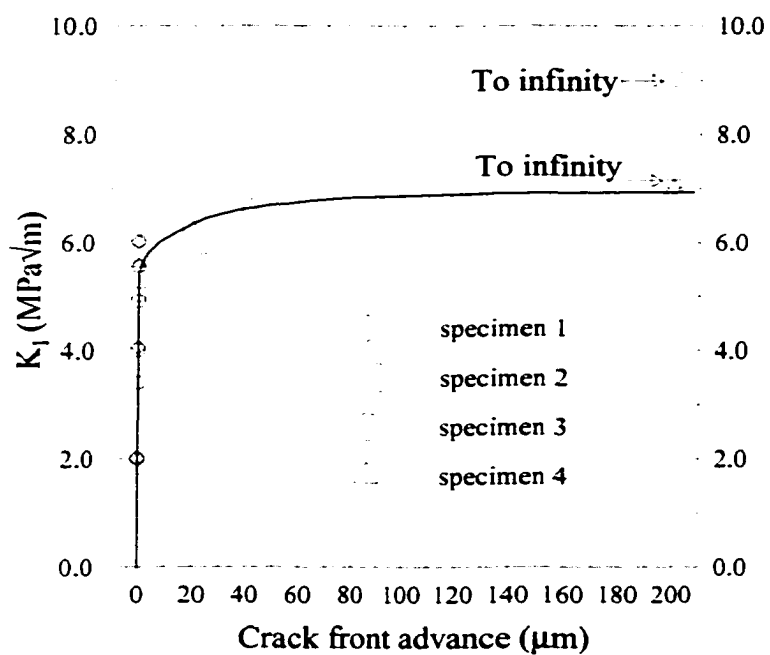


Figure 4.5. Distance of crack advance at different K_I .

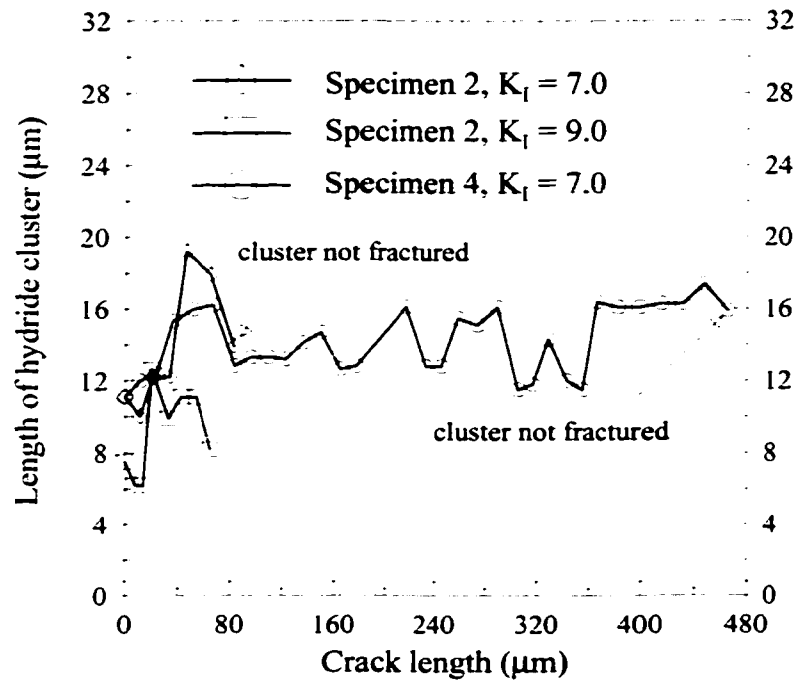


Figure 4.6. Length of hydride clusters along crack path.

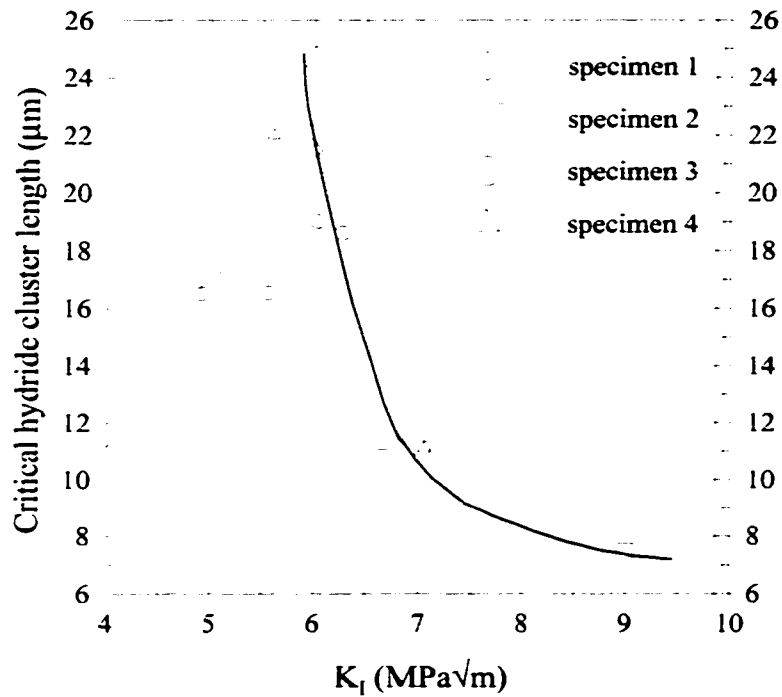


Figure 4.7. Critical hydride cluster length at different K_I . The solid line is obtained by drawing along the experimental data by eye; and the dotted line is obtained by fitting the line that has the relation $L \propto K_I^2$ to the three experimental measurements by eye. One measurement is considered as possibly unrepresentative and is not included in fitting the dotted line.

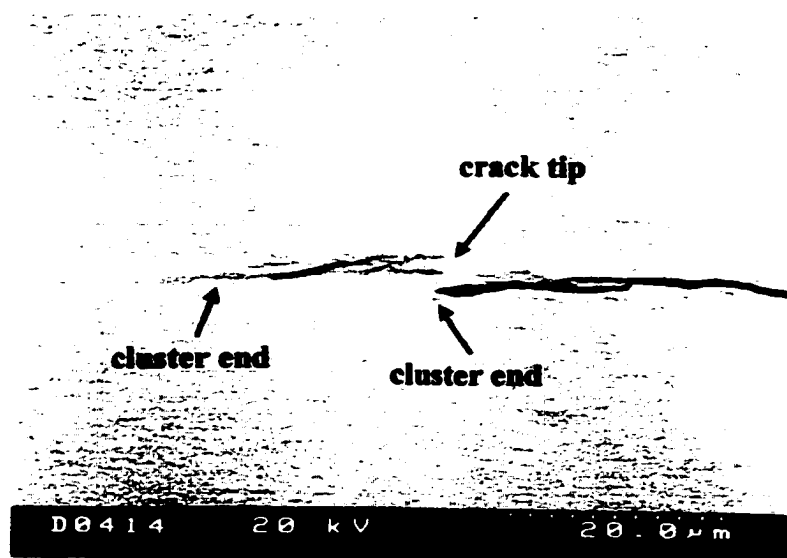
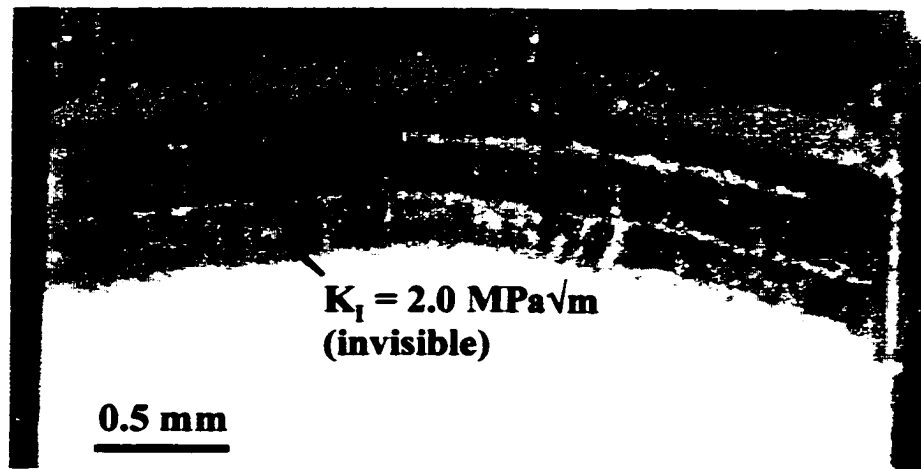
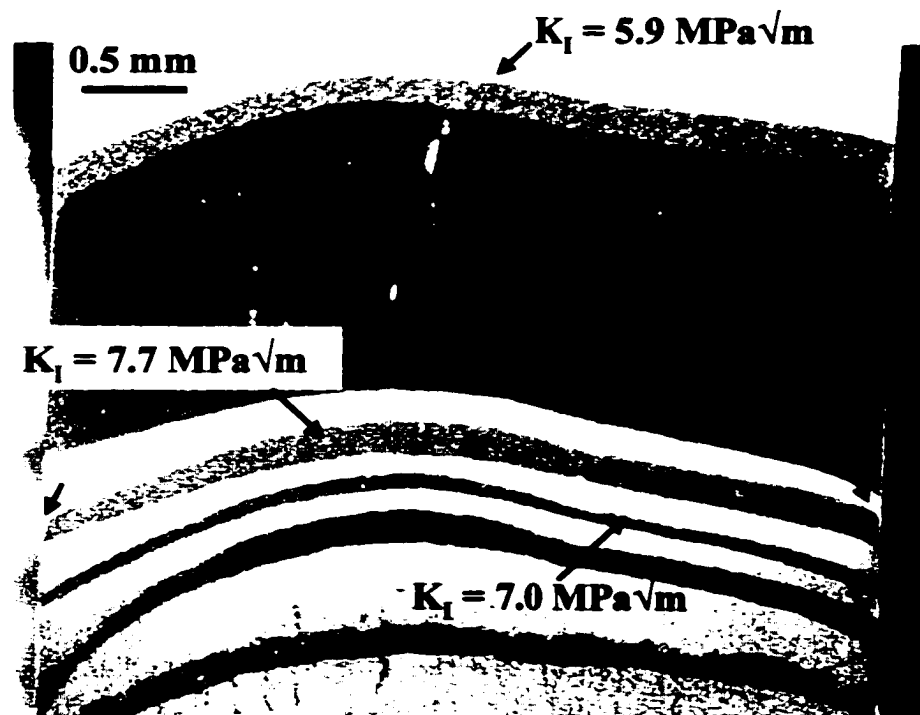


Figure 4.8. A partially fractured hydride cluster at crack tip, when $K_I = 7.0 \text{ MPa}\sqrt{\text{m}}$ (SEM).



(a)



(b)

Figure 4.9. Fracture surface showing variation of crack length along specimen thickness direction: (a) a specimen with many polishings and etchings; (b) a specimen with no polishing and etching.

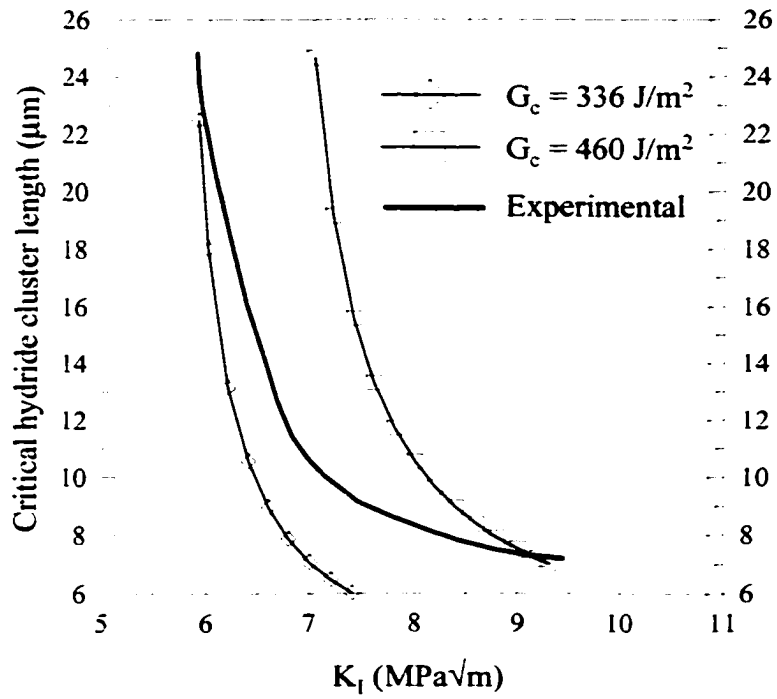


Figure 4.10. Comparison of critical hydride cluster length vs. applied K_I curves theoretically calculated and experimentally measured.

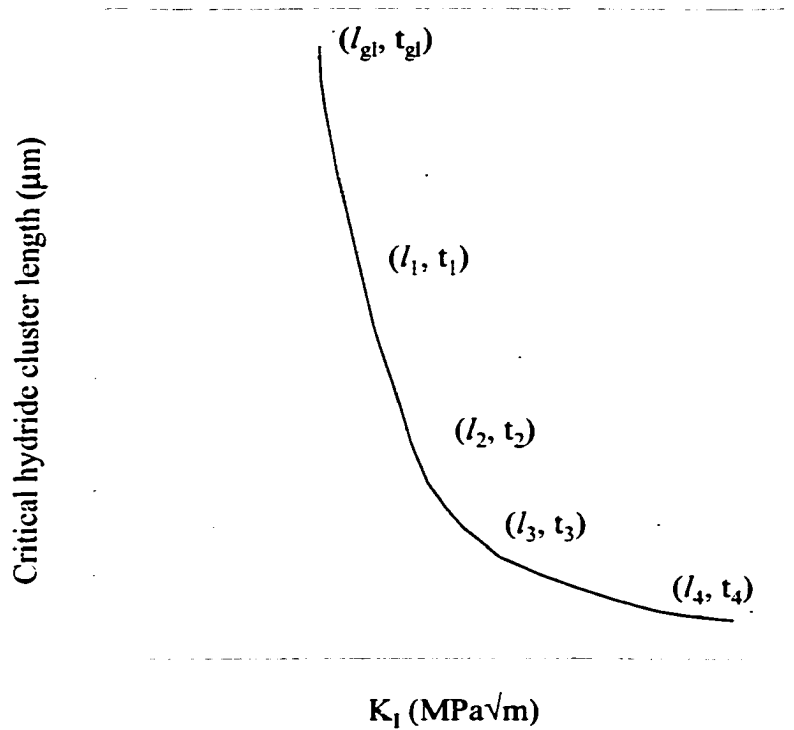


Figure 4.11. A schematic showing critical hydride cluster lengths and the lengths of hydride clusters that grow at different diffusion times, at different K_I 's. The solid line is adopted from figure 4.7 and gives the critical hydride cluster lengths at different K_I 's. The dotted lines are a series of lines that have the relation $L \propto K_I^2$, with the one on the top adopted from figure 4.7 giving the maximum length for hydride cluster growth.

CHAPTER 5. CONCLUSIONS

The initiation of delayed hydride cracking (DHC) in zirconium alloys has been studied in two aspects:

- (1) The effect of stress on the hydride precipitation solvus in zirconium has been studied from the view point of thermodynamics. The material equilibrium of a closed thermodynamic system which corresponds to a simplified model of hydride precipitation in zirconium is discussed using the internal energy minimization method. A general expression for the effect of external stress on the hydride precipitation solvus in zirconium is obtained for the simplified model.
- (2) The mechanism of the threshold stress intensity factor K_{IH} for DHC in Zr-2.5wt% Nb alloys is studied by using a modified experimental method. A new R-curve phenomenon for DHC initiation in Zr-2.5wt% Nb alloys has been observed and proposed for the first time. Based on this concept, K_{IH} is more carefully defined from the view point of experiment. The hydride cluster lengths at different applied K_I have been experimentally measured. Based on this work, the threshold phenomenon of DHC is explained. A qualitative micromechanical model which incorporates the effect of both stress and energy has been proposed to explain the details of the K_{IH} mechanism and some experimental phenomena.

CHAPTER 6. FUTURE WORK

The results presented in this work are preliminary, and may be improved or further developed through some possible future work:

(1) The model used in chapter 3 for studying the effect of stress on the hydride precipitation solvus in zirconium may be refined in two aspects. First, in deriving the material equilibrium conditions by applying the internal energy minimization method, the movement of the interfaces between different solid phases needs to be taken into consideration. Thus there

should be surface integrals involved in equation (3.2). This will make the model more rational for describing the hydride precipitation or growth, but will certainly add some complexity in the derivation. But it may not change the material equilibrium criterion, *i.e.* equation (3.26), that is used for deriving the effect of stress on the hydrogen precipitation solvus. Secondly, the interface energy and especially the plastic deformation energy may need to be taken into consideration in section 3.3.

(2) It would be interesting to apply the results from chapter 3 to the computer simulation of hydride precipitation and growth at the crack tip, and see how significant the effect of stress is.

(3) The results and discussion in chapter 4 are mostly qualitative and may be further developed. For example, the description of the Zr-2.5wt% Nb alloys' resistance to DHC, the R-curve, and the micromechanical model for describing the K_{IH} mechanism are still qualitative. When using the critical hydride cluster length at different applied K_I to explain the stages I and II behavior of DHC velocity, if a quantitative relationship can be found to describe the length of the hydride cluster that can grow at different times, one may be able to theoretically calculate the DHC velocity vs. K_I curve.

(4) There are unexplained experimental phenomena in the work of chapter 4, *e.g.* it is still not clear why no hydride cluster is observed at crack tip when the applied K_I is around $4 \text{ MPa}\sqrt{\text{m}}$ or lower.

REFERENCES

1. B.A. Cheadle, *Ontario Hydro Research Review*, August 1993, No. 8, 4 (1993).
2. B. Lustman and F. Kerze, Jr., *The Metallurgy of Zirconium*, McGraw-Hill Book Company, Inc. (1955).
3. Z. Li, *Handbook of Elemental Characteristic Data (in Chinese)*, Hebei People's Press (1985).
4. D.L. Douglass, *The Metallurgy of Zirconium, Supplement 1971*, Int. Atomic Energy Agency, Vienna (1971).
5. J.P. Langeron and P. Lehr, *Rev. Metall.* **56**, 307 (1959).
6. P. Gaunt and J.W. Christian, *Acta Metall.* **7**, 534 (1959).
7. W.G. Burgers, *Physica* **1**, 561 (1934).
8. L.T. Lloyd, ANL-6591 (1963).
9. B.D. Lichter, *Trans. AIME* **218**, 1015 (1960).
10. L. Espagno, P. Azou and P. Bastien, *Rev. Metall.* **57**, 254 (1960).
11. R.L. Beck, *Trans. ASM* **55**, 542 (1962).
12. H. Richter, P. Wincierz, K. Anderko and U. Zwicker, *J. Less-common Metals* **4**, 252 (1962).
13. C.E. Lundin and R.H. Cox, *Proc. USAEC Symp. on Zirconium Alloy Development*, GEAP-4089, I, 9-0 (1962).
14. B.A. Hatt and J.A. Roberts, *Acta Metall.* **8**, 575 (1960).
15. J. Winton and R.A. Murgatroyd, *Electrochem. Techno.* **4**, 358 (1966).
16. E.T. Hayes, E.D. Dilling and A.H. Roberson, *Trans. ASM* **42**, 619 (1950).
17. B.A. Cheadle, in *The Physical Metallurgy of Zirconium Alloys*, ed. B.A. Cheadle, CRNL-1208, CRNL, Chalk River, Ontario, Canada, 1 (1975).
18. D.L. Douglass, *Corrosion* **17**, 589 (1961).

19. M.R. Louthan, Jr. and R.P. Marshall, Paper presented at the 11th Annual AEC Corrosion Symp., Brookhaven, N.Y. (1962).
20. R.P. Marshall and M.R. Louthan, Jr., Proc. USAEC Symp. on Zirconium Alloy Development, GEAP-4089, 14-0 (1962).
21. A.C. Wallace, G.K. Shek and O.E. Lepik, unpublished research draft, Ontario Hydro Research Division, Toronto, Ontario, Canada (1988).
22. M.J. Manjoine and W.L. Mudge, Jr., Proc. ASTM, **55** (1955).
23. B.A. Cheadle, in *The Physical Metallurgy of Zirconium Alloys*, ed. B.A. Cheadle, CRNL-1208, CRNL, Chalk River, Ontario, Canada, 21 (1975).
24. J.J. Kearns, J. Nucl. Mater. **22**, 292 (1967).
25. G.G. Libowitz, J. Nucl. Mater. **5**, 228 (1962).
26. G.F. Slattery, J. of the Inst. of Metals **95**, 43 (1967).
27. C.E. Ells, in *The Physical Metallurgy of Zirconium Alloys*, ed. B.A. Cheadle, CRNL-1208, CRNL, Chalk River, Ontario, Canada, 67 (1975).
28. A. Sawatzky, J. Nucl. Mater. **2**, 62 (1960).
29. V.L. Gelezunas, Ph.D. Thesis, Univ. of Cincinnati, Cincinnati, Ohio (1962).
30. J.M. Markowitz, Trans. AIME **221**, 819 (1961).
31. J.C.M. Li, R.A. Oriani and L.S. Darken, *Zeitschrift für Physikalische Chemie Neue Folge*, Bd. **49**, 271 (1966).
32. R.L. Eadie, D. Mok, D. Scarth and M. Leger, *Scripta Metall. et Mat.* **25**, 497 (1991).
33. M.F. Kanninen and C.H. Popelar, *Advanced Fracture Mechanics*, Oxford University Press, New York (1985).
34. J.W. Hutchinson, *J. Mech. Phys. Solids* **16**, 13 (1968).
35. J.R. Rice and G.F. Rosengren, *J. Mech. Phys. Solids* **16**, 1 (1968).
36. J.W. Hutchinson, *J. Mech. Phys. Solids* **16**, 337 (1968).
37. J.D. Eshelby, Proc. R. Soc. London A **241**, 376 (1957).
38. C.F. Shih, Brown University Report No. MRL E-147, Providence, RI (1983).

39. E.T.C. Ho, unpublished research, Ontario Hydro Research Division (1988).
40. R. Dutton and M.P. Puls, in *Effects of Hydrogen on the Behaviour of Materials*, eds. A.W. Thompson and I.M. Bernstein, Metallurgical Society of AIME, New York, 516 (1976).
41. J.R. Rice and M.A. Johnson, in *Inelastic Behaviour of Solids*, eds. M.F. Kanninen, W.G. Adler, A.R. Rosenfield and R.I. Jaffee, McGraw-Hill Book Co., New York, NY, 651 (1970).
42. T.L. Anderson, *Fracture Mechanics (Fundamentals and Applications)*, CRC Press, Inc. (1991).
43. L.A. Simpson and M.P. Puls, *Metall. Trans.* **10A**, 1093 (1979).
44. R.L. Eadie and F. Ellyin, *Scripta Metall. et Mat.* **23**, 585 (1989).
45. J.R. Rice, *Proc. of the First Int. Con. on Frac., Sendai, Japan, 1965*, **1**, Part A-17, Japanese Soc. for the Strength and Frac. of Mat., 283 (1966).
46. J.R. Rice, *Fatigue Crack Propagation*, ASTM STP 415, 247 (1967).
47. H.M. Westergaard, *J. Appl. Mech.* **6**, A49 (1939).
48. X.Q. Yuan and K. Tangri, *J. Nucl. Mater.* **105**, 310 (1982).
49. G.C. Weatherly, *Acta Metall.* **29**, 501 (1981).
50. F. Ellyin and J. Wu, *Acta Metall.* **42**, 2709 (1994).
51. D.R. Metzger and R.G. Sauvé, COG Report No. 95 - ???, Ontario Hydro Technologies (1995).
52. S.R. MacEwen, C.E. Coleman, C.E. Ells and J. Faber, Jr., *Acta Metall.* **33**, 753 (1985).
53. R.L. Eadie, T. Tashiro, D. Harrington and M. Leger, *Scripta Metall. et Mat.* **26**, 231 (1992).
54. M.P. Puls, *Metall. Trans. A* **21A**, 2905 (1990).
55. S. Shi and M.P. Puls, *J. Nucl. Mater.* **208**, 232 (1994).
56. X.J. Zheng, L. Luo, D.R. Metzger, and R.G. Sauve, *J. Nucl. Mater.* **218**, 174 (1995).

-
57. E. Smith, *J. Mat. Sci.* **30**, 5910 (1995).
 58. H. Tada, P.C. Paris and G.R. Irwin, *The Stress Analysis of Cracks Handbook*, Del Research Co., Heller-town, Pennsylvania (1985).
 59. Cottrell, *Proc. of the First Tewksbury Symp., Univ. of Melbourne, Australia*, ed. C.J. Osborn, 1 (1963).
 60. L. Luo, *Ontario Hydro Research Division Technical Report No. 93-11-P* (1993).
 61. L.A. Simpson and C.D. Cann, *J. Nucl. Mater.* **126**, 70 (1984).
 62. A. Sawatzky, G.A. Ledoux, R.L. Tough and C.D. Cann, *Proc. Miami Int. Symp. on Metal-Hydrogen Syst., Miami Beach, 1981*, ed. T.N. Veziroglu, Pergamon Press, Oxford, U.K. (1982).
 63. C. Coleman, S. Sagat and K.F. Amouzouvi, *AECL report, Vol. Dec., 1* (1987).
 64. B.C. Skinner and R. Dutton, in *Hydrogen Effects on Material Behaviour*, eds. N.R. Moody and A.W. Thompson, *The Minerals, Metals&Materials Society* (1990).
 65. B.A. Cheadle, C.E. Coleman and M. Ipohorski, *ASTM STP 824*, 210 (1984).
 66. J.F.R. Ambler, in *Zirconium in the Nuclear Industry*, AECL, 653 (1984).
 67. J.F.R. Ambler and C.E. Coleman, in *Hydrogen in Metals*, Pergamon Press, Oxford, U.K., Paper 3C10 (1978).
 68. M.P. Puls, *AECL Report 6302*, AECL, Pinawa, Manitoba, Canada (1979).
 69. L.A. Simpson and M.P. Puls, *Metall. Tran. A* **10A**, 1093 (1979).
 70. R.R. Smith and R.L. Eadie, *Scripta Metall. et Mat.* **22**, 833 (1988).
 71. R.L. Eadie, D.R. Metzger and M. Leger, *Scripta Metall. et Mat.* **29**, 335 (1993).
 72. D.R. Metzger, *H3DTAP VERSION I - A THREE DIMENSIONAL FINITE ELEMENT PROGRAM FOR THERMAL AND ATOMIC DIFFUSION ANALYSIS*, Ontario Hydro Research Division Report 91-102-K, Toronto (1991).
 73. D.R. Metzger, *OHR Technical Report* (1995).
 74. D.J. Cameron and R.G. Duncan, *J. Nucl. Mater.* **68**, 340 (1977).

75. A.C. Wallace, G.K. Shek and O.E. Lepik, unpublished research draft, Ontario Hydro Research Division, Toronto, Ontario, Canada (1988).
76. G.K. Shek, M.T. Jovanović, H. Seahra, Y. Ma, D. Li and R.L. Eadie, *J. Nucl. Mater.* **231**, 221 (1996).
77. M.P. Puls, *Acta Metall.* **29**, 1961 (1981).
78. M.P. Puls, *Acta Metall.* **32**, 1259 (1984).
79. J.W. Gibbs, *The Scientific Papers of J. Willard Gibbs, Vol. 1*, Dover Publications Inc., New York (1961).
80. F. Larché and J.W. Cahn, *Acta Metall.* **21**, 1051 (1973).
81. F. Larché and J.W. Cahn, *Acta Metall.* **26**, 1579 (1978).
82. F. Larché and J.W. Cahn, *Acta Metall.* **26**, 53 (1978).
83. E. Smith, *Int. J. Pres. Ves. & Piping* **68**, 53 (1996).
84. R. Dutton, K. Nuttall, M.P. Puls, L.A. Simpson, *Metall. Trans. A* **8A**, 1553 (1977).
85. J.W. Cahn, *Acta Metall.* **10**, 907 (1962).
86. I.N. Levine, *Physical Chemistry*, McGraw-Hill Book Company, New York (1988).
87. E.A. Guggenheim, *Thermodynamics*, North-Holland Publishing Company, Amsterdam (1957).
88. J.D. Eshelby, in *Solid State Physics*, eds. F. Seitz and D. Turnbull, Academic Press, NY, vol. **3**, 79 (1956).
89. G. Lin, S. Skrzypek, D. Li, and R.L. Eadie, *J. Testing and Evaluation* **26**, 15 (1998).
90. M.P. Puls, *Metall. Trans. A* **19A**, 1507 (1988).
91. M.P. Puls, *Metall. Trans. A* **19A**, 2247 (1988).
92. E. Smith, *Int. J. Pres. Ves. & Piping* **61**, 1 (1995).
93. X.J. Zheng, D.R. Metzger, G. Glinka and R.N. Dubey, *ASME PVP*, vol. **326**, *Computer Technology: Application and Methodology*, 181 (1996).
94. L.A. Simpson, *Metall. Trans. A* **12A**, 2113 (1981).

-
95. G.K. Shek and D.B. Graham, in *Zirconium in the Nuclear Industry (The 8th International Symposium)*, ASTM STP 1023, L.F.P. Van Swam and C.M. Eucken, Eds., ASTM, Philadelphia, 89 (1989).
 96. G.P. Kiely, CRNL Report-2523 (1983).
 97. H.L. Ewalds and R.J.H. Wanhill, *Fracture Mechanics*, Edward Arnold Ltd., London, UK (1984).
 98. D.R. Metzger and R.G. Sauvé, ASME PVP, vol. **326**, *Computer Technology: Application and Methodology*, 137 (1996).
 99. D. Hardie and M.W. Shanahan, *J. Nucl. Mater.* **55**, 1 (1975).
 100. S. Shi and M.P. Puls, *J. Nucl. Mat.* **218**, 30 (1994).
 101. R.W. Hertzberg, *Deformation and Fracture Mechanics of Engineering Materials*, Fourth Ed., John Wiley & Sons, Inc. (1996).